

UNIVERSITY OF TRENTO  
DEPARTMENT OF PHYSICS



**Doctoral dissertation**

IN FULFILLMENT OF THE REQUIREMENTS  
FOR THE DEGREE OF DOCTOR OF PHILOSOPHY  
IN THE SUBJECT OF PHYSICS

---

**On-Line Sensing  
of the Interlacing Process**

---

*Candidate:*  
MADDALENA BERTOLLA

*Supervisor:*  
Prof. MARIO SCOTONI  
*Co-Supervisor:*  
Dott. MAURO CALDARA

ACADEMIC YEAR 2018/2019

**Maddalena Bertolla**

*On-Line Sensing of the Interlacing Process*

24 May 2019

Supervisor: prof. Mario Scotoni

Co-Supervisor: dott. Mauro Caldara

Reviewers: prof. Arianna Mencattini and prof. Diego Scaccabarozzi

**University of Trento**

Department of Physics

Via Sommarive 14

38123, Trento, Italy

**Aquafil Spa**

Via Linfano 9

38062, Arco, Trento, Italy



---

**Abstract:** This thesis deals with the study of the yarn interlacing. The interlacing process is commonly employed by textile industries to impart cohesion points to a multi-filament yarn. Indeed, this work has been realized in the framework of a collaboration between the Department of Physics of the University of Trento (Italy) and Aquafil S.p.A., a company producing Nylon 6 yarn.

The interlacing of the filaments into periodic knots is caused by their interaction with a turbulent flow, but the full dynamics is not well characterized. Additionally, one problem that textile industries need to face is the irregularity of the process, still difficult to improve. A regular knots distance is required to ensure the homogeneous appearance of the final fabric.

Hence, it is interesting to understand which are the key parameters affecting and influencing interlacing, to improve its regularity. For this reason, the present work focuses on a deeper understanding of the process dynamics. Then, different on-line sensing techniques that measure the knots distance are investigated and compared. The evaluation of the process regularity during yarn production allows, as a further step, to change the machine parameters on-line, avoiding waste of time and material.

In **Chapter 1** is given the background knowledge about the yarn production process, starting from the raw material. The attention will be focused on interlacing, with an overview of the state of the art literature on that topic.

In **Chapter 2** the yarn-air interaction is investigated, with a high speed analysis of the yarn motion in an interlacer. A dynamics of interlacing is proposed, indicating the key role played by the turbulent pattern, observed by means of a tracer.

**Chapter 3** studies the vibrations close to the interlacer, to monitor a possible flow modulation caused by the yarn-air interaction.

In **Chapter 4** and **Chapter 5** two sensing techniques have been approached, based on the use of a microphone and a photodiode. The issues related to those measurements have been investigated, for a final comparison of their performance in terms of capability of detecting the cohesion points distance on-line, on a running yarn.

---



# Contents

<b>1</b>	<b>Background</b>	<b>1</b>
1.1	Aquafil and its production cycle . . . . .	2
1.1.1	Nylon 6 polymerization and production . . . . .	2
	Polymerization . . . . .	2
	Industrial production of Nylon 6 chips . . . . .	3
1.1.2	Fibers production . . . . .	6
	Melt spinning . . . . .	7
	Fibers drawing . . . . .	8
	Texturing and interlacing . . . . .	10
1.1.3	Properties of fibers . . . . .	11
	Linear density . . . . .	11
	Tensile properties . . . . .	12
	Crimp evaluation . . . . .	12
	Entanglement testing . . . . .	12
1.2	The interlacing process . . . . .	13
1.2.1	Aim of the work . . . . .	13
1.2.2	State of the art of interlacing . . . . .	14
	Interlacing dynamics . . . . .	15
	Variables influencing the process . . . . .	18
	On-line yarn evaluation . . . . .	22
<b>2</b>	<b>High speed imaging</b>	<b>23</b>
2.1	Materials and methods . . . . .	24
2.1.1	Experimental setup . . . . .	24
2.1.2	Image processing . . . . .	25
2.2	Experimental measurements . . . . .	26
2.3	Flow visualization . . . . .	30
2.4	Chapter summary . . . . .	33
<b>3</b>	<b>Vibration analysis</b>	<b>35</b>
3.1	Motivation of the vibration measurement . . . . .	36

3.1.1	Air flow-yarn interaction . . . . .	36
3.1.2	Shock waves-yarn interaction . . . . .	38
3.2	Design of the experimental setup . . . . .	40
3.2.1	Lower limit of detection . . . . .	41
3.2.2	Resonance frequencies of a screwed plate . . . . .	41
	Simplified model: the cantilever beam . . . . .	42
	Improved model: the screwed plate . . . . .	46
	Experimental results . . . . .	48
3.2.3	Mechanical filters . . . . .	49
	Accelerometer saturation . . . . .	49
	Free vibration of a viscously damped system . . . . .	50
	Response of a damped system to a harmonic excitation . . . . .	54
	Experimental results . . . . .	55
3.3	Vibrations induced by the interlacing yarn . . . . .	57
3.4	Chapter conclusions . . . . .	61
<b>4</b>	<b>Acoustic analysis of an interlaced yarn</b>	<b>63</b>
4.1	Feasibility study . . . . .	64
4.1.1	Yarn diameter modulation during production . . . . .	64
4.1.2	Simulation of air pressure close to the yarn . . . . .	65
4.2	Theoretical background . . . . .	68
4.2.1	Wave equation, speed of sound and sound pressure level . . . . .	68
4.2.2	The acoustic impedance . . . . .	70
4.2.3	Acoustic filters . . . . .	71
4.3	Experimental measurements . . . . .	74
4.3.1	Experimental setup . . . . .	74
4.3.2	Acoustic filter design . . . . .	74
4.3.3	Sensing of the interlaced yarn . . . . .	77
4.3.4	Improvement of yarn signal over external noise . . . . .	82
4.4	Chapter conclusions . . . . .	87
<b>5</b>	<b>Optical sensing of an interlaced yarn</b>	<b>89</b>
5.1	Theoretical background . . . . .	90
5.1.1	Basic operating principles of a photodiode . . . . .	90
5.1.2	Load resistance and transimpedance amplifier . . . . .	92
5.1.3	Position sensitive detectors . . . . .	93
5.2	Materials and methods . . . . .	95
5.2.1	Description of the experimental setup . . . . .	95
5.2.2	Sensor calibration . . . . .	97
5.3	Experimental measurements . . . . .	100

5.3.1	Detection of yarn modulation . . . . .	100
5.3.2	Sources of noise . . . . .	102
5.3.3	Evaluation of the mean distance between knots . . . . .	104
5.3.4	Reconstruction of the yarn profile from the time signal .	107
5.4	Signal processing to detect irregular patterns . . . . .	110
5.4.1	Threshold proportional to the signal amplitude . . . . .	111
5.4.2	Cross-correlation analysis . . . . .	113
	Correlation with a regular signal segment . . . . .	113
	Correlation with a Gaussian wave packet . . . . .	115
	Sources of cross correlation amplitude modulation . . . .	120
5.5	Comparison of the acoustic and optical approach . . . . .	123
5.5.1	Simultaneous measurement of the mean interlacing fre- quency . . . . .	123
5.5.2	Signal to noise ratio evaluation and comparison . . . . .	124
5.5.3	Detection of missing or irregular knots . . . . .	126
<b>Conclusions</b>		<b>130</b>
<b>Bibliography</b>		<b>133</b>
<b>Publications</b>		<b>141</b>
<b>Conference presentations</b>		<b>142</b>
<b>Acknowledgments</b>		<b>144</b>



# 1

## Background

### Contents

---

<b>1.1</b>	<b>Aquafil and its production cycle . . . . .</b>	<b>2</b>
1.1.1	Nylon 6 polymerization and production . . . . .	2
1.1.2	Fibers production . . . . .	6
1.1.3	Properties of fibers . . . . .	11
<b>1.2</b>	<b>The interlacing process . . . . .</b>	<b>13</b>
1.2.1	Aim of the work . . . . .	13
1.2.2	State of the art of interlacing . . . . .	14

---

## 1.1 Aquafil and its production cycle

The research project results from the collaboration between the Department of Physics of the University of Trento and Aquafil S.p.A. (Arco, Trento).

Aquafil S.p.A. is a multinational company that produces and sells Nylon 6 yarn. In particular, it operates through two product areas: the yarn for carpets and the yarn for garments used in the apparel and sportswear industries. The company is deeply involved in lowering the environmental impact of its production. This commitment lead to the development of ECONYL®, that is a yarn produced using secondary raw materials made of recycled waste products such as end-of-life fishing nets and used carpet fluff [1].

A general overview of the production process of Aquafil S.p.A. will be given in the next pages, in a way that the reader can easily understand the main topic. In the next paragraphs will be explained the processes that, starting from the raw materials, lead to the final yarn.

### 1.1.1 Nylon 6 polymerization and production

#### Polymerization

Nylon is a generic way of calling high molecular weight polyamides, that are semi-crystalline polymers produced by the condensation of a carboxylic acid with an amine. The  $-\text{COOH}$  acid group reacts with the  $-\text{NH}_2$  amine group to form the amide, with the release of a molecule of water. There are several types of Nylon and each type is described by a number that refers to the number of carbon atoms present in the molecular structures of the amine and acid, respectively (or a single suffix if the amine and acid groups are part of the same molecule) [2]. This is the case of Nylon 6, that begins as pure caprolactam, a ring-structured molecule with six carbon atoms. It is actually the raw starting material bought by Aquafil S.p.A. for the yarn production. Caprolactam does not polymerize when it is dry, hydrolytic polymerization is normally used for fibers.

The hydrolytic polymerization of  $\epsilon$ -caprolactam can be described by three main steps.

- **Opening of the ring** (Fig.1.1 A)

This reaction is also called hydrolysis of the  $\epsilon$ -caprolactam and occurs mainly in the molten caprolactam (melting temperature of  $69^\circ\text{C}$ ). The carbonyl oxygen steals a hydrogen from the water molecule, creating an instability in the ring structure of caprolactam and resulting in a more stable linear molecule. It is an endothermic reaction ( $\Delta H = 2240 \text{ cal/mol}$ ) and hence it is enhanced by temperature. Moreover, it depends on the



amount of water, commonly about 5-10% of the monomer content. The linear molecule produced by this reaction is the  $\epsilon$ -amino-caproic acid [3].

- **Polyaddition** (Fig.1.1 B)

The linear  $\epsilon$ -amino-caproic acid can, in turn, react with a caprolactam molecule. This latter steals the acid hydrogen from the linear amino acid, causing itself the opening of the ring and the step by step addition of caprolactam units to the polymer chains. This reaction can occur both between caprolactam and a single amino-caproic acid molecule and with an oligomer. The reaction is exothermic ( $\Delta H = -4030$  cal/mol) and hence it is disadvantaged by high temperature values. In the working conditions, this reaction is both responsible for the rapid growing of the polymeric chain, but also for the amount of the residual unreacted monomers and oligomers (10-20%).

- **Polycondensation** (Fig.1.1 C)

Also this reaction is responsible for the growing of the polymeric chain and results from the condensation of amine and carboxyl terminal groups of two linear  $\epsilon$ -amino-caproic acids (or oligomers), leading to the formation of an amide group and a molecule of water. Those water molecules are in turn involved in the ring opening of caprolactam. In this way, product molecules are subtracted to the reaction and the equilibrium position is moved to the left, according to le Chatelier's principle. In other words, subtracting water we enhance the occurrence of the condensation reaction and hence we increase the molecular weight of the resulting polymers. Also this reaction is exothermic ( $\Delta H = -6270$  cal/mol) [3].

Steps B and C do not occur necessarily in the described order in the polymerization of Nylon 6.

### Industrial production of Nylon 6 chips

- **Production of base Nylon 6 chips**

**Polymerization** In industries polymerization of Nylon 6 can be carried out either in a semi-batch reactor or in a continuous tubular reactor. Nowadays, this latter is preferred since it reduces the production times. A semi-batch reactor is employed when the polymer composition need to be changed, due to a higher flexibility of this approach. Continuous processes use a reaction vessel called a VK tube (from the German expression Vereinfacht Kontinuierlich, simplified continuous). A common VK tube is a 8 – 10 m tall and narrow reaction vessel that consists of different zones where temperature can be independently measured and

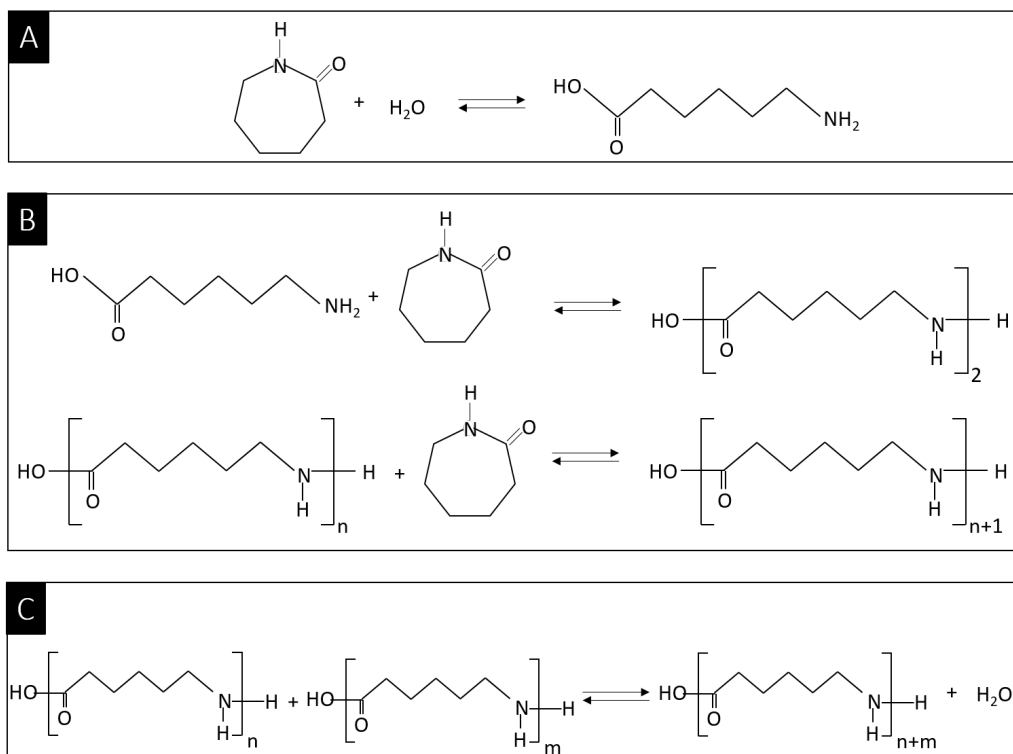


Figure 1.1: Steps in the hydrolytic polymerization of Nylon 6. Ring opening polymerization reaction (A), polyaddition (B), polycondensation (C).

controlled. The reaction mixture, that consists of the molten caprolactam, mixed with 0.5-5% wt. of water, is fed under nitrogen cover at the top of the reactor, where also other additives can be included. Nitrogen is necessary to avoid possible oxidation reactions.

The reaction mixture enters the tube with a temperature of about 90 °C and it is heated to 230 °C as it passes through a heat exchanger, causing the ring opening reaction. Then, the melt is further heated by the ongoing addition and condensation exothermic reactions, reaching 270 – 280 °C. At this stage, most of the added water is evaporated and removed as condensate. As we move down the reactor, temperature increases, more water is evaporated and the vapor rises to the top surface of the reactor. The heat transfer is enhanced, as well as the equilibrium in the upper portion of the reactor. In the lower part of the reactor, temperature is decreased to 250 °C by another heat exchanger. In this condition, we are favoring the equilibrium of polyaddition and condensation reactions, lowering the amount of non reacted monomer and increasing the mean molecular weight. Additionally, the decrease in temperature prevents also

from the formation of water vapor bubbles, that could cause ruptures in the final polymer. The polymer resulting from this process consists of about 200 units (mers) and is characterized by a molecular weight of 15-20 kDa.

The whole polymerization process takes about 18 – 20 hours. In order to reduce this time, double stage reactors have been realized, separating the ring opening reaction from the other two steps. Indeed, since the ring opening is enhanced by pressure and temperature, in the first stage pressure is increased to about 3 bar. The second stage operates under pressure, to favour water elimination. This results in a speed up of the reaction (12 – 13 hours globally) [4].

#### **Extraction with water and drying**

In both cases, unreacted caprolactam and oligomers are still present in the final polymer (about 10%), that need to be removed to enhance the mechanical properties of the final fiber [5]. The polymer emerging from the VK tube is extruded into strands and cut into chips. The unreacted monomers and oligomers in the chips are extracted by a counter current hot water flux (105 – 110 °C) that is progressively concentrated reaching the top of the vertical extraction column. The resulting water is then distilled and reused and the unreacted caprolactam and oligomers are recovered. After extraction with water, the Nylon 6 chips are dried under nitrogen and are stocked, until they are remelted during extrusion into fibers [6]. The chips are stored in silos under nitrogen atmosphere, to prevent thermo-oxidation and moisture absorption.

- **Production of Nylon 6 color masterbatches**

**Monoconcentrated masterbatches** are materials obtained adding to the Nylon powder a high amount of color pigments (5-50% wt.). Pigments are usually mixed with the polymer matrix by means of a double screw extrusion process. An extruder consists of a screw that rotates into a barrel containing the polymer, that is fed from a hopper to the screw. At the end of the extruder, the melt passes through a die to produce an extrudate of the desired shape [7]. The polymer is melted both by friction forces and by heaters placed along the barrel. High shear stresses given by the screw guarantee penetration, dispersion and distribution of the pigment in the polymeric matrix [8].

**Color masterbatches** are chips of the final color, obtained extruding different monoconcentrated masterbatches to produce the color requested. For coloring plastic materials, the masterbatch concentrates are added to the polymer through another extrusion process. This approach guarantees better results in terms of safety (avoiding dust on working

place) and product quality (better dispersion) with respect to the direct use of pigment powders [9].

### 1.1.2 Fibers production

Spinning is the first step in the conversion of the bulk polymer to fiber form, followed by drawing, texturing and interlacing. In Aquafil S.p.A. the fibers production process is continuous, also called bulk continuous filament. This means that the different steps occur continuously; here, they will be described separately, for clarity reasons.

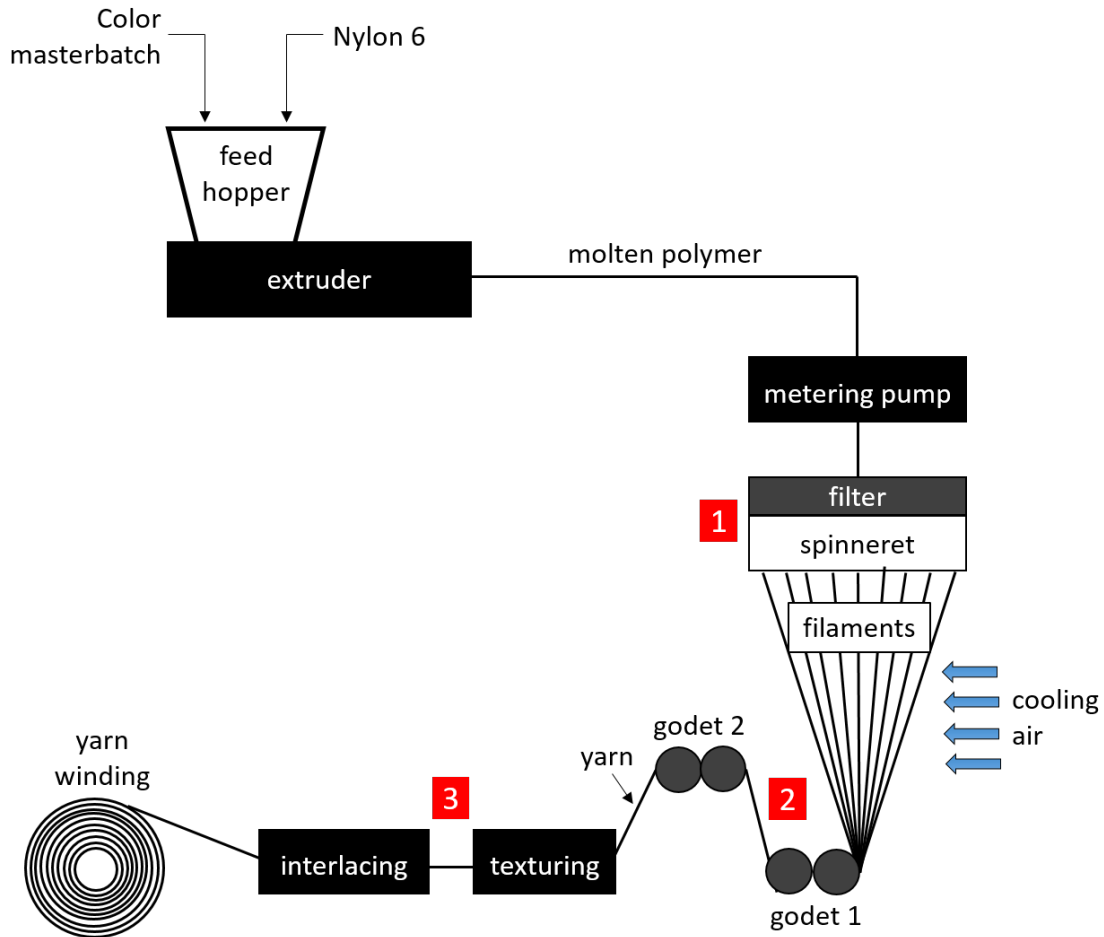


Figure 1.2: Schematic diagram of fibers production process, with an insight into the melt spinning process (1), the fibers drawing (2) and the texturing and interlacing processes (3).

### Melt spinning

In Fig.1.2 (1) are illustrated the main steps of the melt spinning process.

- Initially, polymer chips and color masterbatch are fed into the hopper of an extruder.
- At this point, the molten polymer is fed to a metering pump, that maintains an exact volume of molten polymer per unit time to the spinneret. This expedient guarantees a control of the linear density of the final product. The molten polymer is filtered, to remove impurities or aggregates that may cause spinneret clogging.
- Then, it passes through the spinneret, that is a plate with a number of small holes ( $100\text{-}400\text{ }\mu\text{m}$  diameter), equal to the number of filaments required in the final yarn [6]. The shape of the spinneret holes determines the shape of the cross section of the resulting fibers, considering of course the effects of polymer surface tension and viscosity, that attempt to return always the fiber to a circular shape. Different cross sections, such as trilobal, allow to achieve special properties like luster, opacity, air permeability or insulation [10]. For example, a fiber like cotton with rough surface and irregular shape, has lower luster. On the other hand, smooth, regular round fibers reflect light better, but tend to show soiling more easily than a multilobal cross section [11].  
The final density of the filaments is not determined by the diameter of the holes but by the rate at which the polymer is pumped through the spinneret and the rate at which the filaments are wound up (process described in the following section).
- The filaments emerging from the spinneret enter an air stream and begin to cool.
- As they have traveled enough to become solid, they are brought together and wound up at speeds typically above  $1000\text{ m/min}$ . This bunch of fibers brought together is also called multi-filament yarn, that is a grouping of fibers to form a continuous strand. After spinning, the filaments are almost completely unoriented, since most of the stretching that occurs between the spinneret and the windup happens while the filament is still molten. Hence, molecules have enough time to relax before the fiber cools and solidifies. This is the reason why a separate drawing step is necessary before yarn collection into bobbins [12].

**Fibers drawing**

- **The drawing process** Up to now, we have seen that spinning processes the yarn in a fibrous form, but these fibers lack good tensile properties. Indeed, the elongation at break is very high and initial modulus is low. This gives poor stability to the fiber, that can elongate up to six times [6]. The drawing step is necessary to improve the fibers properties, enhancing the polymer orientation before solidification. It is realized by means of two sets of heated rolls, called godets. The first pair of godets works at low temperatures and speed (commonly 50 °C and 1000 m/min), while the second works at higher temperatures and speeds (e.g. 190 °C and 3500 m/min) (see Fig.1.2 (2) for a representation of the two godets). The draw ratio is defined as the ratio between the speed of the second and the first godet. The higher the draw ratio, the lower the linear density. In textile applications common values of draw ratio range from 2 to 5. The yarn tension is monitored on-line during this process, by means of a load cell based tensiometer (commonly around 70 cN).
- **Crystallization induced by drawing** Different studies indicate that increasing the draw ratio allows both to decrease the elongation and improve the tenacity of the final yarn [13]. The main reason behind the improvement of the yarn properties with the draw ratio is the orientation of Nylon 6 fibers induced by drawing. In Fig.1.3 is illustrated the relative orientation of fibers. After spinning, fibers do not show orientation due to relaxation phenomena, then filaments diameter decreases due to the flow with a partial drawing and orientation due to gravity. Finally, molecular chains are more and more oriented by the drawing process. To understand the morphology of Nylon 6 in those different phases, we need to look deeper into the structure of Nylon 6. The structure of Nylon 6 is quite polar, which induces the formation of hydrogen bonding between the polymer chains (-CO—HN- bond). This causes the folding of the polymeric chains in organized structures, called lamellae, that are further linked together to form aggregates, called spherulites. The areas surrounding the spherulites are amorphous, meaning that the polymer forms a disordered structure. The semicrystalline structure just described results from crystallization in a quiescent homogeneous melt in the absence of external forces. In the production process, during spinning and drawing, the solution is subjected to an external stress that leads to the breakdown of lamellae and spherulites with the formation of new crystalline structures, called fibrils [12].

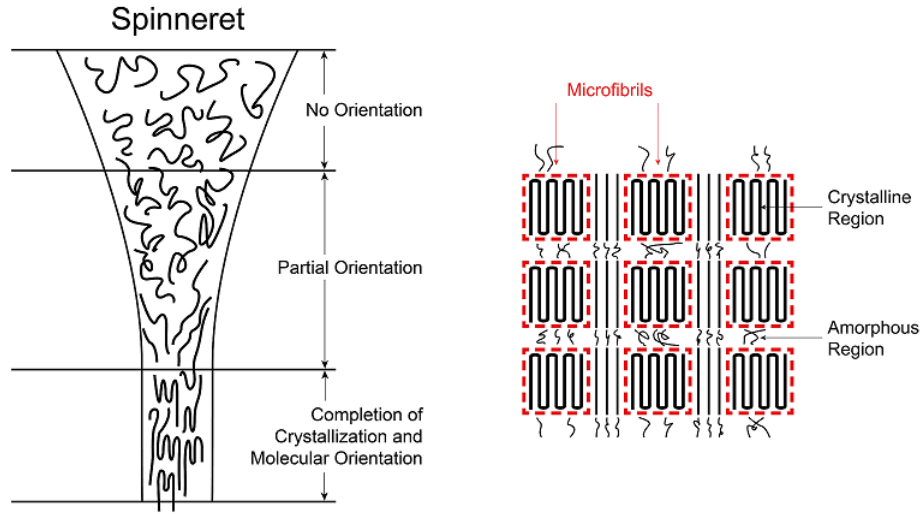


Figure 1.3: Fibers orientation after spinning and due to drawing with an insight into the fibrils structure induced by orientation.

At this point, fibers are more and more oriented (like in the final part of Fig.1.3) and Nylon 6 can crystallize in two different forms, monoclinic  $\gamma$  and monoclinic  $\alpha$ , according to the arrangement of the macromolecules [14]. In the  $\gamma$  phase, the hydrogen bonds bridge parallel macromolecular chains and they are not collinear, as represented in Fig.1.4. This bond requires a rotation of the amide groups which results in a shrinkage of the unit cell parameter. On the other hand, when the molecules are arranged in opposite directions (antiparallel chains), they form a zig-zag planar structure, called  $\alpha$  phase, characterized by collinear H-bonds [15]. Since no bond rotation is involved in this structure, the  $\alpha$  phase is the most stable structure [5]. The resulting sheets are stacked upon each other by Van der Waals interactions. The bonds cause close packing between chains, resulting in high crystallinity. This crystallinity leads to high strength, high stiffness, good toughness, good abrasion resistance, low gas and vapor permeability. In general, mechanical and physical properties are affected by the amount of crystallization. The high crystallinity of Nylon 6 causes also a high melting temperature (220-230 °C), enabling the employment of this material also in high temperature conditions. The main limitation is the Nylon sensitivity to water, that may cause hydrolytic degradation of the material.

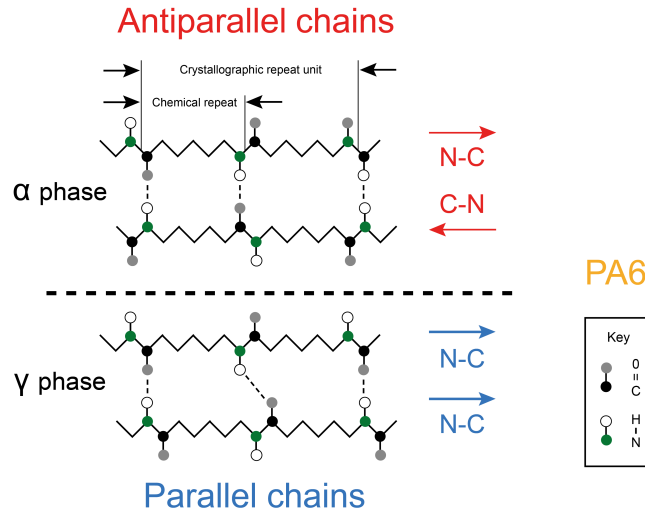


Figure 1.4: Molecular arrangements in the  $\alpha$  and  $\gamma$  crystal lattices of Nylon 6.

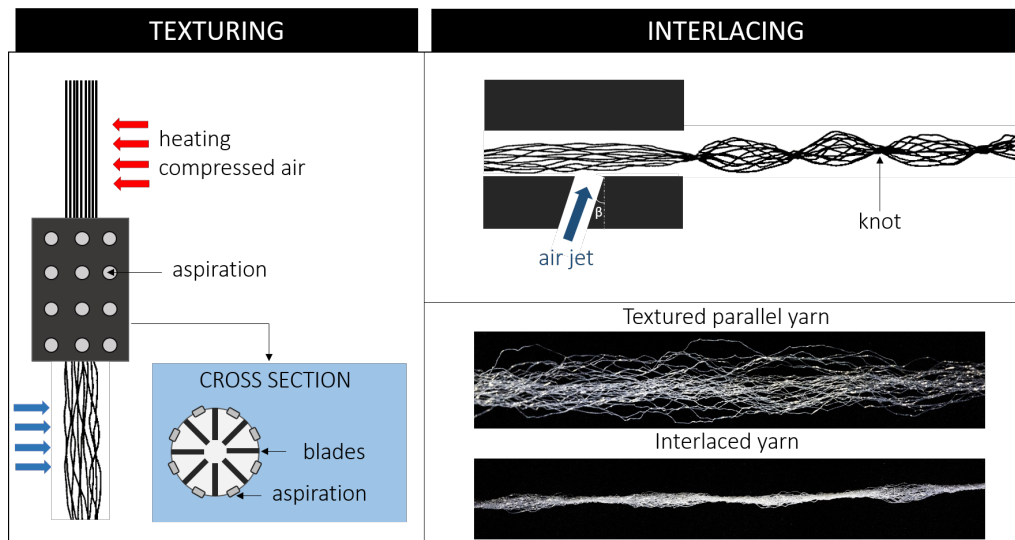


Figure 1.5: Schematic representation of texturing and interlacing and picture of the resulting processed yarns.

### Texturing and interlacing

The yarn needs to undergo two other processes before collection into reels, that are texturing and interlacing.

**Texturing** is the conversion of flat to crimped fibers, where crimp refers to the waviness of a fiber along its length. The yarn produced by this process resembles better natural yarns (such as wool), both in appearance and physical characteristics. The distortion of fibers improves their apparent volume,



stretching properties as well as the perceived feel (e.g. softness) and covering feature of the resulting fabric. Cover is an important property of a fabric, especially in the carpet sector, and it is enhanced by the use of multifilament textured yarns (with respect to single filament) in waving. Additionally, this process improves the insulation properties of fibers, since they will better trap air [16].

The method employed by the company is called jet-texturing. The yarn is hit by a hot compressed air jet, that increases initially the yarn volume. Then it enters the texturing unit, that consists of a chamber with internal blades and nozzles for air aspiration (Fig.1.5). In this way, both deformation and shape fixing are guaranteed.

Since a yarn is composed of many filaments, it is difficult to further process it into the final carpet or fabric by weaving or tufting. Indeed, filament cohesiveness is required and is reached by means of **interlacing**. An interlacer consists of an air jet nozzle and a yarn channel. Commonly, the air jet nozzle is not perpendicular to the yarn channel, but tilted of an angle  $\beta$  with respect to the normal (Fig.1.5). As the compressed air jet interacts with the running yarn, filaments are intermingled with each other, creating periodic nodes, also called knots, with almost uniform spacing. The loose filaments are hence transformed into an entangled yarn suitable for further processing [10].

Both texturing and interlacing are performed on a continuously running yarn, after spinning and drawing, as shown in the scheme of Fig.1.2.

### 1.1.3 Properties of fibers

Testing of the fibers resulting from the processes described above is important from the point of view of quality control. For this reason, in this section will be presented some of the main properties of the final yarn and the way they are tested. The following tests are periodically performed by the company as quality control, testing some meters of yarn for each production lot.

#### Linear density

The mass for unit length of a fiber is the common way to measure its fineness. It has been adopted due to the difficulties associated with the diameter measurement, since the cross section is non circular and variable. It is simply determined measuring the mass of 10 m of a pretensioned yarn. As a result, the linear density is measured in dtex, where

$$1 \text{ dtex} = \frac{\text{weight [g]}}{10 \text{ km of yarn}} \quad (1.1)$$

The linear density depends on different parameters like the diameter or the number of filaments composing the yarn. One example of yarn produced in Aquafil S.p.A. is a 42 filaments yarn, with an average diameter of each fiber of  $70\text{ }\mu\text{m}$  and a linear density of 1000 dtex.

### **Tensile properties**

As already explained, typically a yarn is composed of many filaments, further processed to guarantee the cohesion necessary for the conversion of the yarn into fabric. Additionally, a multi-filament yarn can be further combined with another yarn, for example through an additional interlacing step or by means of a twisting process. The number and type of yarns that are combined to produce the final yarn depends on the required application, in terms of color or mechanical properties. The thread resulting from the combination of two yarns is called *double end yarn*, moving to *triple end yarn* and so on.

Increasing the number of filaments increases the strength of the final thread and its tensile properties are a combination of the individual filaments. When the filaments are straight and parallel, the combination would be additive. With twisting, texturing and interlacing, the reciprocal fibers and crystal orientation with respect to the applied force need to be considered.

The tensile properties of a material are measured using machines that transmit force to the yarn and record the corresponding elongation. To make possible the comparison of different yarns, the unit of force is commonly normalized by the linear density of the yarn. For example, for a yarn, the tenacity is defined by the ratio of the force at failure divided by the linear density of the fiber (measured in cN/dtex) [11].

### **Crimp evaluation**

Another property of the final yarn that needs to be tested is the crimp imparted through the texturing process. Indeed, the crimping extent determines the covering properties of the final fabric.

First, the yarn is boiled in water and then, applying different weights, the elongation is evaluated. If the elongation is lower than expected, the temperature of the heating jet is increased (Fig.1.5) in a way that texturing is enhanced.

### **Entanglement testing**

Interlacing results in sections of filaments entanglement, alternating with open sections. The distance between knots in terms of number of entanglements per unit length, as well as their strength and distribution determines the final appearance, homogeneity, softness and covering capability of the fabric. Missed

or weak entanglements cause fabric production problems, as well as streaks in knit and woven fabrics. After yarn production, the company monitors the knots distance on the yarn sample. Two methods are used by the quality control department of the company, both imparting a known tension to the interlaced yarn. A difference in this pre-tension value with respect to the winding tension, causes a variation in the distance between knots estimated by the quality control with respect to the distance that would be measured on-line during interlacing.

The first method is based on the use of an **optical micrometer**. A parallel light curtain is transmitted via a lens arrangement into the receiving unit, that is a linear CCD sensor. If the yarn is placed in the light path, its profile is reconstructed from the generated shadowing. The profile allows to evaluate both the tension and the distance between knots.

The other method is based on a **capacitive measurement**. One plate of the capacitor is fixed, while the other plate is a cantilever beam leaned against the yarn and it moves following the yarn profile. As the cantilever senses a knot, the capacitance decreases, since the distance between plates is increasing with the strength of the knots. As a matter of facts, the increase in thickness is proportional to the degree of interlacing. In this way, the size, the distance and the strength of knots is evaluated.

Also another capacitive based sensing device is employed by the company to monitor on-line the yarn diameter fluctuations. This technique is based on the use of an interdigital capacitor, powered with an electrical alternating voltage. The yarn interactions with the electrical field produce a capacity variation, that depends also on the distribution of the yarn filaments. In this way, assuming that dielectric polarization intensity is uniform along the yarn, the current measured is proportional to the yarn shape. However, this technique is sensitive to environmental factors since the dielectric constant is also dependent on the moisture content, that is not homogeneous along the yarn [17]. Additionally, residual electric charges on the yarn surface could affect the measurement. For this reason, the sensor is used just to evaluate the stability of the yarn diameter during production.

## 1.2 The interlacing process

### 1.2.1 Aim of the work

The previous section dealt with the quality control measurements that the company is performing to establish the regularity of interlacing on some meters of a sample yarn for a given lot. However, it occurs that bobbins from

the same lot show different interlacing strength levels, variations in the distance between knots, or sections where knots are missing. For this reason, the response of the quality control is not always representative of the knots distribution over the whole yarn production. On the other hand, to guarantee high efficiency and homogeneity of fabric processing, the entanglements need to be evenly distributed and of similar strength levels.

In light of this situation, it is necessary to monitor on-line the regularity of interlacing, during yarn production. The sensor required needs to be stable and cheap enough to be implemented on the hundreds of interlacers used in the industrial plant. This rules out the possibility of using an optical micrometer, due to its high cost. The high yarn speed and tension prevent also us from the use of the capacitive sensor, since the cantilever touching the yarn could cause its break or damage. A sensor without direct contact to the yarn is preferred to guarantee the desired stability.

Additionally, the causes of irregularity of interlacing are still unclear. It could be caused for example by a fluctuation of air pressure, yarn speed or tension. The key parameters influencing the regularity of the process can be individuated just with a deeper understanding of the dynamics of knots formation.

For this reason, in the following section will be given a brief overview of the literature about interlacing, to better understand the process.

### **1.2.2 State of the art of interlacing**

In the textile industry the need of cohesion points in a parallel yarn has always been an issue, since otherwise the yarn can incur problems in manufacture and handling. The first way employed to overcome this lack of cohesion was a twisting step followed, if necessary, by sizing. However, these processes are quite time consuming and constitute an additional step, increasing the cost of the yarn manufacturing operations. From this consideration arised the necessity of make the filaments to cohere by other methods [18].

The earliest patent about interlacing was taken out in 1961 by Du Pont, an american chemical company [19]. The theory of filaments intermingling has come behind its industrial practice and the studies performed have been focused more on the process development rather than its full understanding. The main efforts were made in the improvement of the interlacer geometry to reduce compressed air consumption. Few studies focused also on the identification of the key elements leading to a variation in the nips features, in terms of regularity, strength and knots distance and on the study of the interlacing dynamics.

The main advantage of interlacing with respect to the previous techniques is its easy integration into the continuous yarn production process, without ad-

ditional steps, and its simplicity of operation. However, interlacing produces cohesion with a degree of irregularity in nip spacing. Moreover, intermingling nozzles are not flexible in the intermingling capability, making difficult the production of nips at a frequency outside a very narrow range. So, proper geometries are necessary for different applications and it is also difficult to design a nozzle for a precise nips frequency. For this reason, also other techniques are under investigation. A novel method of creating cohesion at the desired frequency is based on the use of a pulsed laser that hits the yarn at discrete points. Even if the flexibility and validity of this technique have been proved, it is too expensive to be implemented at an industrial level, on hundreds of plants [20]. For this reason, interlacing is still the leading technology in imparting cohesion to a parallel yarn at industrial level.

### Interlacing dynamics

Filaments intermingling results from their interaction with the air jet. So, an insight into the airflow pattern in the yarn channel is required to clarify the interlacing process. Finite elements fluid-dynamics simulations of air motion have been performed, solving the Navier Stokes equations for the fluid flow in turbulent regime, due to the high Reynolds number involved in the process [21]. The simulation studies assume that since the size of filament yarn is much smaller than the nozzle, the influence of yarn on air flow can be ignored [22]. The air velocity profile resulting from the simulations indicates that the compressed air from the air inlet impinges upon the opposing wall of the yarn channel, divides in two branches and the air rotates, creating two twin spiral eddies, as shown in Fig.1.6, A. The flow is characterized by high velocity values, around  $10^2$  m/s and vorticity of the order of  $10^6$  Hz, in the case of a yarn channel diameter of 2 mm [21]. Also in the case of a triangular yarn channel cross section with an expansion chamber, the air flow pattern shows the same behavior. In this case, also the Mach number was evaluated and the profile indicates that the flow is supersonic [22].

The same study develops a mathematical model in order to relate the simulation results to the experimentally measured interlacing frequency. It is worth showing this mathematical model, to get an idea of the key parameters considered. The model assumed the interlacing frequency  $k$  to be given by:

$$k = \beta \frac{\rho_a \omega R^2}{\rho_y V_y} \quad (1.2)$$

with  $\rho_a$  the air density,  $\omega$  the air vorticity,  $R$  the yarn channel radius,  $\rho_y$  the yarn density and  $V_y$  the yarn speed.  $\beta$  is a parameter that depends on the

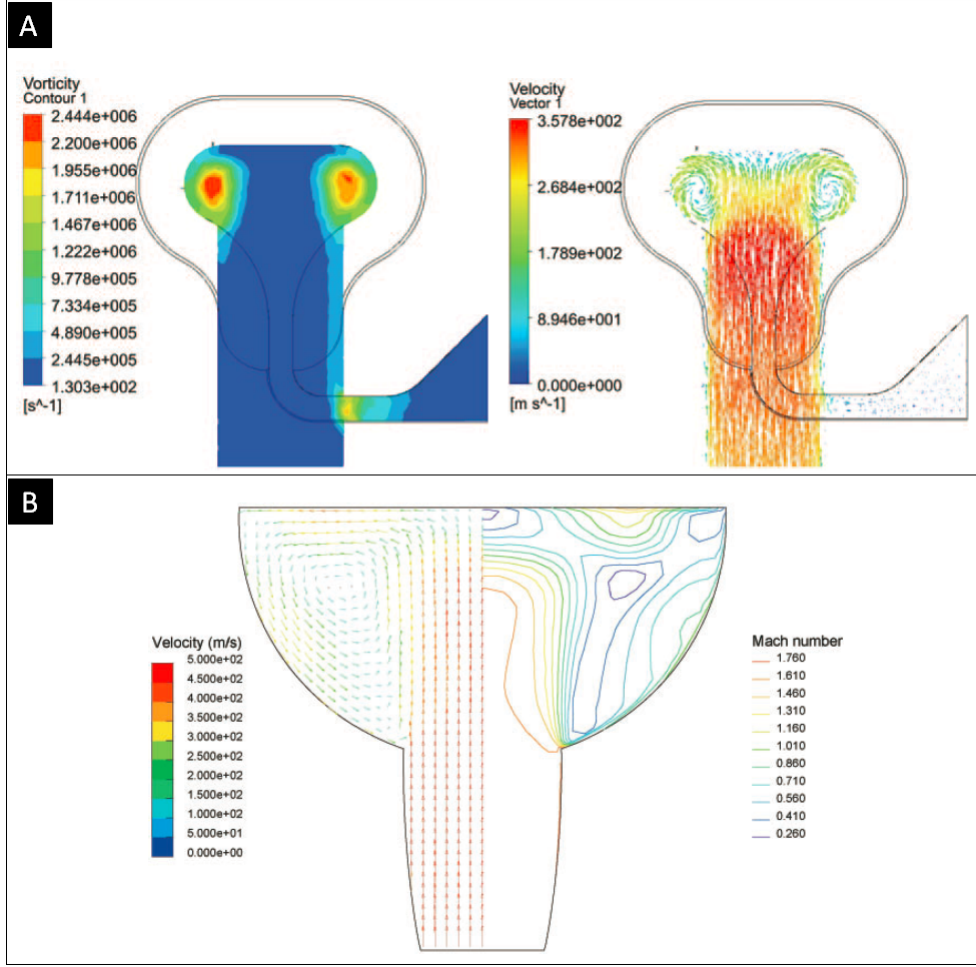


Figure 1.6: Vorticity and velocity distributions, A [21]; flow field characteristics in terms of air speed and Mach number, B [22].

geometry of the interlacer and is obtained from the fit with the experimental measurements. An agreement between the interlacing frequency predicted from the model and the one experimentally measured has been observed.

Even if in literature is not reported any direct observation of the twin eddies described by the simulation, different measurements suggest their actual presence. The first evidence is given by the measurement of dynamic pressure and flow direction in the yarn duct, with Pitot tubes positioned radially and along the yarn duct. This experimental measurement, even if performed in discrete points, suggested the presence of the twin vortices [23].

But what happens when the yarn interacts with the vortices? A patent published by Temco [24], a company producing commercial interlacers, shows that the presence of the yarn in the channel is actually influencing the air motion,

differently from the previous assumptions. The counter-rotating eddies are stable as long as no yarn is present in the channel. When a filament yarn enters the channel, most of the filaments enter one eddy, but this eddy is partially destroyed and the filaments move to the eddy on the other side (Fig.1.7, A). Additionally, the yarn motion causes a back and forth oscillation of the two eddies. This oscillatory movement is non-steady and combined with the effect given by many other small eddies observed in the turbulent flow, causes the random entanglements observed on the yarn. The experimental procedure followed to get those results is not explained in the patent.

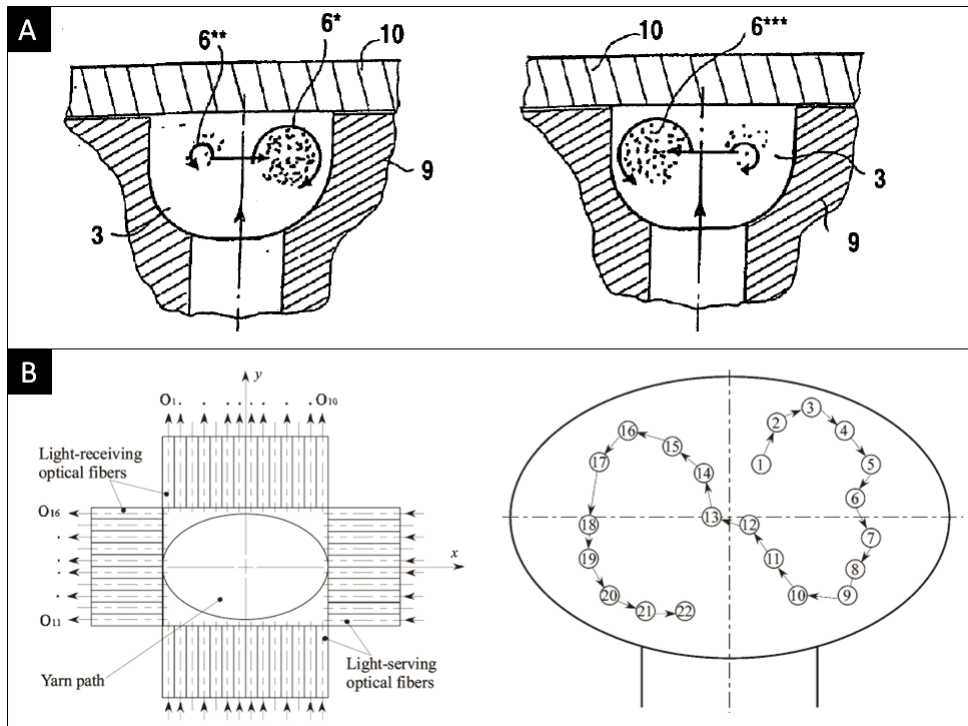


Figure 1.7: Non stationary eddy flow where yarn filaments move from the left to the right eddy, A [24]; arrangement of optical fibers to monitor yarn motion (left); yarn trace monitored in 0.42 ms with a 3 bar inlet pressure and 200 m/min yarn speed in case of an elliptical yarn channel cross section ( $a=1.75$  mm,  $b=1.12$  mm), B [25].

However, other studies suggest a similar behavior. The yarn motion has been observed with a set of optical fibers and photosensors (Fig.1.7, B, left). Comparing also different geometries, the yarn traces an 8 like pattern, as suggested by the previous explanation (Fig.1.7, B, right). As a matter of facts, this pattern results if the majority of yarn filaments are first trapped in the right side eddy, that is partially destroyed and the yarn moves towards the left side eddy, crossing the axis of the air jet. As a result, the higher the air jet crossing

frequency, the higher the number of knots per meter [25]. The importance of traversing the air jet to improve the interlacing performance has been observed also analyzing multiple photographs of the yarn during the interlacing process, using a still camera [26]. A relation between the yarn position, jet crossing and the number of tangles has been demonstrated, even varying the processing parameters.

The yarn motion in an interlacer has been further clarified also using a high speed camera (15 000 fps). The interlacer employed in this case has a yarn duct made of transparent glass, with a circular cross section in such a way that the yarn motion can be monitored both from the top and from the side. The air jet nozzle is perpendicular to the yarn duct. From the analysis of the frames, the following dynamics of interlacing has been proposed. First, the yarn oscillates in the channel, then it is entrapped into the jet and the filaments are opened. At this point, two tangling parts are supposed to be generated at both sides of the opening part. Then the yarn hits the wall in front of the air jet nozzle and moves forward. For a short time, opening and tangling parts are not generated [27]. This dynamics has also been confirmed by a more recent study of the same author, that employing a higher speed camera (40 500 fps) studied the formation of different nips shapes [28].

However, so far this dynamics has not been confirmed experimentally, for example observing on the yarn the actual presence of knots in the expected position. Additionally, the studies were performed always considering an air jet nozzle perpendicular to the yarn channel. Whether the dynamics is the same also with the tilted nozzle geometry used in the company, needs to be further investigated.

### **Variables influencing the process**

The parameters influencing the properties of an interlaced yarn can be divided in *properties of the material* such as yarn density, number of filaments and yarn texturing, *process parameters* like air pressure, yarn speed and tension and *interlacer design*. We will briefly discuss the effects on interlacing following a variation in the parameters just listed.

- **Properties of the material**

Interlacing results from the intermingling of the filaments composing the yarn, for this reason, its efficiency increases with the number of filaments. As a result, when the number of filaments increases, also the number of nips rises because of a better interlacing [29]. Additionally, finer filaments have lower inertia and hence they are more likely to move in the air jet, increasing the interlacing strength. Also the cross section of the filaments



is determinant, since different shapes need different forces to deflect and move the filaments [30].

- **Process parameters**

**Pressure** The main key driving force in the process is the airflow velocity, responsible of opening and entangling the filaments. Increasing air pressure, flow velocity increases such as the number of mingle points inserted into the yarn [31]. However, there is a limit to the rate of increase in intermingling. Over a certain pressure value determined by the geometry of the interlacer, the air flow is too turbulent and instead of intermingling the filaments, they are blown apart [32]. Shock waves in the yarn channel are also affecting the response of interlacing with pressure. A Schlieren imaging technique indicates the formation of a detached shock wave in correspondence to the duct wall, opposite to the nozzle, that is moving further from the wall increasing the inlet pressure (Fig.1.8, A) [33]. Also a finite element simulation of the air flow in an interlacer characterized by an expansion chamber after the air jet nozzle, illustrates the development of shock surfaces (yellow regions in Fig.1.8, C) [22]. When the compressed air flow enters the expansion chamber, it quickly accelerates and forms lower shock surfaces near the nozzle. The following air deceleration causes an additional upper shock surface. The two surfaces limit the effective space for air motion in the interlacer, increasing air speed and hence the interlacing capability. For higher values of air pressure, we observe that the shock surfaces are more and more stable and hence the interlacing frequency ( $k$  in Fig.1.8, B) increases, up to the complete establishment and little variation of shock surfaces with pressure. This behavior explains the steep increase in the interlacing frequency with pressure, followed by a slow variation caused just by the increase of the flow velocity with pressure.

Another parameter influenced by the inlet air pressure is the nips strength, or their resistance to removal. It is assessed counting knots before and after the application of a known load. This value gives an indication of the ability of intermingling to survive subsequent yarn processing. The strength of nips depends on the nips structure.

Microscopic observations indicate that the shape of nips can be classified into four groups: twist, braid, wrap and entanglement nips, according to the arrangement of filaments. Different shapes imply different knots strength. Entanglement nips are featured by the highest filaments disorganization and are the most unlikely to unravel, even under high tension. Increasing air pressure, the proportion of entanglement nips with respect to the other shapes increases; this means that the nips strength increases

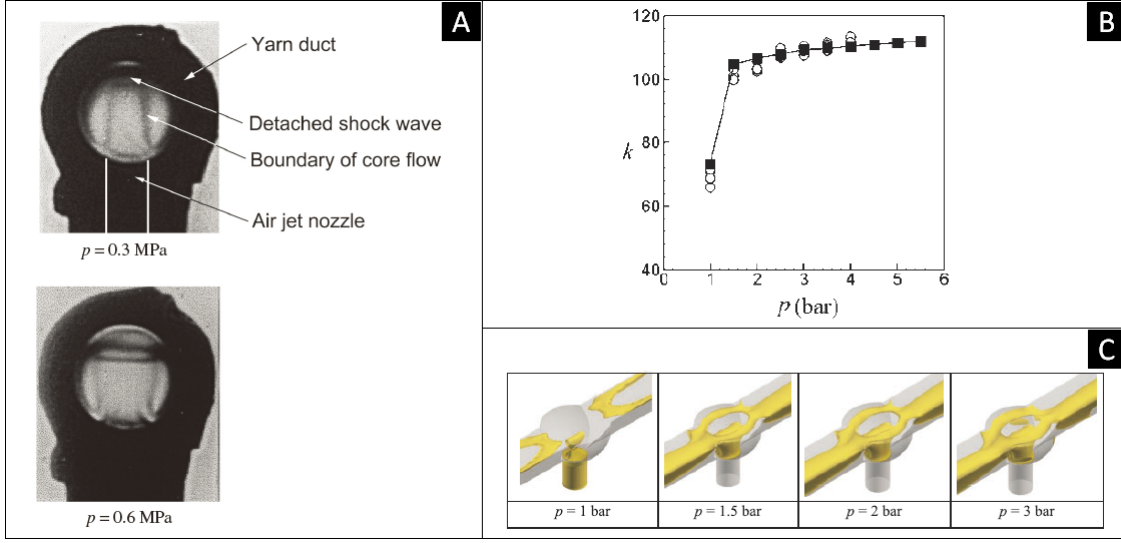


Figure 1.8: Schlieren photographs increasing pressure values, A [33]. Yarn interlacing frequency ( $k$ ) at different inlet pressures, the hollow circles are the experimental measurements, while solid squares represent numerical predictions, B [22]. Corresponding simulated development of shock inside the expansion chamber, C [22].

with the inlet pressure [34].

**Yarn speed** The number of nips per meter decreases with the yarn take-up speed. This behavior can be easily understood if we consider that when the yarn speed is higher, the time for filaments to interact with the air flux shortens and filaments are less likely to open and tangle with each other [35]. Additionally, the strength of tangles is shown to increase with the yarn speed, since the tangling parts tend to be loosed if they stay for a longer time in the processing region [36].

**Yarn overfeed and tension** With overfeed we mean the percentage of feeding speed with respect to the yarn take up speed. In other words, higher overfeed values imply a lower yarn tension in the processing section. As a consequence, filaments are more easily opened and tangled by compressed air. On the contrary, high yarn tension values obstruct the free movement of filaments, resulting in poor mingling.

For this reason, the interlacing frequency increases with the overfeed ratio, as well as the average nips length [34]. The increase in nips frequency occurs just up to a certain overfeed percentage (depending on the interlacer geometry), since above that value the tension is too low and the yarn may move out of the potential action of air; therefore the nip frequency decreases. Additionally, increasing the overfeed to improve the interlacing frequency is not advisable, because percentages of overfeed

around 5% show the occurrence of big filaments loops and irregularities in the open sections [35]. This considered, the optimal overfeed ratio is found to be around 1% [37].

The overfeed ratio is found to be the most significant processing parameter influencing the number of knots per meter [36]. So, tension needs to be controlled during the process, since yarn tension fluctuations affect the properties of the interlaced yarn.

- **Interlacer geometry**

Different parameters in the geometry of an interlacer can be varied, such as the yarn channel and nozzle length, diameter and shape. The dependence of the interlacing performance from these geometrical variations is still not fully understood and characterized. Some studies evaluated the interlacing capability with different channel cross sectional shapes.

Rounded yarn ducts, elliptical or circular, have been compared with cornered yarn ducts, triangular or squared. The motion in a round yarn duct is smoother and the air flow pattern is regular, hence the yarn is easier to open and tangle and the interlacing frequency is higher. On the other hand, in a cornered air duct airflow stagnates and the yarn stays there for a longer time, causing a higher knots strength. The best compromise has been found to be an oblate elliptical and inverse triangular geometry [35], [38].

Another study evaluated the critical inlet pressure for interlacing, varying the ratio of nozzle and yarn channel diameters. A lower ratio implies lower critical pressures, since the air jet has more space for expansion and lower inlet diameters imply higher air speed values. Increasing the size of the air nozzle, on the other hand, increases the knots strength, at the expense of a greater air consumption. Higher nozzle diameters are hence required with higher density yarns (more filaments are involved in the process).

In the first interlacers, the angle between the yarn channel and the air jet nozzle was always aimed at  $90^\circ$ . In this configuration, the incoming airflow is divided in two equal branches. A slight inclination of the nozzle in the direction of yarn movement results in unequal division of air flow. In this way, a forwarding action is imparted to the yarn, causing a slight overfeed that results in an initial improvement of the interlacing frequency. According to the geometry chosen, optimal inlet angles have been established around  $10 - 15^\circ$  [22]. The tilting of the nozzle produces also two unequally strong eddies in the yarn channel, where the forward eddy has a stronger effect than the rear eddy [24].

### **On-line yarn evaluation**

In textile industries is recognized the need of an on-line sensing technique, that allows to monitor continuously the regularity of interlacing. Few studies moving in this direction are reported in literature, but none of them is performed in the operating conditions employed by the company, in terms of yarn tension (around 70 cN) and yarn speed (from 1000 to 2000 m/min). The first technique proposed to evaluate on-line the interlacing capability is an optical sensor, based on the use of a laser and a linear CCD. A good evaluation of the interlacing frequency was performed, compared with the distance between knots measured manually, up to a yarn speed of 800 m/min [39]. However, the low yarn tension (5 cN) facilitates the observation of yarn profile variations with this optical technique. Whether this approach is suitable even with higher yarn tension values, has not been verified. A more recent study employs the same technique analyzing not only the average knots distance, but also the individual nips to evaluate how well formed the nips appear. Increasing the yarn speed, the analysis worsens due to less controlled yarn vibrations [40]. Even if this technique is promising both in establishing on-line the mean entanglements per meter as well as the shape and regularity of knots, it is too expensive to be implemented industrially.

Another study investigates and compares a capacitive and an optical on-line analysis to evaluate the evenness of a yarn profile. In this case the yarn is parallel and the study aims to identify inhomogeneities in the material. The optical sensor consists of a LED and a photodiode and a maximum yarn speed of 120 m/min is considered. The comparison of the frequency spectra of the signals acquired with the two sensors indicate the same characteristic frequency components, caused by recurrent defects occurring in the yarn. However, this preliminary study was not applied to the interlacing process and was limited to a frequency analysis. The technique needs to be investigated to evaluate for example also the regularity in the knots distance [17].

# 2

## High speed imaging

### Contents

---

<b>2.1</b>	<b>Materials and methods . . . . .</b>	<b>24</b>
2.1.1	Experimental setup . . . . .	24
2.1.2	Image processing . . . . .	25
<b>2.2</b>	<b>Experimental measurements . . . . .</b>	<b>26</b>
<b>2.3</b>	<b>Flow visualization . . . . .</b>	<b>30</b>
<b>2.4</b>	<b>Chapter summary . . . . .</b>	<b>33</b>

---

**Overview** The previous chapter indicated that many physical phenomena are involved in interlacing. Among all these processes it is difficult to discriminate the key parameters responsible for the knots formation. For this reason, we decided to look at the yarn motion during interlacing, to highlight the dynamics involved in the process.

High speed videos have already been performed to study the yarn motion in an interlacer with the air jet nozzle perpendicular to the yarn duct and these measures suggested a possible dynamics of knots formation [27]. However, most textile industries use tilted air jet nozzles ( $\beta$  in Fig.1.5), that improve the regularity and efficiency of interlacing [22]. It is still not clear if the dynamics of interlacing suggested in [27] is valid also with this tilted geometry.

Following this reasoning, we decided to perform a high speed imaging analysis of the yarn during interlacing.

After that, a preliminary investigation of the air flow pattern into the interlacer has been performed, mixing the fluid with a tracer and monitoring it by means of a high speed video.

## 2.1 Materials and methods

### 2.1.1 Experimental setup

We used as test material a raw Nylon 6 textured multi-filament yarn (1000 dtex /42 filaments). The interlacer employed is produced by Temco; the yarn channel length is 24 mm and its diameter 4 mm. The air jet nozzle is tilted of  $10^\circ$  with respect to the normal to the yarn channel ( $\beta$  in Fig.1.5). The nozzle is 20 mm long and has an elliptical cross sectional shape of 2 mm and 4 mm minor and major axes.

A pressure gauge is placed at the beginning of the nozzle to monitor the inlet pressure. We covered the interlacer with a plexiglas lid, as shown in Fig.2.1.

The high speed camera was the model SC2+ (Edgertronic) with a maximum frame rate of 17 000 fps (resolution:  $192 \times 96$  pixels). The resolution increases lowering the frame rate ( $320 \times 240$  pixels at 6700 fps).

Initially, the measurements were performed in the laboratory, on a pilot testing setup. During these first measurements, the yarn was not guided, but just set in motion by compressed air. Increasing the value of compressed air, the yarn speed increases. For example with an inlet pressure of 4.5 bar the yarn speed was of 500 m/min, increasing to 700 m/min with 6 bar inlet pressure.

The successive measurements were performed on the industrial plant, where two guiding rolls allow to monitor and control the yarn motion, in terms of yarn tension (70 cN) and yarn speed. The inlet pressure was 6.5 bar. We considered

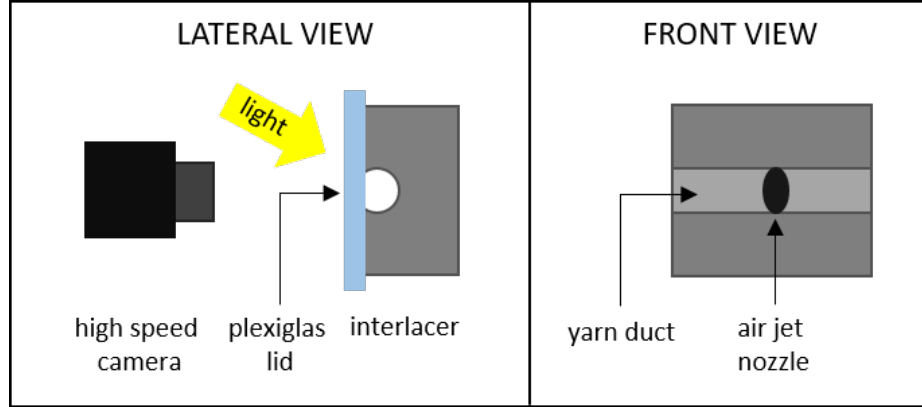


Figure 2.1: Experimental setup for the high speed imaging of yarn motion.

six yarn speed values (400, 600, 800, 1000, 1200 and 1500 m/min), associated to different frame rates of the camera (8000 fps for 400 and 600 m/min, 10000 fps for 800, 1000 and 1200 m/min and 12000 fps for 1500 m/min). In this way we guaranteed a 2 mm maximum displacement of the yarn from one frame to the following one, in order to reconstruct the dynamics in the whole channel. To assure a short time exposure (around  $10 \mu s$ ), we used high intensity LEDs. A short time exposure is preferable to obtain the most possible fixed image of the moving yarn. The recording time was adjusted according to the yarn velocity (from 1.2 s to 2 s), analyzing 20 meters of running yarn in about 15000 frames.

### 2.1.2 Image processing

The high speed videos were analyzed using Matlab®2018. We acquired the frames of the video (Step 1 in Fig.2.2) and then we reconstructed the yarn profile, frame by frame. First, we converted each image into a grayscale, in such a way that we can attribute to each pixel an intensity value (Step 2 in Fig.2.2). Then, we aim to discriminate the yarn from the background and the common way to achieve this aim is thresholding.

The basic idea is to select an optimal grey intensity threshold to separate the object of interest from the background, based on their grey-level distribution. In this way, binary images are created, turning all pixels below or above the threshold to zero or one. One method to establish this threshold value is called Otsu method and it assumes that the image contains two classes of pixels, one for the foreground and one for the background, following a bimodal histogram. The method aims to minimize the intra-class variance, that is the weighted sum of variances of the two classes. The threshold that gives the weights minimizing the variance is chosen [41]. We used the Otsu's algorithm

to discriminate the yarn from the background (Step 3 in Fig.2.2). The profile of the yarn reconstructed in this way was further smoothed fixing a threshold on the derivative of the profile. In this way, we neglect the sharp profile variations caused by an irregular illumination or by other defects in the image (Step 4 in Fig.2.2). This image processing procedure allows to reconstruct the yarn profile over time.

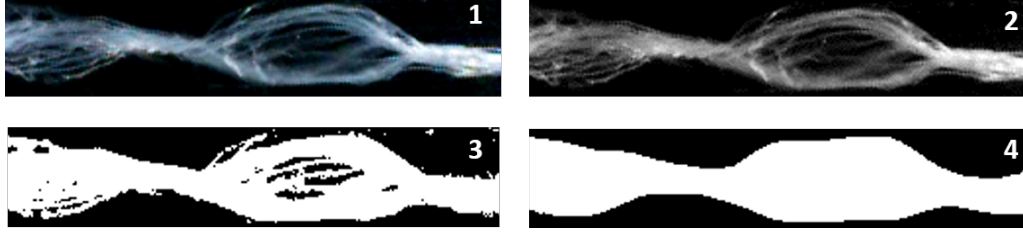


Figure 2.2: Steps in the frames processing procedure to reconstruct the yarn profile.

## 2.2 Experimental measurements

We performed the first high speed videos on the pilot experimental setup in the laboratory, where the yarn is set in motion just by compressed air. In Fig.2.3 is reported a typical sequence of frames extracted from a 8000 fps video. We observe that in certain moments the yarn oscillates, for example in steps 4, 5, 6, while in other instants the filaments are opened in front of the air jet nozzle, for example in steps 2 and 7.

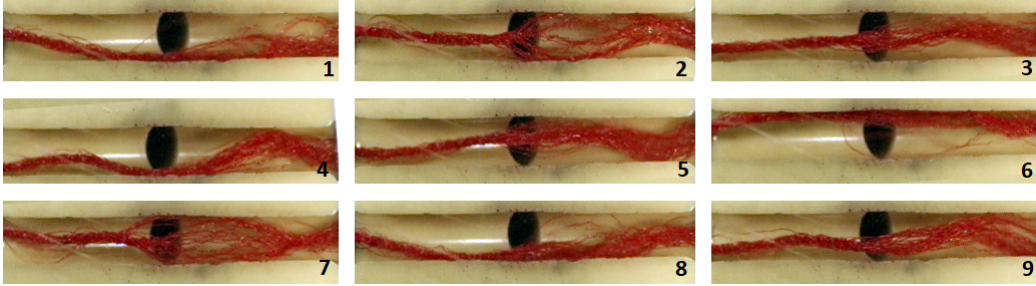


Figure 2.3: Sequence of frames extracted from an high speed video.

This behavior suggested us an hypothetical dynamics of knots formation, similar to the one proposed in [27]. The filaments of the yarn interact with the twin vortexes that are formed in proximity of the nozzle and are opened and intermingled with each other. In this way two knots should be created: one before and one after the nozzle, as in step 7 of Fig.2.3. Then, as the knot is



passing in front of the nozzle, the vortexes do not succeed anymore in opening the filaments in that point. So, in this moment, the yarn is just moving forward oscillating, until the knot overcomes the nozzle and the filaments are opened again by vortexes.

As a first test of this hypothesized dynamics, we decided to verify if the knots are actually created in the positions where we are predicting to find them from the video analysis. So, we considered a white parallel yarn and we marked it with different colors, in order to relate the frames of the video to the corresponding yarn segment. In Fig.2.4 we observe a sequence of frames extracted from the video, where we recognize the formation of four knots, identified by the red arrows in Fig.2.4. The knots in those positions are actually observed also in the post processed yarn.

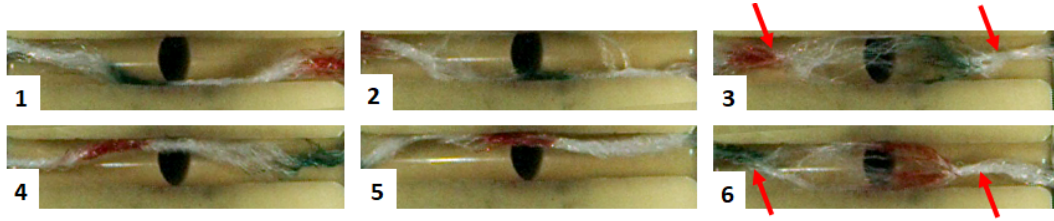


Figure 2.4: Sequence of frames extracted from the high speed video of the marked yarn. Red arrows: positions of knots.

As a result of this encouraging confirmation of our hypothesis, we decided to further validate it. As a matter of facts, with the marker we can verify the dynamics just on few samples since we need to check and compare manually, frame by frame, the video with the final yarn. This is the reason why we were looking for a parameter that can be extracted from each frame and that allows us to study the dynamics of interlacing over the whole video. We identified the yarn diameter as the key parameter. Indeed, according to the dynamics described previously, as the knots are forming the filaments are opened and the width in front of the nozzle is large. Afterward, the knot moves to the same position, in front of the nozzle and in that moment the width is smaller than previously. As a result, the width of the yarn in front of the nozzle should vary in time periodically, at the frequency of interlacing. To verify this hypothesized periodicity of width variation, the yarn speed needs to be regular. However, up to now, we could not monitor neither the position, nor the speed of the yarn. For this reason, we decided to perform the high speed analysis of interlacing on the industrial plant. In this case, the yarn motion is stabilized by two guiding rolls, placed before and after the interlacer. So, we took a 2s high speed video and monitored the width of the yarn in front of the nozzle in time, frame by frame. The evaluation of the width of the yarn in front of

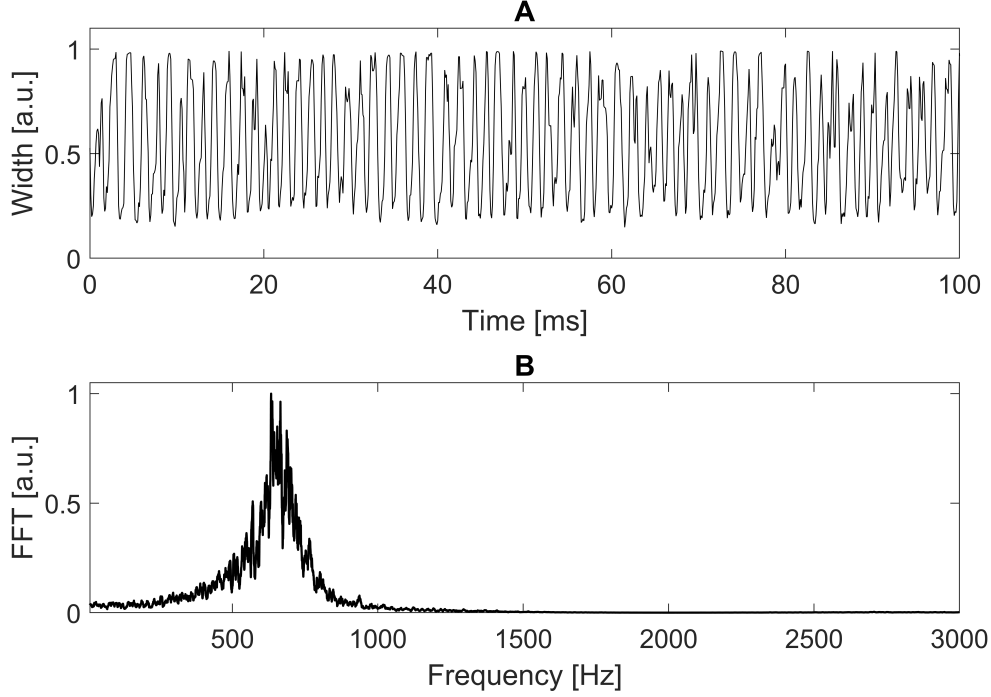


Figure 2.5: Width variation in time in front of the nozzle, for a yarn running with a speed of 800 m/min (A), FFT of the whole 2 s signal (B).

the nozzle is bothered by the black nozzle (Fig.2.4). To overcome this issue, we used a brownish interlacer and white yarn, easily discernible on the dark background.

In Fig.2.5 (A) we observe that the width changes periodically in time, as expected. The FFT of the width in time over the whole 2 s measurement indicates a peak in the frequency distribution (Fig.2.5, B). To further validate our hypothesis, we still need to check if this frequency component is related to the interlacing process.

A change in the yarn speed during interlacing causes a variation in the distance between knots. Therefore, we decided to repeat the measurement for different yarn speed values (ranging from 400 m/min to 1500 m/min). Each peak in the frequency spectrum is characterized by a central frequency and a width. The knots distance is indeed distributed around a mean value and the width of the distribution represents the process regularity.

Spectral leakages are not affecting this width, since in this case the main lobe width is 1 Hz (given by  $2/T$ , for a rectangular window), while the peak broadening detected is much higher. A cross check of this statement has been performed also windowing data (using Hanning and Blackmann-Harris window);

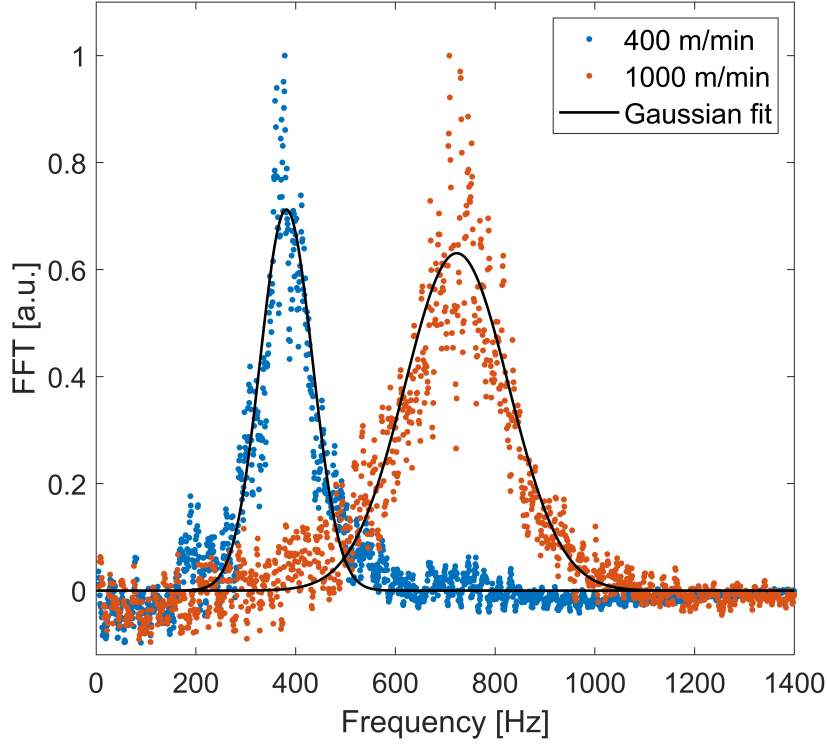


Figure 2.6: FFT of the width variation in time for two values of yarn speed (400 m/min and 1000 m/min).

no variation in the width of the frequency distribution has been observed, indicating that spectral leakages are not causing the detected peak broadening [42]. We fit a Gaussian to data, to have an estimate of the central frequency and width of the distribution.

Fig.2.6 shows the fitting curves for two values of yarn speed; we observe that frequency increases linearly with the yarn speed (Fig.2.7, A). Indeed, fitting a polynomial to data, the second degree term results 3 orders of magnitude lower than the linear term.

This demonstrates that the presence of the yarn and its speed influence the fluid dynamics in the channel (vortexes and shock waves), while in numerical simulations and experimental analyses the effect of the yarn has always been neglected [22].

From the central frequency and the yarn speed values, we can easily estimate the spatial frequency, i.e. the distance between knots. The distance obtained from the analysis of the high speed videos is in agreement with the distance between knots measured off-line on the interlaced yarn (see Fig.2.7, B).

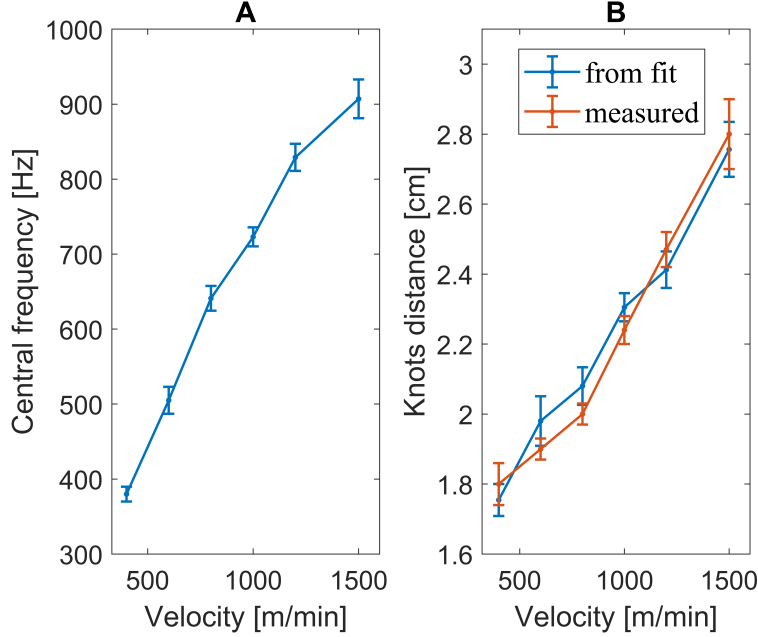


Figure 2.7: Central frequency of the Gaussian distribution increasing yarn speed (A); distance between knots estimated from the high speed analysis (blue) compared with the distance measured on the interlaced yarn (red) (B).

### 2.3 Flow visualization

In the previous chapter, we indicated that in literature is not reported any direct observation of the vortexes. FEM simulations predicted the occurrence of the twin eddies and also the yarn motion suggested their presence. However, due the hypothesized fundamental role of vortexes in the interlacing process, it would be interesting to visualize the fluid motion. To have just a preliminary information using the available experimental setup, we decided to monitor the fluid just at the exit of the interlacer.

Since the light scattered from the fluid molecules (Rayleigh scattering) is extremely weak, in order to visualize the flow, small tracer particles need to be injected. The implicit assumption is that the motion of the tracer follows the fluid velocity. This approximation holds when we are dealing with not-turbulent conditions: for example in compressible flow with shock waves, particles of finite mass and size cannot follow such an abrupt change [43]. The size and mass of tracers play a fundamental role: the size should be small enough to achieve good tracking, but also large enough to scatter sufficient light signal.

As a matter of facts, since we are in the Mie scattering regime, the intensity

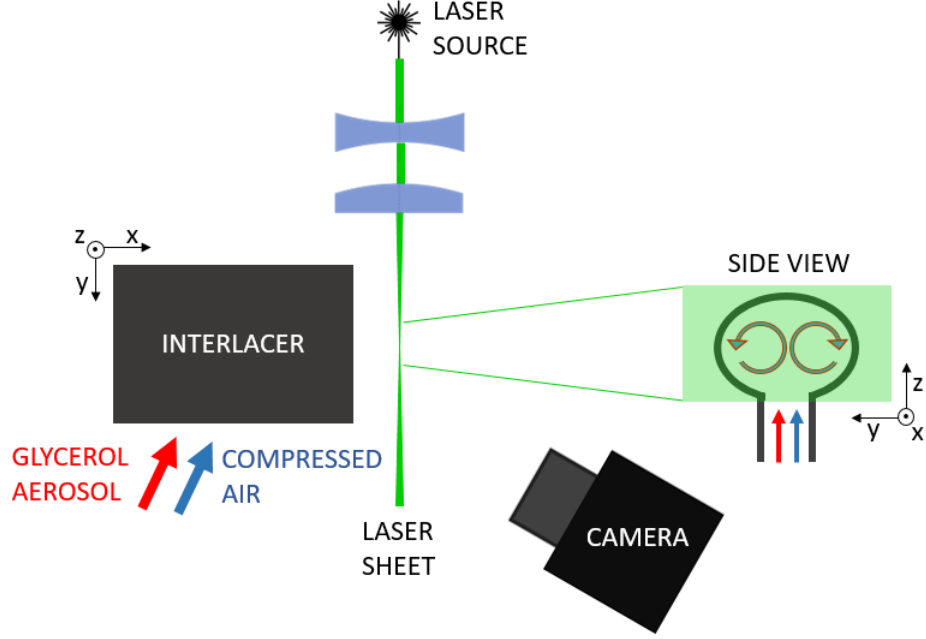


Figure 2.8: Experimental setup to monitor the flow motion at the interlaser exit.

of forward scattering increases with the particles size [44]. Recommended particles diameters range between  $0.1$  to  $20\ \mu\text{m}$ . Additionally, to guarantee an optimal flow visualization, particles should be seeded into the flow with steady and spatial uniform concentration. Too high density causes a decrease in the spatial resolution, if we are interested in tracking single particles to reconstruct the flow velocity profile.

In our case, the tracer is obtained heating glycerol, since the resulting aerosol particles are reported to have a mean diameter ranging from  $100$  to  $600\ \text{nm}$  [45]. We added this fog to the compressed air at the entrance of the interlaser nozzle (Fig.2.8). Once mixed the tracer to the fluid, we need to visualize it with appropriate lighting. In our case, we are interested in the cross section of the fluid at the exit of the interlaser. So, illuminating the flow field by a sheet of light, we can examine discrete slices of the flow. We used a green laser and then by means of a divergent and a cylindrical lens we generated the laser sheet. The cylindrical lens is the key component to focus the light sheet to the desired thickness [46]. The divergent lens determines the width of the sheet, of about  $6\ \text{mm}$  for our application. We focused the resulting laser sheet at the exit of the interlaser.

The vorticity values reported in literature (around  $10^6\ \text{Hz}$ ) indicate that with the available high speed camera (acquisition rate in the  $\text{kHz}$  range), we can not follow the flow dynamics. In other words, the resulting intensity profile

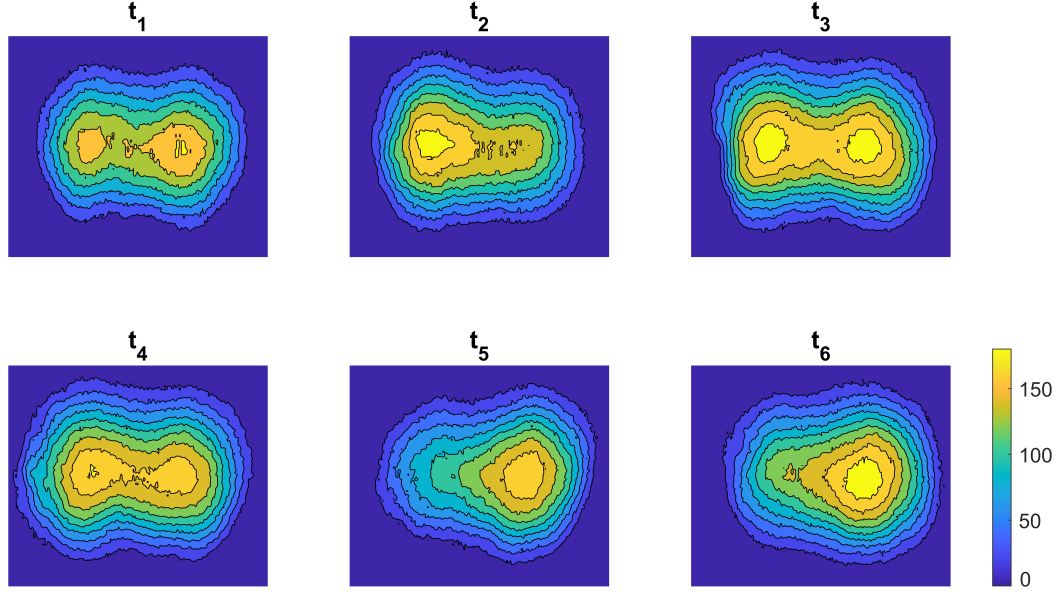


Figure 2.9: Sequence of frames extracted from the high speed video (1000 fps), where  $t_2 = t_1 + 1\text{ms}$  and so on. The colorbar indicates the intensity of the scattered green light (blue-low intensity, yellow-high intensity).

will be given by multiple particles scattering and we measure the sum of the single particles contributions. In the working conditions, the low light intensity allowed us to use a shutter speed of 0.5 ms and a frame rate of 1000 fps. We placed the camera in such a way to detect the more intense forward scattering (Fig.2.8). Since we are interested just in the green light, in order to reduce other sources of noise, we extracted the green component from each frame.

In Fig.2.9 is reported a sequence of frames, where the colorbar indicates the intensity of green light. The higher the particle concentration, the higher the scattered intensity (yellow regions in the plot). We observe the occurrence of two high intensity spots, that could be given by a high particles concentration in those regions due to the presence of the vortexes. We observe that the flow is not stable, suggesting that the vortexes are periodically created and destroyed.

This is just a proof of principle result, that needs to be further improved. We need to increase the light intensity to lower the shutter speed and enhance the acquisition frame rate. In this way, we can better investigate the temporal flow dynamics and not just an integral behavior. The final aim is to track the single particles to reconstruct the flow velocity profile. Additionally, a plastic transparent interlacer could be employed to visualize the flow in the yarn channel.

## 2.4 Chapter summary

A high speed imaging analysis of the yarn motion allowed us to understand the dynamics of knots formation in an interlacer. We found that the width of the yarn in front of the nozzle is a key parameter to monitor on-line the process and to evaluate the regularity in the distance between knots. This analysis pointed out that the interaction between yarn and vortexes is fundamental in the knots formation process.

The flow field and the exit of the interlacer has been visualized adding a tracer to the moving compressed air. The fluid cross section, monitored with a laser sheet and a high speed camera, indicated the occurrence of two unstable vortexes. This first, preliminary result needs to be further improved to follow the flow dynamics.





# 3

## Vibration analysis

### Contents

---

<b>3.1</b>	<b>Motivation of the vibration measurement . . . . .</b>	<b>36</b>
3.1.1	Air flow-yarn interaction . . . . .	36
3.1.2	Shock waves-yarn interaction . . . . .	38
<b>3.2</b>	<b>Design of the experimental setup . . . . .</b>	<b>40</b>
3.2.1	Lower limit of detection . . . . .	41
3.2.2	Resonance frequencies of a screwed plate . . . . .	41
3.2.3	Mechanical filters . . . . .	49
<b>3.3</b>	<b>Vibrations induced by the interlacing yarn . . . . .</b>	<b>57</b>
<b>3.4</b>	<b>Chapter conclusions . . . . .</b>	<b>61</b>

---

**Overview** The interaction between the yarn and the compressed air jet is supposed to cause a modulation of the air flow pattern. If this modulation is responsible of the periodicity of interlacing, its detection could allow to monitor the process. This idea is developed in this chapter, starting with a characterization of the yarn interaction with the air flow and with the shock waves. Then, we will focus on the main issues related to the design of the experimental setup, linked to the sensor saturation due to resonances. A theoretical model to explain and predict the resonances and their damping will be described. Finally, the vibrations induced by the interlacing process will be measured and analyzed.

### 3.1 Motivation of the vibration measurement

#### 3.1.1 Air flow-yarn interaction

The interlacing process results from the interaction of the multi-filament yarn with the impinging air flow. Several studies have been performed to investigate the air flow motion in an interlacer, assuming that since the yarn is small with respect to the diameter of the yarn channel, its influence on the air flow can be ignored, as explained in Sec.1.2.2. Actually, considering the geometry of the interlacer we are using, the channel diameter is just 4 times bigger than the yarn section and so we can not exclude the possibility that the yarn interacts and modifies the air flow.

In order to verify this concept, we performed a 3D FEM simulation with COMSOL Multiphysics®, CFD module in the laminar flow approximation. This approximation is required to reduce the computational time and ensure the simulation convergence (since a 3D model is required), but in any case it is representative of the air flow behavior for low inlet air speed values. In pipes, laminar flow occurs when the Reynolds number is below a critical value of about 2000 [47].

The Reynolds number is defined as:

$$Re = \frac{\rho v_{in} D}{\mu} \quad (3.1)$$

with  $\rho = 1.2 \text{ kg/m}^3$  the air density,  $v_{in}$  the air speed,  $D = 4 \text{ mm}$  the pipe diameter and  $\mu = 1.78 \cdot 10^{-5}$  the dynamic viscosity. For an inlet air speed of  $4 \text{ m/s}$  it is equal to 1075, meaning that the regime is laminar. So, in the simulation we set this input air speed value.

The geometry of the simulated interlacer is characterized by the same dimensions of the one employed experimentally (Sec.2.1.1). Setting an inlet speed of  $4 \text{ m/s}$ , we compared the fluid motion in the yarn channel; in Fig.3.1 (A) is

shown the resulting airflow pattern in the whole 3D geometry. The simulation was performed with and without an object interfering with the air flow, characterized by a diameter 4 times smaller than the yarn channel. We are considering a raw simplification of the real situation, since the yarn is not a rigid object and it is moving with the air flow. It is a first approximation, to have an idea about the interference between the air flow and an object.

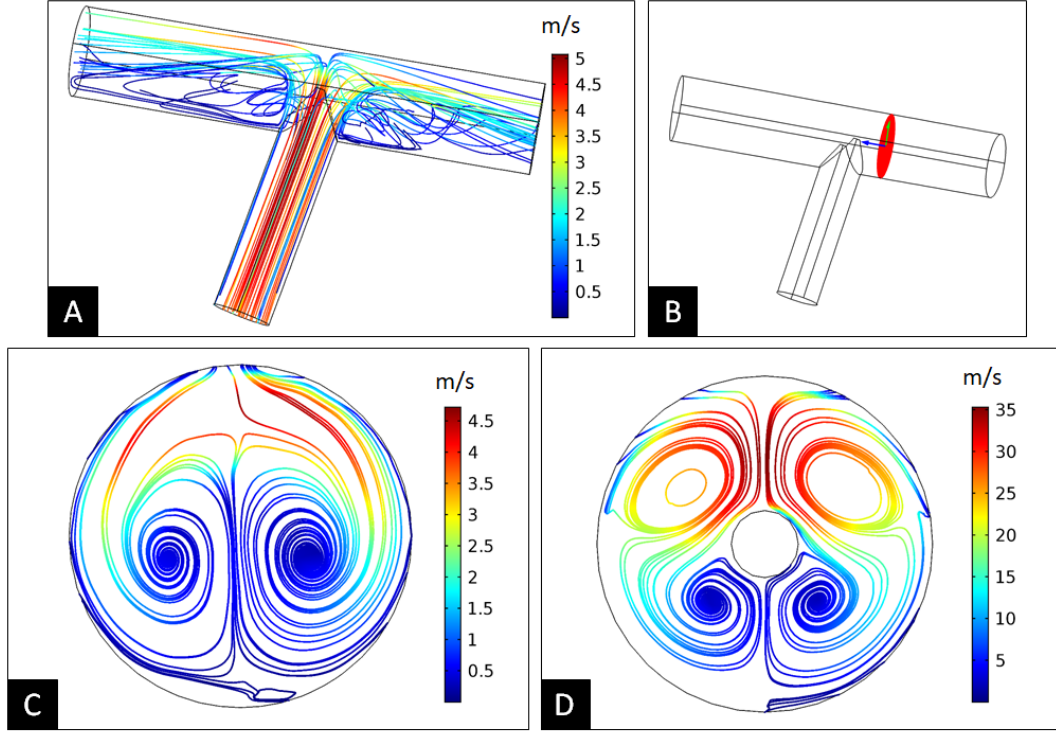


Figure 3.1: Simulation of fluid motion in laminar flow conditions with an input speed of 4 m/sec. Streamline velocity field in the 3D geometry (A). Indication of the cut plane 3 mm at the right of the nozzle (B) where the velocity streamlines are extracted (C). Resulting flow velocity pattern also when an object is placed in the yarn channel (D).

Looking at the streamline velocity in a cut plane orthogonal to the yarn channel (Fig.3.1, B), we observe the occurrence of two twin vortexes, with two high pressure regions in the middle of the channel, when no object is interacting with the flow (Fig.3.1, C). The interaction of the air flow with the rigid object placed in the middle of the channel, causes a modification of the air pattern (Fig.3.1, D).

This first result let us hypothesize that the yarn in the channel creates a periodic modulation of the air flow. This component adds to the one measured in absence of the yarn by means of Pitot tubes [33].

The hypothesized flow variation could be responsible for the periodicity of the interlacing process. This is the first reason why we decided to monitor the vibrations induced by a possible air flow modulation.

### **3.1.2 Shock waves-yarn interaction**

The second motivation is related to the interaction of the yarn with the shock surfaces occurring in front of the air jet nozzle. It has been demonstrated, both by means of a numerical simulation [22] and with a Schlieren imaging technique [33] the occurrence of a detached shock wave in front of the duct wall opposite to the nozzle.

The air flow in the nozzle reaches a supersonic regime and moving into a higher diameter duct (yarn channel's diameter is twice the nozzle), the speed decreases, approaching the speed of sound. As the wave is propagating, its velocity decreases; so, impulses from the back will reach the front causing a piling up of waves, also called shock waves.

The shock waves are characterized by high pressure values, of the order of some bar [48]. The shock surface limits the effective space in the yarn channel in front of the nozzle, enhancing in this way the vorticity strength. This is the reason why the frequency and efficiency of interlacing, in terms of knots strength, are enhanced by the presence of the shock waves [22].

We hypothesized that the interaction of the oscillating yarn with the shock front causes a temporary perturbation of the shock stability. In fact, a shock refraction and damping occurs when it interacts with a disturbed interface [49]. It is also well known that obstacles placed in the path of a moving shock can diffract and attenuate the shock waves transmitted through them. In general, shock waves are partially reflected and partially transmitted at the interface between two media, depending on the acoustic impedance mismatch at the boundary [50]. In some particular cases, such that of a shock wave front diffracting on a perforated wall, the flow passes through the perforations and there are no shock reflections, only transmitted waves. All these studies have been performed in the framework of the shock waves attenuation, for the protection against blast waves caused by explosions in mine and transportation tunnels and vents [51]. In the particular case of a porous compressible material, that resembles the structure of the interlacing yarn, it has been observed that a porous material can reduce the reflected shock wave and attenuates the transmitted one [52].

In the same way, we expect to observe a modulation in the shock wave as it interacts with the running yarn, due to shock waves absorption. This process could create periodic favorable conditions for interlacing. As a further proof, we decided to investigate what happens to a shock wave when a small object

is placed in the air path. To that aim, we simulated a De Laval nozzle, that consists of a pipe with a constriction in the middle. The constriction induces a sudden increase in the flow speed, creating a region of supersonic flow. Unlike a subsonic flow, the supersonic one accelerates as the area gets bigger. This region of supersonic acceleration is ended by a normal shock wave, where energy is dissipated and the speed decreases, returning to subsonic conditions. We simulated the behavior of a de Laval nozzle in standard conditions and with an object placed after the position where the shock was formed without the object. In both cases the same initial parameters, as pressure and inlet velocity, were considered. The 2D simulation was performed using a Spalart–Allmaras turbulence model, implemented in COMSOL Multiphysics®. It is used to model gas flows at high Reynolds number where the velocity magnitude is comparable to the speed of sound. The results, in terms of Mach number, are reported in Fig.3.2.

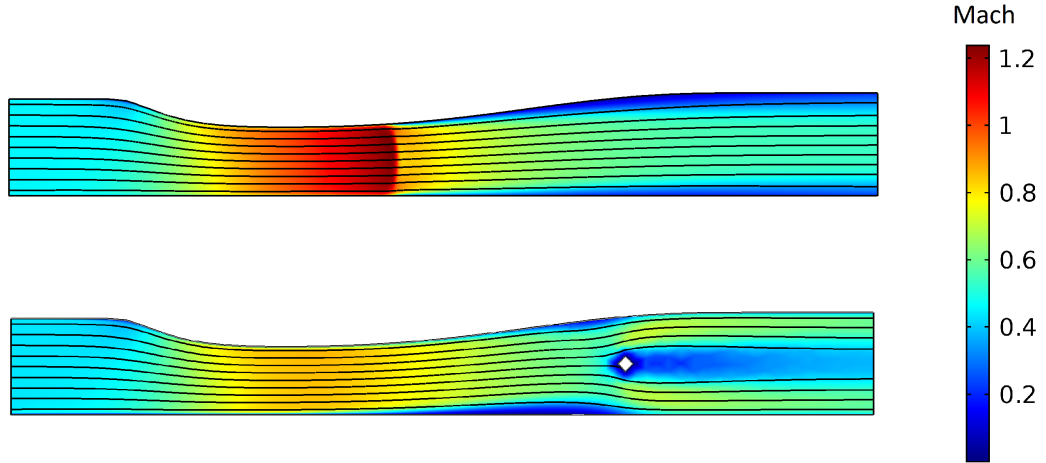


*Figure 3.2: FEM simulation of fluid motion in a de Laval nozzle. Mach number in different points of the nozzle (upper figure). Mach number when an object is placed in the nozzle (lower figure). Inlet air flow speed: 150 m/s, air pressure: 1.2 bar.*

We observe that the presence of the object prevents the formation of the shock wave, even if the object is small compared to the pipe size (about 6 times smaller).

This result indicates that also the interaction of the yarn with the air flow could cause a periodic modulation of the shock waves.

The hypotheses described so far motivated us to monitor the pressure waves related to the interlacing process, measuring the induced vibrations. The vibration analysis is a commonly employed technique in monitoring health of industrial machines, due to its long term stability [53]. The measurement of

vibrations is preferred with respect to the use of pressure transducers, since they require tapping into the piping, creating in this way a system modification. On the other hand, the analysis of vibrations is a non-intrusive method. Additionally, this technique is widely employed in monitoring the fluid motion, since its performance is not influenced by the physical properties of the fluid under investigation [54]. In general, the transducers employed in vibration analyses convert the solicitation into an electrical signal, which is a function of the mechanical vibration in terms of frequency and amplitude.

### 3.2 Design of the experimental setup

The characteristic vibration frequencies induced by the flow can be monitored fixing the accelerometer on a plate positioned in front of the yarn channel. The plate is set in vibration by the air flux and by the yarn; for this reason the material composing the plate needs to be elastic enough to follow all the solicitations, i.e. it should be characterized by a low Young's modulus and by a proper geometry. To start, we chose an aluminum plate 3 mm thick, 30 mm wide and 40 mm long. The accelerometer is screwed on the plate, in front of the air jet nozzle, as shown in Fig. 3.3 (A, B).

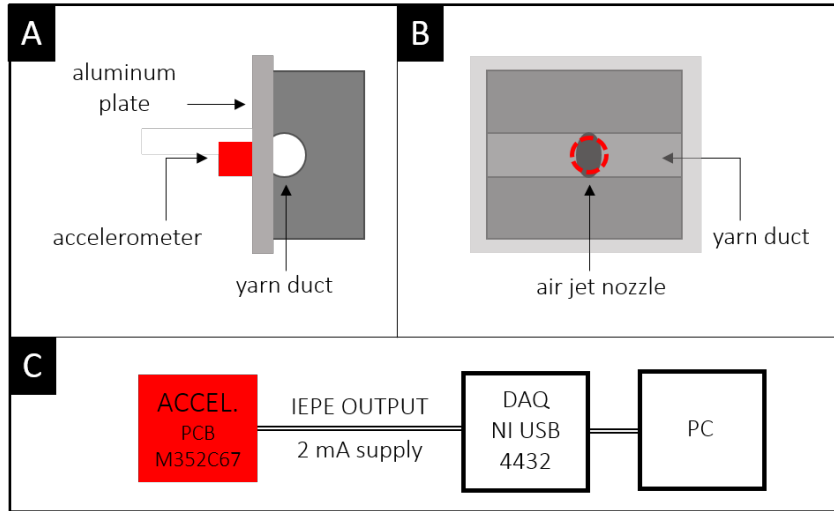


Figure 3.3: Scheme of the vibration measurement setup; lateral view (A) and front view (B). Vibration acquisition procedure (C).

A PCB M352C67 accelerometer has been selected, due to its wide measurement range ( $\pm 50$  g *pk*), flat frequency response up to 20 kHz (resonance frequency  $\geq 30$  kHz) and high sensitivity (100 mV/g). We used the NI USB-4432 data acquisition board, coupled to the PC with a LabVIEW interface, that is used

also to analyze the signal (Fig. 3.3, C).

We wrote a data analysis software in LabVIEW, that converts the output voltage in acceleration (100 mV/g of sensitivity) and then performs the FFT of the signal using a Hann window (1 Hz resolution, acquiring 200 kSamples with a 200 kHz sampling frequency). Then, it calculates the Power Spectral Density (PSD) of the signal and this value is averaged each time with the one calculated in the previous cycle. 60 averages are performed to reduce the overall noise; as a result, the measurement lasts one minute. Averaging allows to reduce random contributions and enhances the signal, it is commonly employed as a way of smoothing the spectrum of the random signals [55]. The averages are performed considering the PSD of adjacent time segments; using a Hann window an overlap of 66% is required not to lose signals information, since the time window reduces the weight signal to zero at the connection of the adjacent segments. However, for our purposes, the partial loss of time signal is not affecting the information we are looking for.

The PSD allows to evaluate the signal amplitude, that is calculated from the square root of the PSD, with three multiplication factors. The value is multiplied by  $\sqrt{2}$  since it is a rms value, by 2 since the spectrum is single sided and by  $\sqrt{1.5}$  that accounts for the distortion effects caused by the Hann window. Having in mind this experimental setup, first we need to understand if it is suitable to monitor the desired vibrations and which is the best plate geometry to avoid resonances in the frequency range of interest. Then, we will evaluate different sensor mounting configurations to improve the measurement.

#### 3.2.1 Lower limit of detection

First, we decided to test the lower limit of detection of our system, in order to be sure that our experimental setup succeeds in sensing the hypothesized modulated shock waves. We positioned a loudspeaker in the yarn channel and measured the induced vibration. We chose the lower detection limit of the system as the solicitation that causes a vibration detected through the accelerometer with a  $S/N \simeq 4$ . The corresponding pressure is measured through a microphone placed close to the loudspeaker, at the same distance of the vibrating plate. We found that the lower signal that our system is sensitive to is around 0.5 Pa, 5 orders of magnitude lower than the traditional pressure values involved in a shock wave [48].

#### 3.2.2 Resonance frequencies of a screwed plate

We are measuring vibrations by means of a metallic lid, characterized by its resonances. Those resonances must be at frequencies different from the signal

we are interested to detect, given by the interlacing process.

This is the reason why we decided to further investigate the vibration modes of a plate, starting with the simple case of a cantilever beam. The theoretical and experimental dissertation on the cantilever beam vibration has been realized during a school on active vibration control (Technical University of Ostrava, prof. Tuma Jiří, [56]).

### **Simplified model: the cantilever beam**

The following pages contain a brief overview of the theory of vibrations to develop an analytical model (lumped-parameter model) that allows to predict the resonance frequencies of the beam.

The lumped-parameter model approximates the cantilever beam as a continuum: the system is idealized as rigid masses joined by massless springs and dampers. This means that we are assuming that the mass of the spring is negligible and its only effect is to exert a force between the mass and the support to which the spring is attached. A rigid mass does not deform and does not feel any elastic force.

This approach has been employed in the study of vibrations of a cantilever beam, aiming at an active control of vibrations [56]. Indeed, in order to control actively vibrations, the movement of the structure needs to be predicted in such a way that an actuator can be driven to counterbalance this movement. The control of vibrations is a hot topic in civil and seismic engineering, such as in the automotive and energetic field. For example, dampers of vibration are employed in overhead power lines to control wind-induced oscillations or in projecting high buildings. The largest tuned mass damper has been constructed on Taipei101, a 509 m tall skyscraper. In the past, many architectural disasters occurred due to a wrong planning of the vibrations control. One example is the collapse of Tacoma Narrows bridge in 1940.

For the analysis, the beam is divided into  $N$  discrete cuboid elements with the mass  $\Delta m$  and length  $\Delta L$ , connected by rotational springs with torsion stiffness  $K_\delta$ . Deflections in points of nodes are marked  $y_1 \dots y_N$ , as shown in Fig.3.4. The beam is clamped at the xy-plane and only planar motion in the yz-plane is assumed. The meeting points of the adjacent elementary beams are described by coordinates  $y_1, y_2, \dots, y_N$  and the angles of rotation with respect to the horizontal axis are  $\delta_1, \delta_2, \dots, \delta_N$ .

The beam is characterized by an area moment of inertia of cross-section  $I_x$  and a mass moment of inertia  $J_x$ , related to the beam geometry:



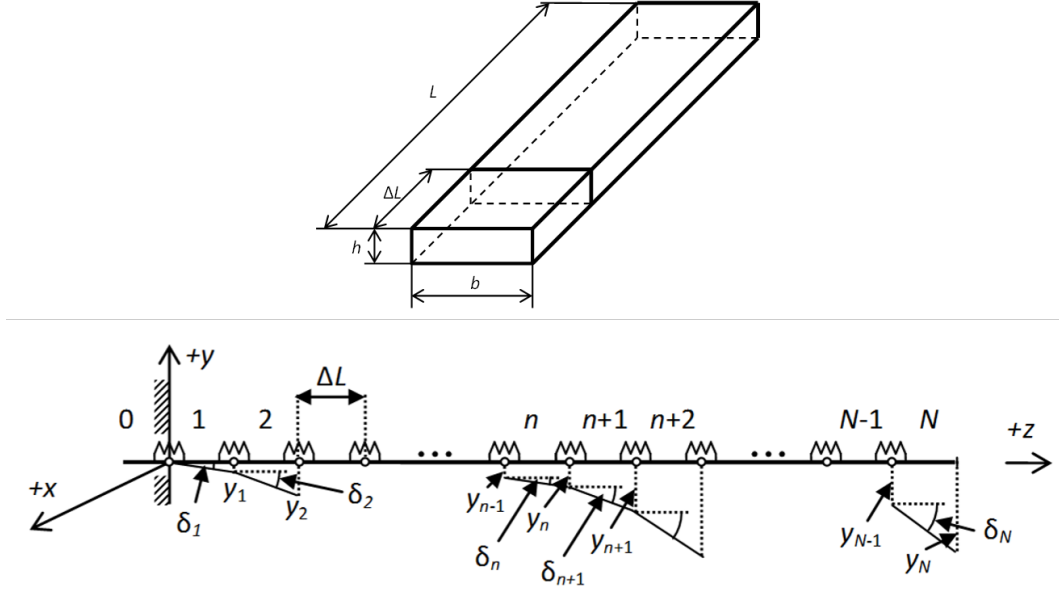


Figure 3.4: Lumped parametrization of the beam divided in  $N$  rigid masses joined by springs.

$$I_x = \frac{bh^3}{12} \quad (3.2) \quad J_x = \Delta m \frac{\Delta L^2 + h^2}{12} \quad (3.3)$$

To derive the potential energy of the system, the rotational stiffness  $K_\delta$  needs to be determined.  $K_\delta$  relates the applied moment  $M$  to the relative rotation  $\Delta\delta$ , where the moment is expressed as a force acting in the middle of a discretized cuboid:  $M = F\Delta L/2$  and, for small angles,  $\Delta\delta = \Delta y/\Delta L$  and hence:

$$K_\delta = \frac{M}{\Delta\delta} = \frac{F\Delta L^2}{2\Delta y} \quad (3.4)$$

The Euler-Bernoulli bending theory demonstrates that the curvature of the beam ( $1/r$  of Fig.3.5) is directly proportional to the bending moment  $M_B$  and inversely proportional to the flexural rigidity  $EI_x$  as:

$$\frac{1}{r} = \frac{M_B}{EI_x} = \frac{F\Delta L}{EI_x} = \frac{d^2y}{dz^2} \quad (3.5)$$

From simple geometrical considerations we obtain

$$\frac{d^2y}{dz^2} \simeq \frac{2\Delta y}{\Delta L^2} \quad (3.6)$$

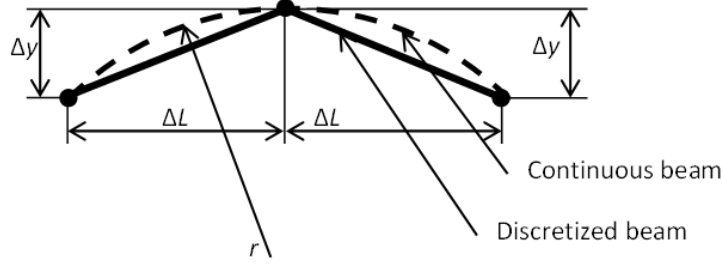


Figure 3.5: Key parameters in the segmentation of the beam.

and joining Eq.3.4 and Eq.3.5

$$K_\delta = \frac{EI_x}{\Delta L}. \quad (3.7)$$

At this point, we can easily derive the potential energy  $V$  of the system

$$V = \sum_{n=1}^{N-1} \frac{1}{2} K_\delta (\Delta \delta_n)^2 \quad (3.8)$$

and the kinetic energy  $T$

$$T = \sum_{n=1}^N \frac{1}{2} \Delta m \left( \frac{dY_n}{dt} \right)^2 + \sum_{n=1}^N \frac{1}{2} J_x \left( \frac{d\delta_n}{dt} \right)^2 \quad (3.9)$$

to obtain the Lagrangian  $L = T - V$ . The equation of motion in each point of the beam is given by

$$\frac{d}{dt} \left( \frac{\partial L}{\partial \dot{y}_n} \right) - \frac{\partial L}{\partial y_n} = 0 \quad (3.10)$$

That results in the following system of equations:

$$M\ddot{y}(t) + Ky(t) = 0 \quad (3.11)$$

with

$$M = \begin{bmatrix} B & A & 0 & \dots & \dots & \dots & 0 \\ A & B & A & 0 & \dots & \dots & 0 \\ 0 & A & B & A & 0 & \dots & 0 \\ 0 & 0 & \ddots & \ddots & \ddots & 0 & 0 \\ 0 & \dots & 0 & A & B & A & 0 \\ 0 & \dots & \dots & 0 & A & B & A \\ 0 & \dots & \dots & \dots & 0 & A & B/2 \end{bmatrix}$$

the mass matrix, where  $A = \Delta m/4 - J_x/\Delta L^2$ , and  $B = \Delta m/2 + 2J_x/\Delta L^2$

$$K = \frac{K_\delta}{\Delta L^2} \begin{bmatrix} 7 & -4 & 1 & 0 & \dots & \dots & 0 \\ -4 & 6 & -4 & 1 & 0 & \dots & 0 \\ 1 & -4 & 6 & -4 & 1 & \dots & 0 \\ 0 & \ddots & \ddots & \ddots & \ddots & \ddots & 0 \\ 0 & \dots & 1 & -4 & 6 & -4 & 1 \\ 0 & \dots & 0 & 1 & -4 & 5 & -2 \\ 0 & \dots & \dots & 0 & 1 & -2 & 1 \end{bmatrix}$$

the stiffness matrix.

Considering also damping, the resulting equation of motion is:

$$M\ddot{y}(t) + D\dot{y}(t) + Ky(t) = F(t) \quad (3.12)$$

Where, according to Rayleigh, the damping matrix is a linear combination of the mass and stiffness matrix

$$D = \alpha M + \beta K \quad (3.13)$$

Simulink was used to simulate the response of the system, to compare results obtained from the mathematical model with an experiment. The experiment (performed in the laboratories of the Faculty of Mechanical Engineering, Ostrava) consisted in exciting a steel cantilever beam (with  $L=50$  cm,  $b=4$  cm,  $h=0.5$  cm) with a white noise next to the fixed end of the beam and monitoring the induced vibration with an accelerometer mounted at the opposite end. Since the piezoactuator is mounted in point  $y_1$ , this point becomes another input to the model. For this reason, matrices and vectors need to be partitioned and a white noise disturbance is introduced in  $y_1$  as input of the simulation. Considering the ratio of the FFTs of the eigenvectors at the free end and at the clamped end of the beam, we obtain the simulated frequency response of the system (red), that can be easily compared to the experimental one (blue) in Fig.3.6.

The parameters of damping  $\alpha$  and  $\beta$  are optimized comparing the experimental results with the simulation. The good agreement between experimental data and simulations validates the model.

We aim to further develop the model towards a more realistic simulation of the plate screwed to the interlacer, using a FEM simulation. So, we compared the result of the analytical model with the simulation of the same object performed with the solid mechanics interface module of COMSOL Multiphysics®. The resonance frequencies simulated in this way are in agreement with the one obtained previously, confirming the validity also of the FEM simulation. This result was encouraging in enhancing the geometry of the simulation in order to make it similar to the real situation.

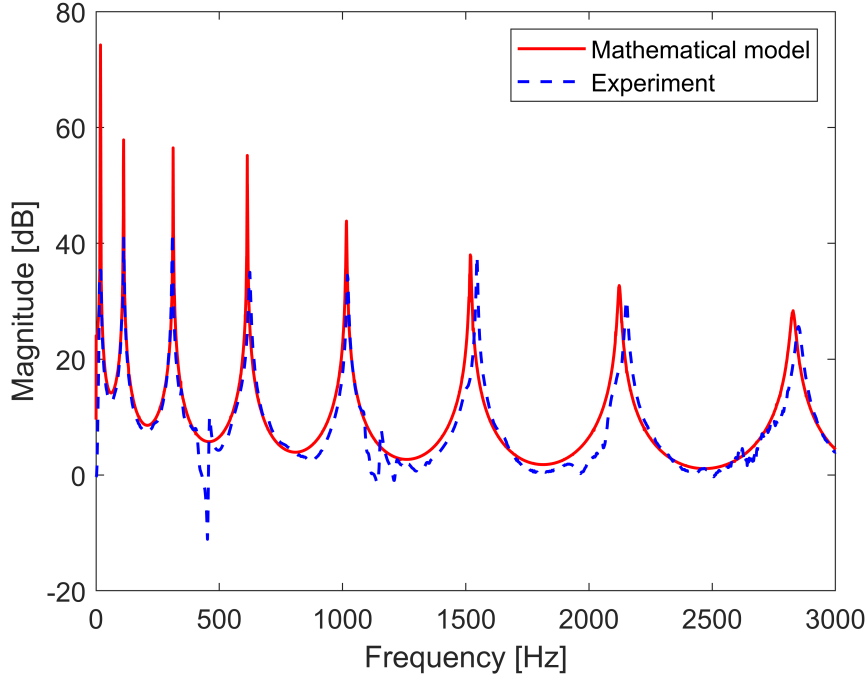


Figure 3.6: Comparison of simulated and measured frequency response functions of the cantilever beam.

#### Improved model: the screwed plate

Using again the solid mechanics interface of COMSOL, we considered a more realistic geometry of the system, where the plate is fixed to the interlacer by means of two screws. So, we simulated the response of an aluminum plate excited from below (the blue region of Fig.3.7 represents the excitation area) with a 4 bar solicitation. The screwing is simulated considering the internal surface of the cylindrical holes as fixed.

To evaluate the response of the plate in different blocking configurations, we evaluated the frequency spectra of a free plate, a plate screwed in two points and a plate screwed in four points.

Since we are interested in the resonance frequencies of the plate and not in the characterization of the full vibration dynamics, to reduce the computational time, we performed an Eigenfrequency study.

The red point in Fig.3.7 represents the position where the accelerometer is fixed and for this reason the vibrations have been studied in this point, using a finer and finer mesh until we did not observe any variation in the resonance frequency. The resulting frequency spectra are shown in Fig.3.8. The displacement values have been normalized to have just a relative information.

### 3.2. DESIGN OF THE EXPERIMENTAL SETUP

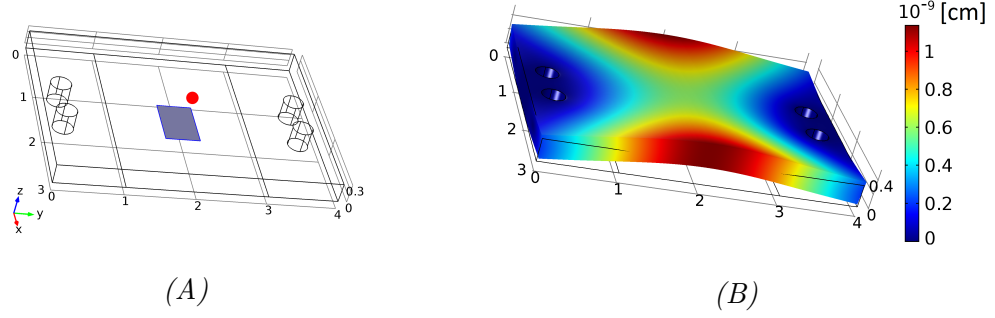


Figure 3.7: Geometry used for the FEM simulation, aluminum plate 3 mm thick, 30 mm wide and 40 mm long. The blue area represents the solicitation region, the red point is the accelerometer position (A). Result of the simulation, showing the displacement of each point of the plate after solicitation (B).

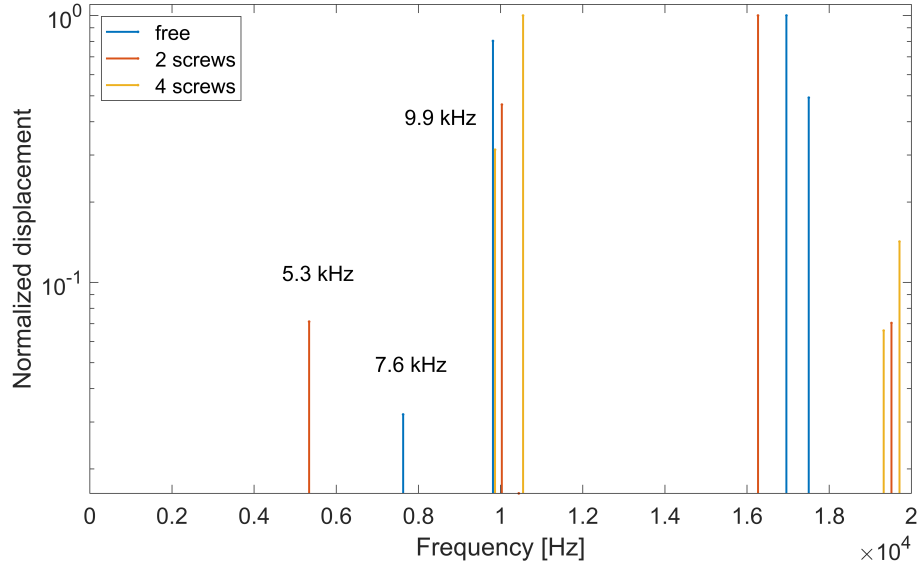


Figure 3.8: Eigenfrequency study of the vibrating plate of Fig.3.7, free to vibrate, fixed in two points and fixed in four positions.

The frequency spectra indicate that the resonances of the system are strongly dependent on the blocking conditions.

In any case, we observe that the first resonance occurs between 5 kHz and 10 kHz and not in the frequency range of interest for interlacing (between 400 Hz and 900 Hz), as desired.

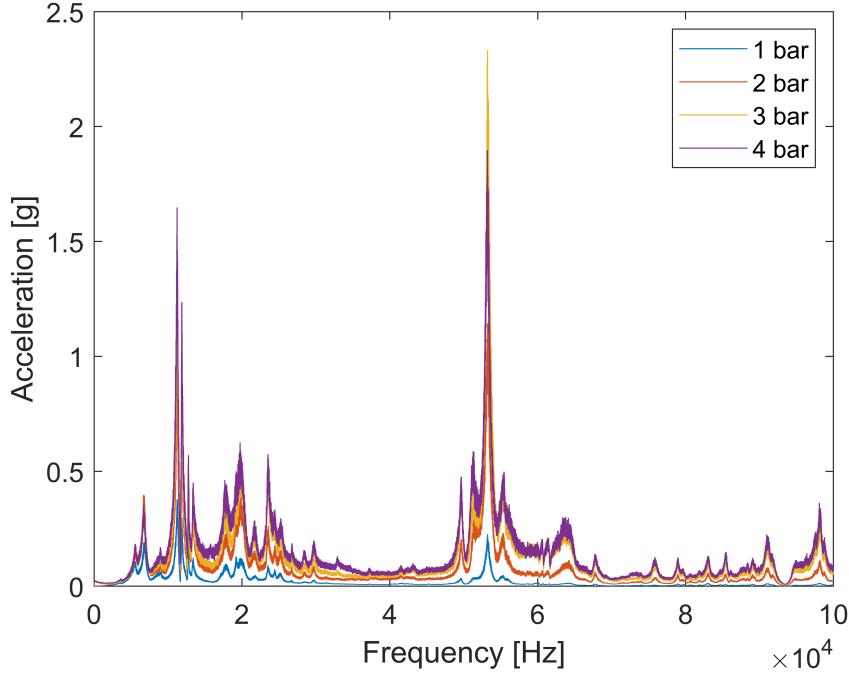


Figure 3.9: Frequency spectra of the vibrating plate, for increasing inlet pressure values.

### Experimental results

To compare this result with the experimental measurement, we stud mounted the accelerometer (PCB M352C67) on the aluminum plate in front of the air jet nozzle and acquired the vibrations as shown in Fig.3.3. This type of mounting ensures a close coupling between the block and the sensor, allowing for good transmission of the vibrations to be measured [57].

We considered four different pressure values (3, 3.5, 4 and 5 bar) and we measured the vibrations induced by air, analyzing data as described in Sec.3.2. The resulting spectra are shown in Fig.3.9.

The first detected resonance frequency is around 6 kHz, in the frequency range predicted by the simulation. As already discussed previously, different fixing constraints cause different resonances, difficult to predict exactly due to the low torque control on the screwing system. Additionally, the simulation does not consider the vibrations caused by the entire system interlacer+aluminum plate+accelerometer. For this reason, the exact frequency response is not predicted by the simulation, since it depends on the true blocking conditions and on resonant systems not considered.

The experimental result confirms the absence of resonances in the frequency

range of interest for our process, indicating that the geometry chosen could be suitable to monitor the vibrations induced by interlacing.

In any case, both the simulation and the measured spectra show the occurrence of high frequency vibrations, that exceed the flat frequency band of the accelerometer.

### 3.2.3 Mechanical filters

#### Accelerometer saturation

As reported also in [58], if the mechanical solicitation exceeds the transducer bandwidth interfering with the accelerometer resonance peak, a saturation of the transducer may happen. This could alter the measurement and the response of the sensor. For this reason, we aimed at testing the hypothetical saturation of the sensor due to high frequency solicitations.

We measured the lower limit of detection of the screwed accelerometer increasing the intensity of the solicitation that induces the high frequency components (hence increasing pressure).

The measurement has been performed coupling the interlacer with a plate that vibrates at a settable frequency and intensity. Through this plate, we set in vibration the interlacer and identified the minimum detectable solicitation ( $S/N = 4$ ) for the different inlet pressures. At this point, switching on the inlet pressure, we measured the minimum detectable acceleration. The results for three different frequencies are shown in Fig.3.10.

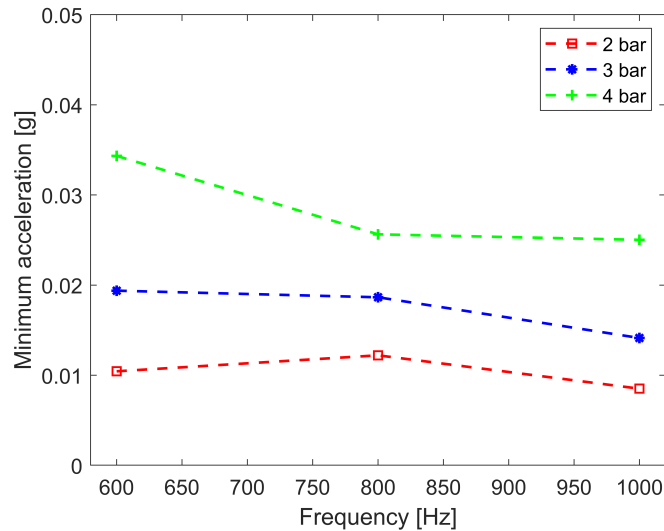


Figure 3.10: Minimum detectable vibration varying inlet pressure, for different solicitation frequencies.

The minimum detectable acceleration increases with air pressure: we observe a doubling of the signal at 3 bar with respect to that at 2 bar and a tripling of the value at 4 bar. This result indicates a possible saturation of the sensor due to high frequency contributions, that could prevent us from detecting the low frequency components of our interest.

The common way to avoid this kind of saturation is to employ mechanical filters, damping in this way undesired spectral contributions [58]. To ensure linear response we want to limit the spectrum of the acceleration input within the transducer recommended bandwidth. Generally, the maximum usable bandwidth needs to be less than one fifth of the accelerometer resonance, as reported in various studies about high shock measurements. It is worth to underline that we are interested in limiting the mechanical excitation frequency range; that's why an electrical filter at the sensor output is not sufficient, since it cannot prevent mechanical overload effects [59].

### **Free vibration of a viscously damped system**

What is a mechanical filter and why does it damp vibrations exceeding a cutoff frequency? What does this frequency depend on? To answer these questions we go back to the theory of vibrations and in particular we need to understand which are the key elements in a vibrating system.

The fundamental components in a vibrating mechanical system are inertia, stiffness, damping and a source of work or energy. The inertia element is anything that has a mass or stores kinetic energy. The stiffness element is a store of potential energy and can be modeled as a combination of springs, replaced by a single spring of an equivalent stiffness  $k_{eq}$ . The viscous damping component dissipates energy, the friction force is proportional to velocity and also in this case the overall viscous damping coefficient  $c_{eq}$  is calculated as a combination of viscous dampers. The source of energy could be either an initial energy present in the system or an external force [60]. Accordingly, the resulting free body diagram of a damped vibrating system subjected to a force  $f(t)$  is shown in Fig.3.11.

If the system is subjected to a sinusoidal excitation, the resulting equation of motion is

$$m_{eq}\ddot{x} + c_{eq}\dot{x} + k_{eq}x = f_0 \sin(\omega t) \quad (3.14)$$

The solution of Eq.3.14 is composed of two parts:

$$x(t) = x_h(t) + x_p(t) \quad (3.15)$$

with  $x_h(t)$  the homogeneous solution satisfying

$$m_{eq}\ddot{x}_h + c_{eq}\dot{x}_h + k_{eq}x_h = 0 \quad (3.16)$$



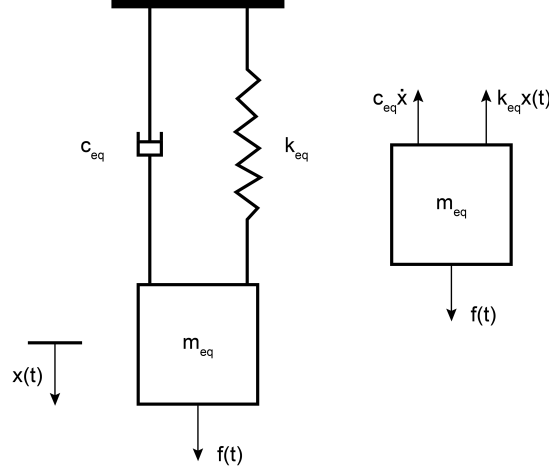


Figure 3.11: Model of vibrating object as a spring-mass-damper subjected to external excitation.

and  $x_p(t)$  the particular solution fulfilling

$$m_{eq}\ddot{x}_p + c_{eq}\dot{x}_p + k_{eq}x_p = f_0 \sin(\omega t) \quad (3.17)$$

for the sake of simplicity and to have just an idea of the key parameters and behavior of the system, we will just look deeper at the way of solving the homogeneous equation, that corresponds to the solution of the equation of motion of a free vibrating damped system. After that, we will just analyze the final solution of Eq.3.14.

Assuming that the solution of Eq.3.16 is of type

$$x_h(t) = De^{st} \quad (3.18)$$

then, substituting Eq.3.18 into Eq.3.16

$$(m_{eq}s^2 + c_{eq}s + k_{eq})De^{st} = 0 \quad (3.19)$$

and hence, to be true for all times  $t$

$$m_{eq}s^2 + c_{eq}s + k_{eq} = 0 \quad (3.20)$$

whose solutions are given by

$$s_{1,2} = \frac{-c_{eq} \pm \sqrt{c_{eq}^2 - 4k_{eq}m_{eq}}}{2m_{eq}} \quad (3.21)$$

We observe that  $c_{eq}^2 - 4k_{eq}m_{eq}$  is a critical parameter. If it is negative, roots are complex conjugates, while if it is positive or equal to zero, roots are real numbers. For this reason, we can define a critical damping as

$$c_c = 2\sqrt{k_{eq}m_{eq}} = 2m_{eq}\omega_n \quad (3.22)$$

with  $\omega_n = \sqrt{k_{eq}/m_{eq}}$ , the natural frequency of vibration of the system. Defining the damping ratio  $\xi$  as

$$\xi = \frac{c_{eq}}{c_c} \quad (3.23)$$

we can rewrite Eq.3.21

$$s_{1,2} = -\frac{c_{eq}}{2m_{eq}} \pm \sqrt{\left(\frac{c_{eq}}{2m_{eq}}\right)^2 - \frac{k_{eq}}{m_{eq}}} \quad (3.24)$$

considering that

$$\frac{c_{eq}}{2m_{eq}} = \frac{c_{eq}}{c_c} \frac{c_c}{2m_{eq}} = \xi\omega_n \quad (3.25)$$

we obtain

$$s_{1,2} = -\xi\omega_n \pm \sqrt{\xi^2\omega_n^2 - \omega_n^2} = -\xi\omega_n \pm \omega_n\sqrt{\xi^2 - 1} \quad (3.26)$$

This rewriting of Eq.3.21 allows to point out three subsets of solutions according to the value of the damping ratio  $\xi$ .

1. *Underdamped* ( $0 < \xi < 1$ ); the solutions are complex conjugates,

$$s_{1,2} = -\xi\omega_n \pm i\omega_n\sqrt{1 - \xi^2} = -\xi\omega_n \pm i\omega_d \quad (3.27)$$

having defined

$$\omega_d = \omega_n\sqrt{1 - \xi^2} \quad (3.28)$$

In this way, the general solution is given by

$$x(t) = D_1e^{s_1t} + D_2e^{s_2t} = e^{-\xi\omega_nt} (D_1e^{i\omega_dt} + D_2e^{-i\omega_dt}) \quad (3.29)$$

or, analogously,

$$x(t) = e^{-\xi\omega_nt} (A_1 \cos \omega_d t + B_1 \sin \omega_d t) \quad (3.30)$$

where  $A_1$  and  $B_1$  are easily determined through the initial conditions. Eq.3.30 indicates that the amplitude is exponentially decaying and that the natural frequency of the damped system is  $\omega_d$ , smaller than in the undamped case ( $\omega_n$ ).

2. *Critically damped* ( $\xi = 1$ ); the solutions are real equal negative numbers:

$$s_1 = s_2 = -\omega_n \quad (3.31)$$

and the general solution is

$$x(t) = A_1 e^{-\omega_n t} + B_1 t e^{-\omega_n t} \quad (3.32)$$

Hence, the solution is not oscillatory.

3. *Overdamped* ( $\xi > 1$ ); the solutions are negative real numbers

$$s_{1,2} = -\xi\omega_n \pm \omega_n \sqrt{\xi^2 - 1} < 0 \quad (3.33)$$

Also in this case, the solution is not oscillatory.

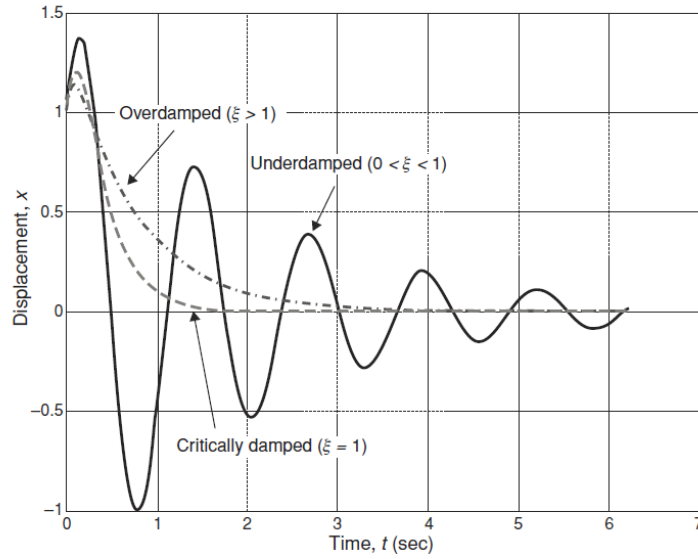


Figure 3.12: Solutions of a free vibrating damped system (from [61]).

A comparison of the three solutions is shown in Fig.3.12, where we observe that the rate of decay of a critically damped system is higher than the overdamped one, since

$$|s_{2,over\_damp}| = |-\xi\omega_n - \omega_n \sqrt{\xi^2 - 1}| > \omega_n = s_{cr\_damp} \quad (3.34)$$

So, considering this simplified model, we have learned that the damping ratio  $\xi$  is the key parameter that determines if a system oscillates, or if it is just exponentially damped at a certain rate, as well as the frequency of oscillation.

### Response of a damped system to a harmonic excitation

To derive the frequency response of the system of Fig.3.11, we need to consider the external harmonic solicitation, assuming a solution of the particular equation of the type

$$x_p(t) = A \sin(\omega t - \phi) \quad (3.35)$$

substituting in Eq.3.17, we can easily obtain that

$$\frac{A}{f_0/k_{eq}} = \frac{1}{\sqrt{(1-r^2)^2 + (2\xi r)^2}} \quad (3.36)$$

with  $r = \omega/\omega_n$ , the ratio of the excitation to the natural frequency. The solutions of the homogeneous equation in all three cases (underdamped, critically damped and overdamped) tend to zero increasing time. Therefore, the homogeneous part is also called transient response, while the particular solution with amplitude described by Eq.3.36 represents the steady state response, plotted in Fig. 3.13.

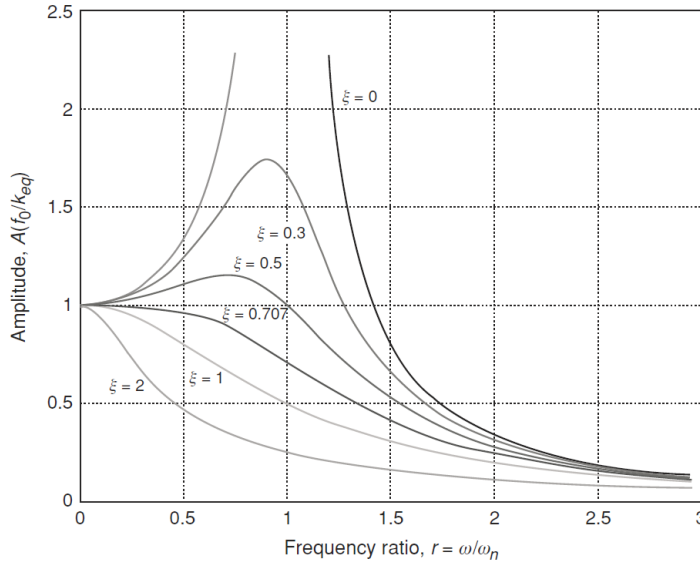


Figure 3.13: Amplitude as a function of the frequency ratio  $r$ , varying the damping ratio  $\xi$  (from [61]).

We observe that the response of the system depends both on the damping ratio and on the exciting frequency. Near resonance the amplitude increases, especially for lower values of damping.

It is also interesting to evaluate the behavior of the bandwidth varying the damping ratio, where the bandwidth frequency (or cutoff frequency) is ob-

tained fixing

$$\frac{A}{f_0/k_{eq}} = \frac{1}{\sqrt{(1-r_b^2)^2 + (2\xi r_b)^2}} = \frac{1}{\sqrt{2}} \quad (3.37)$$

that leads to

$$r_b = \frac{\omega_b}{\omega_n} = \sqrt{1 - 2\xi^2 + \sqrt{4\xi^4 - 4\xi^2 + 2}} \quad (3.38)$$

This result can be more easily understood plotting the bandwidth as a function of the damping ratio.

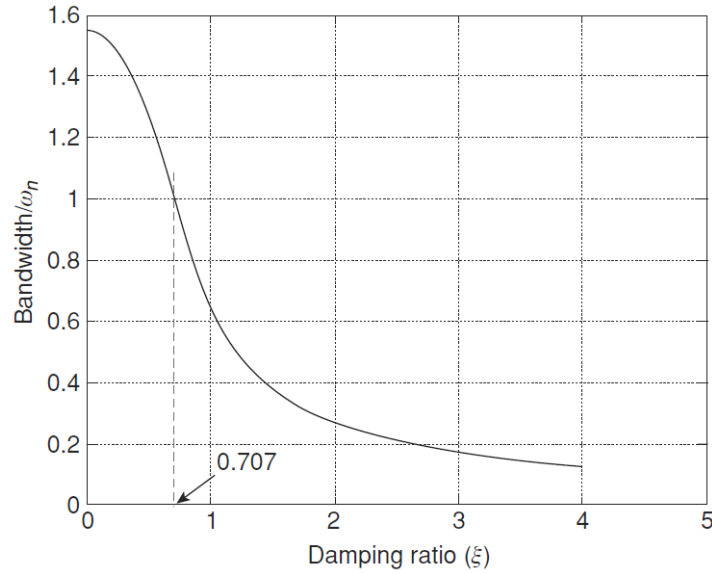


Figure 3.14: Bandwidth of a damped vibrating system as a function of the damping ratio (from [61]).

In Fig.3.14 we observe that increasing damping the bandwidth decreases. Moreover, when the damping ratio equals  $\xi = 0.707$ , the bandwidth equals the natural frequency of the system.

To sum up, we have found that a vibrating mechanical system damps the oscillations above a certain frequency, depending on the value of the damping ratio of the material.

### Experimental results

Drawing inspiration from the theory described above, we decided to place a damping material between the accelerometer and the vibrating plate. We chose to use washers of different damping materials, such as silicone or plastic, verifying primarily their mechanical low pass frequency properties. Therefore, we compared the frequency spectra of the vibrations induced on the aluminum

plate stressed by an air jet with an incoming pressure of 3 bar, fixing the accelerometer in three different ways: screwed on the plate, screwed with a silicone washer and screwed with a plastic washer. The resulting spectra are shown in Fig.3.15.

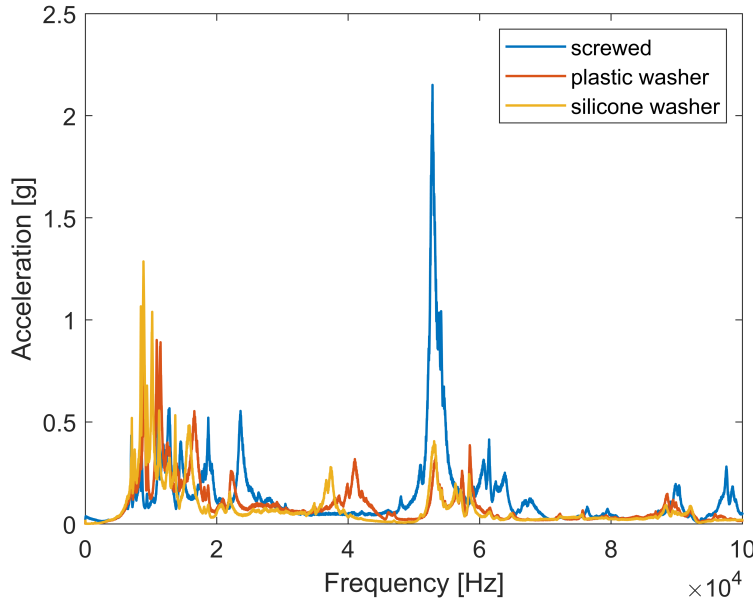


Figure 3.15: Comparison of vibration spectra mounting the accelerometer in three different ways.

We observe that the employment of the damping material causes a shift in frequency of the spectrum and a reduction of the high frequency components. In particular, the dominant high frequency component around 52 kHz that could cause an excitation of the resonance of the accelerometer and hence an alteration of its response, is significantly reduced (5 times).

Looking at the low frequency contributions of Fig.3.16 (A), we observe the occurrence of two vibrations around 1 kHz and 1.4 kHz, that are detectable just for low pressure values. Increasing pressure and hence the intensity of the mechanical solicitation, the two contributions are not detectable anymore.

Using the two washers as damping materials, we observe again the occurrence of the low frequency components even increasing the inlet air pressure, as shown in Fig.3.16 (B, C).

In order to have a further confirmation of this result, we coupled the interlacing block with a plate vibrating at a known frequency (500 Hz in this case) and amplitude and we compared the signals obtained with the three mounting configurations, increasing air pressure.

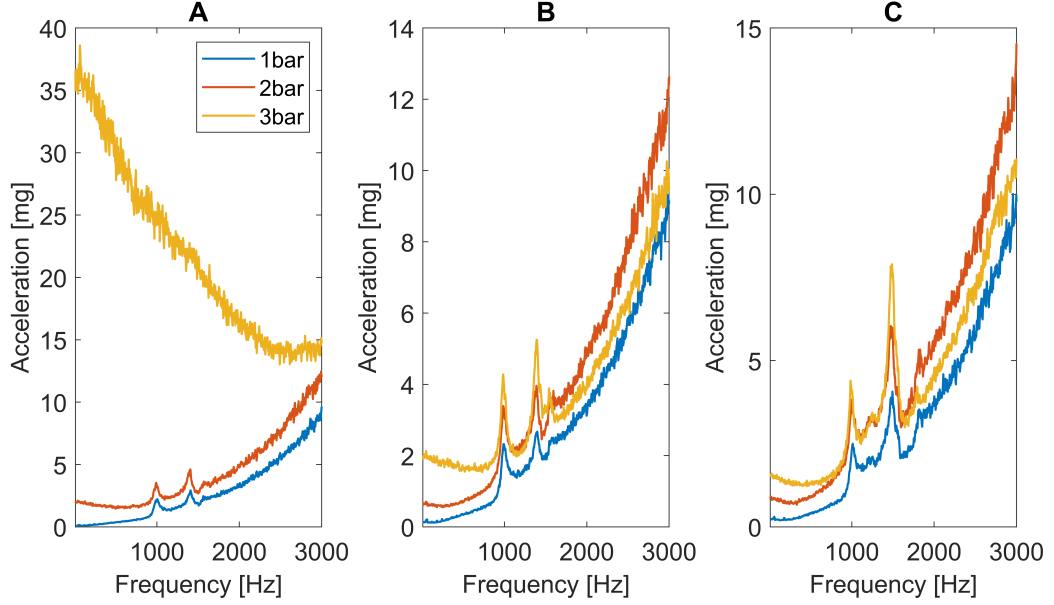


Figure 3.16: Comparison of low frequency spectra for three ways of mounting the accelerometer with different inlet pressure values. Accelerometer screwed on the vibrating plate (A), accelerometer screwed using a silicone washer (B), accelerometer screwed using a plastic washer (C).

In Fig.3.17 is reported the ratio of the vibration amplitude for different inlet air pressure, divided by the amplitude of the vibration without the impinging air jet.

It is very interesting to observe that the induced vibration is damped increasing air pressure when the accelerometer is screwed, while the amplitude remains constant and equal to the one measured without impinging air, when the plastic and silicone washers have been employed.

These results were encouraging in employing the damping material for the detection of the possible vibrations induced by the interlacing process.

### 3.3 Vibrations induced by the interlacing yarn

We performed the measurement with the same parameters and experimental setup described in the previous section. We considered five different pressure values (3, 3.5, 4, 4.5 and 5 bar) and we repeated the measurements with and without the yarn running in the channel of the interlacer, screwing the accelerometer with the silicone washer. The comparison of the resulting spectra is reported in Fig.3.18. The spectra were analyzed just up to 20 kHz, since the higher frequency components are reduced by the mechanical filter.

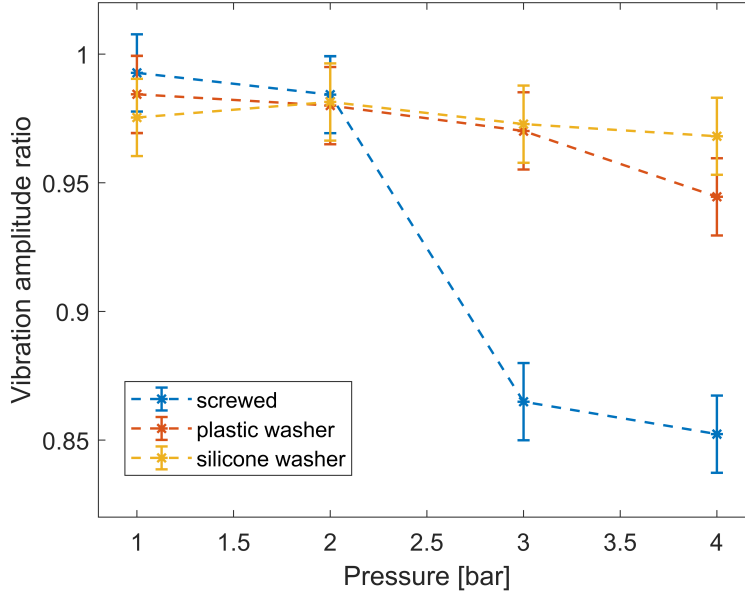


Figure 3.17: Ratio of vibration amplitude measured with an impinging air jet, divided by the amplitude without air as a function of inlet pressure, considering the three accelerometer mounting configurations.

We observe a higher intensity of vibrations with the interlacing yarn in the channel up to 12 kHz. Moreover, the signal increases with pressure, as expected due to the higher solicitation. The frequency components are the same with and without the yarn, except for one contribution around 3 kHz.

We do not observe any low frequency component in the range between 400 Hz and 600 Hz, corresponding to the interlacing frequency measured with the high speed camera in the same working conditions. This indicates that if there is a modulation of the shock waves or of the flow, it does not occur at the frequency of interlacing.

However, we observed a new frequency component with the yarn (around 3 kHz), probably due to the fact that the filaments hit the aluminum plate. The filaments could interact with the twin vortices, rotate and hit periodically the plate. If this component is related to the spinning frequency of the twin eddies in the interlacer, we expect that it increases in frequency with pressure. Indeed, an increase in the eddies vorticity with pressure is predicted also by the FEM simulation of the flow motion into the interlacer, shown in Fig.3.1. This result is observed overlapping the spectra at different pressure values, in the bottom-right box of Fig.3.18. In order to find the central frequency of the peak in the spectrum, we subtracted the baseline and fit the component with



### 3.3. VIBRATIONS INDUCED BY THE INTERLACING YARN

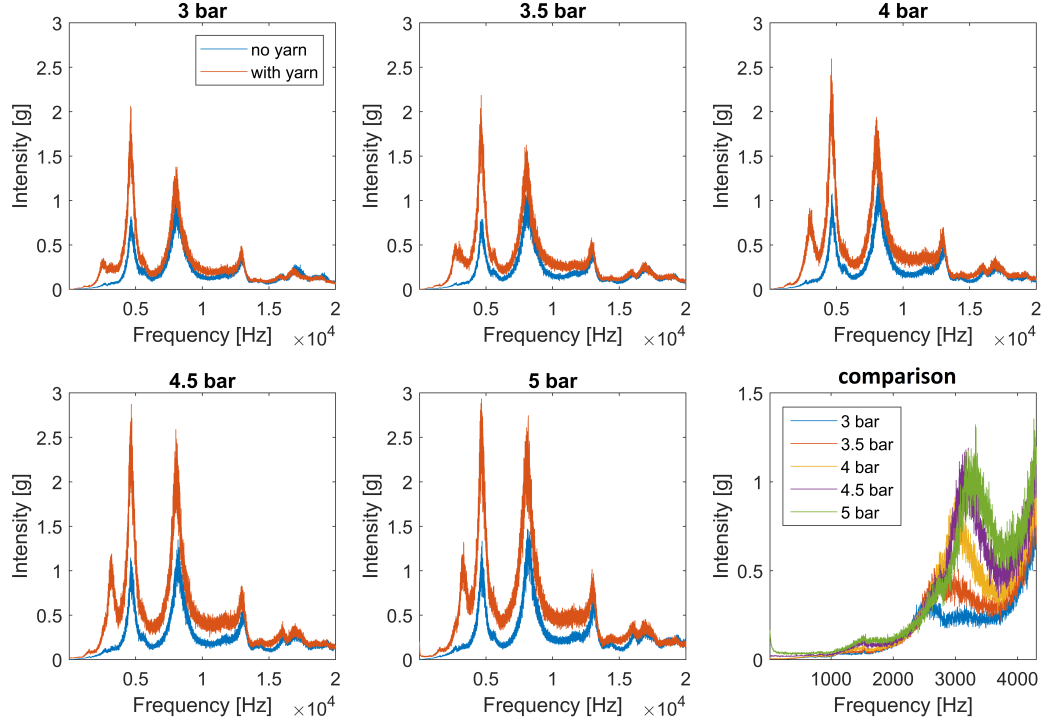


Figure 3.18: Vibration spectra varying the inlet pressure of compressed air, comparing the spectra obtained only with compressed air (blue) and with the interlacing yarn (red). In the last box: comparison of the signal with the yarn at low pressure values, to zoom the 3 kHz component.

a Gaussian (Fig.3.20, A). In Fig.3.20 (B) we observe an increase of the central frequency with pressure, as expected. This result confirms the hypothesis that the yarn, set in motion by the vortexes, is inducing the observed vibration. The 3 kHz component is not likely a resonance of the aluminum plate, since we observe that it is shifting with pressure, while the other resonance frequencies remain fixed for different pressure values, as shown in Fig.3.19.

Up to now, we monitored the vibrations induced by a free moving interlacing yarn. The measurements were performed in the laboratory, on a pilot testing setup. During these first measurements, the yarn was not guided, but just set in motion by compressed air. To work also in more controlled conditions, we repeated the measurements on the industrial machine, the yarn tension is fixed (70 cN) and the speed is varied through two guiding rolls, one before and one after the interlacer, that ensure an higher stability of yarn motion. We compared the vibrations induced varying the yarn speed, with an inlet pressure of 6.5 bar; the resulting spectra are reported in Fig.3.21. We do not observe any new frequency component with the yarn running in the channel, but just an

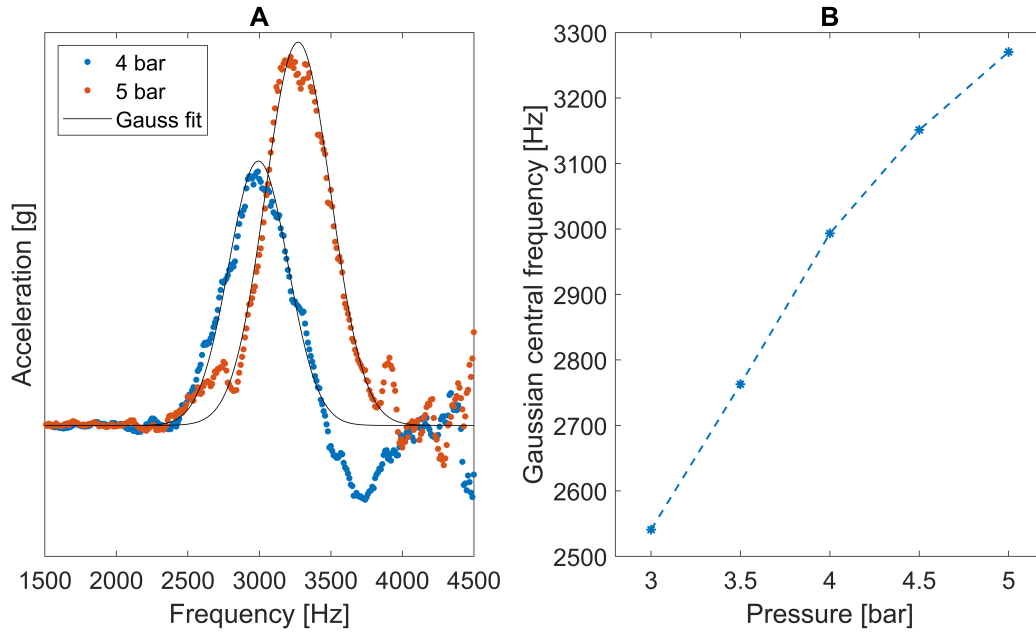


Figure 3.19: Examples of baseline subtraction and Gaussian fit for two pressure values (A). Central frequency of the Gaussian distribution as a function of the inlet pressure (B).

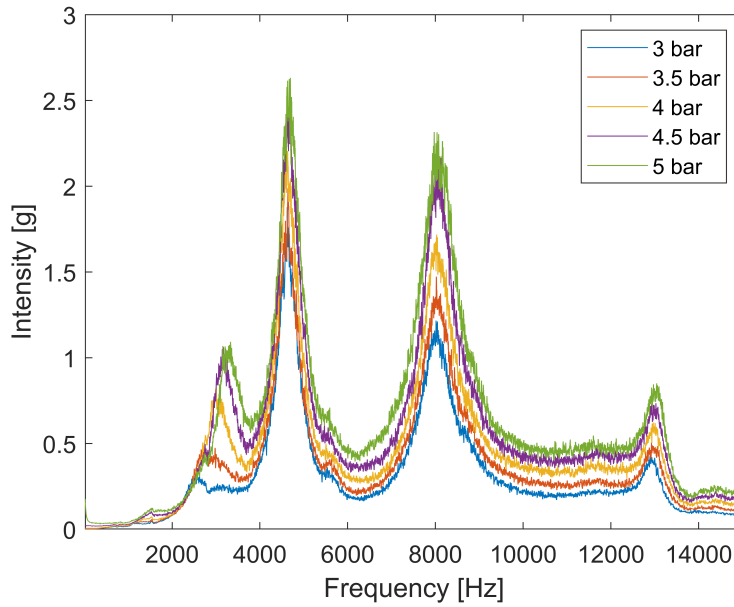


Figure 3.20: Frequency spectra for increasing inlet pressure values in the whole frequency range.

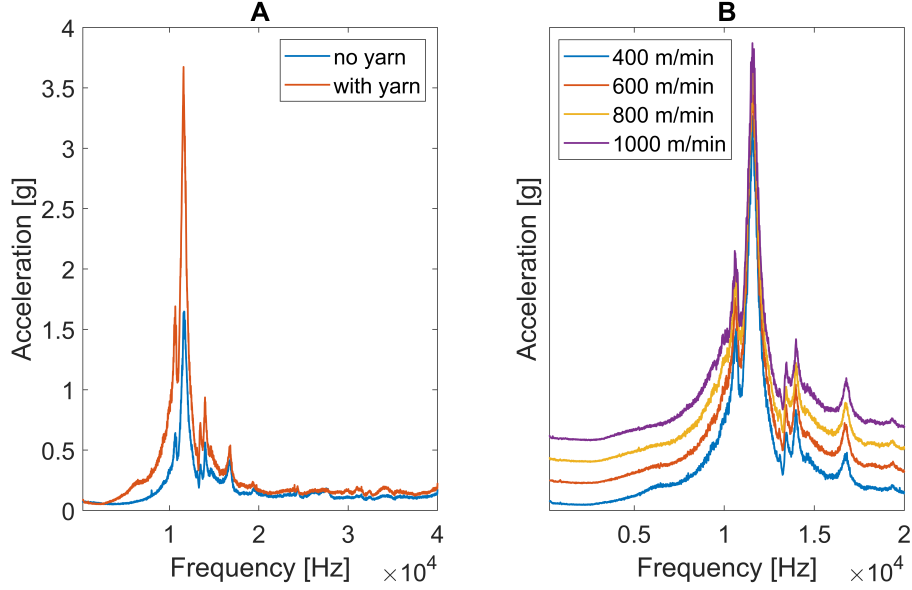


Figure 3.21: Overlap of the spectra with (red) and without (blue) the yarn, yarn speed of 400 m/min and air pressure of 6.5 bar (A). Vibration measured with the yarn running at growing yarn speed values with a shift of 0.2 g for a better comparison (B).

increase of the signal intensity due to the additional vibrations caused by the yarn motion (Fig.3.21, A). We do not observe the component previously detected around 3 kHz and we hypothesize that this fact is caused by the higher guiding of the yarn. As a result, the yarn motion is more restrained and it cannot hit freely the aluminum plate as in the previous case; in this way, the vibration is prevented. Additionally, the spectra show the same components also increasing the yarn speed, while if a vibration would be related to the interlacing process, it should increase with the speed (Fig.3.21, B).

### 3.4 Chapter conclusions

An analysis of the vibrations induced by the interlacing process has been performed. The experimental setup has been optimized in order to avoid system resonances in the frequency range of interlacing. Additionally, we studied the improvements caused by the employment of mechanical filters in the measurement. The frequency spectrum acquired with this optimized setup, does not show any component in the range interested by interlacing. However, when the yarn is not guided and free to move, a 3 kHz contribution is observed, just with the yarn. This components shifts towards higher frequency values increasing

the inlet pressure, indicating that it could be caused by the interaction of the yarn with the air vortexes. Indeed, the vortexes spinning frequency increases with pressure. This component has been detected just when the yarn is free to move and hit the vibrating plate, while when its motion is more constrained and guided, the vibration is not stimulated anymore.

Since our system sensitivity is high enough to detect shock waves modulations, we can state that the interlacing process does not cause such a modulation at the knots frequency. Additionally, with the analyzed mechanical system, we did not detect even a flow modulation in the interlacing frequency range. For this reason, the proposed vibration analysis is not suitable to monitor on-line the interlacing process.

# 4

## Acoustic analysis of an interlaced yarn

### Contents

---

<b>4.1</b>	<b>Feasibility study . . . . .</b>	<b>64</b>
4.1.1	Yarn diameter modulation during production . . . . .	64
4.1.2	Simulation of air pressure close to the yarn . . . . .	65
<b>4.2</b>	<b>Theoretical background . . . . .</b>	<b>68</b>
4.2.1	Wave equation, speed of sound and sound pressure level . . .	68
4.2.2	The acoustic impedance . . . . .	70
4.2.3	Acoustic filters . . . . .	71
<b>4.3</b>	<b>Experimental measurements . . . . .</b>	<b>74</b>
4.3.1	Experimental setup . . . . .	74
4.3.2	Acoustic filter design . . . . .	74
4.3.3	Sensing of the interlaced yarn . . . . .	77
4.3.4	Improvement of yarn signal over external noise . . . . .	82
<b>4.4</b>	<b>Chapter conclusions . . . . .</b>	<b>87</b>

---

**Overview** A free running circular saw emits a noise at the frequency of its teeth. In the same way, we aim to detect a pressure modulation close to the yarn, at the interlacing frequency. First, we will investigate the feasibility of this idea, supported also by a simulation of our system. The results of the simulation will be compared and supported by experimental measurements. Then, some tricks to improve the microphone sensitivity in the frequency range of interest will be discussed, with an insight into the theory and design of acoustic filters. A differential and a correlation based method to reduce the noise will be compared and discussed.

## 4.1 Feasibility study

The vibration analysis described in the previous chapter indicated that the region close to the interlacer is affected by noise and vibrations. For this reason, we decided to focus our attention on the analysis of the interlacing process from another position, further from the interlacer and before the yarn collection into reels. In that place the yarn is guided and the tension is of about 70 cN. We asked ourselves if the modulation of the yarn is still detectable in those working conditions and if the yarn is stable enough, or in other words, if the yarn is oscillating, which is the amplitude of this oscillation.

If the modulation is still detectable, we are interested in monitoring it in two different ways, with an optical and an acoustic approach. Optically, we aim at looking at the shadow of the yarn by means of a photodiode, in this way we should be able to reconstruct the yarn profile. This approach will be described in the following chapter. The other idea is to monitor the pressure modulation provoked by a periodically shaped object moving in free air. Before going into deeper details of these two techniques, we first need to verify that the yarn is stable in the position chosen for the measurement and that the knots-open segments succession is detectable.

### 4.1.1 Yarn diameter modulation during production

The most straightforward way to evaluate and answer these questions is to observe the yarn motion by means of the high speed camera. In addition, to judge also the feasibility of the photodiode approach, we back-illuminated the yarn to monitor its shadow by means of the camera; the measurements were repeated varying the yarn speed. The frames were processed (as described in Section 2.1.2) to reconstruct the yarn section over time and we observed a diameter variation at the frequency of interlacing. This result indicates that the yarn modulation is detectable in the machine-working conditions, on-line,



Figure 4.1: Processed frame of a 7000 fps video of the yarn moving at a speed of 400 m/min. The yarn dimension both in the interlaced and open regions are indicated in red. An overall 3.5 mm oscillation amplitude is measured.

as the yarn is produced.

In Fig.4.1 is shown one frame of the video, to have an idea of the dimensions that we are dealing with and of the extent of the profile modulation.

In the exemplifying case of the reported frame, the yarn oscillation reaches a maximum amplitude of about 3.5 mm. The yarn diameter shows a modulation from 0.6 mm in presence of a knot, to 1.4 mm in correspondence to an open segment.

As already mentioned previously, we thought about a microphone-based knots sensing technique since we are aiming at detecting a pressure modulation caused by the motion of a periodically shaped object in air. This idea has been inspired thinking of the noise emitted by a free running circular saw, that has a predominant frequency of the same order as the frequency of the teeth passing a fixed point [62]. In the same way, we are interested in studying the motion of air around the moving yarn. In particular, we were asking ourselves if the yarn modulation observed in Fig.4.1 is sharp enough to provoke a detectable pressure change. As a first attempt to answer that question, we performed a 2D-FEM simulation, using COMSOL Multiphysics®, CFD module in the laminar flow approximation.

#### 4.1.2 Simulation of air pressure close to the yarn

In order to simulate this phenomenon, we simplified the yarn into a rigid object with the same geometry as the one shown in Fig.4.1. For the sake of simplicity, in the simulation we decided to choose the frame of reference of the yarn. In this way, instead of considering a moving object, we could keep the yarn fixed, with the air flow impinging on it. In Fig.4.2 is reported the pressure pattern around the yarn.

In our reference frame, the yarn is moving from left to right. As a result, in its frame of reference, the air flow is moving from right to left. We observe that as the air flow bumps into a transition knot-opening part, locally pressure

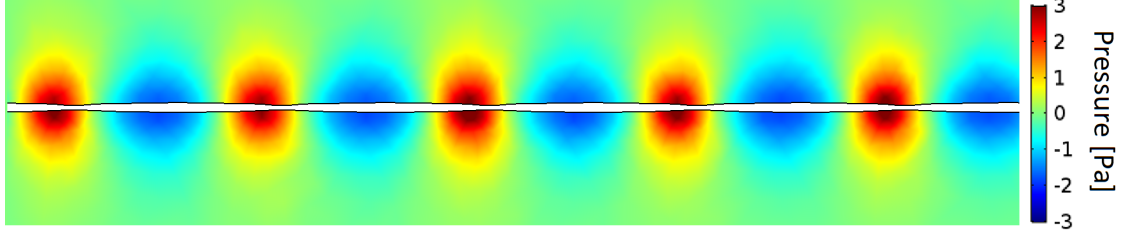


Figure 4.2: FEM simulation of an air jet impinging on the yarn (white). Pressure pattern considering an air speed of 1000 m/min.

increases, followed by a corresponding subsequent low pressure area. The pressure modulation is detectable just next to the yarn, while it is damped moving away from it. In the particular case of Fig.4.2, when the air flow is moving with a speed of 1000 m/min, the modulation is damped, with a 3 dB pressure reduction about 3 mm away from the yarn. Hence, if we imagine to place a sensor close to the yarn (about 1 mm from it), moving at the air flow speed, we are reproducing the configuration of a fixed microphone with a running yarn. The resulting pressure that the microphone should sense over time, according to the simulation, is reported in Fig.4.3 increasing the yarn speed.

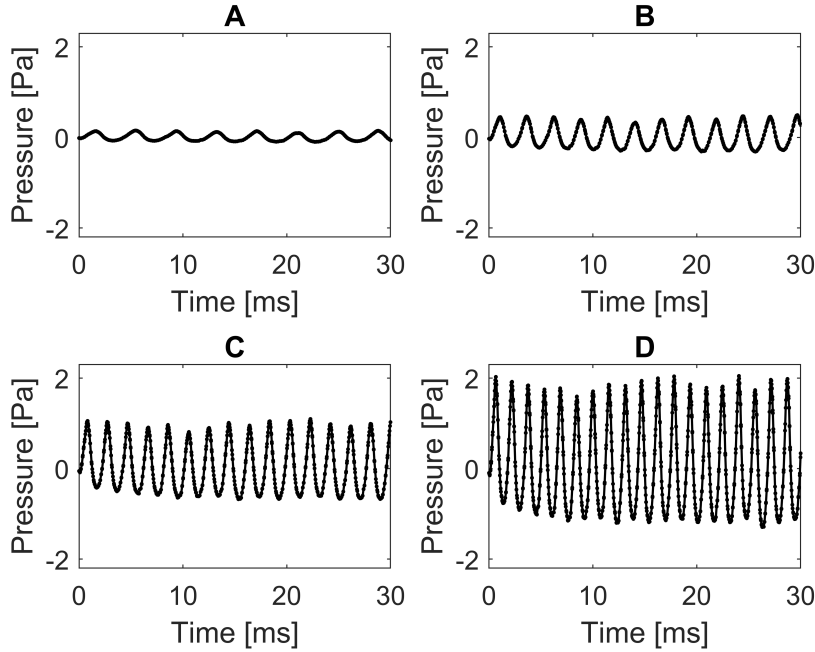


Figure 4.3: Simulation of the pressure variation over time increasing the air flow speed: 400 m/min (A), 600 m/min (B), 800 m/min (C), 1000 m/min (D).



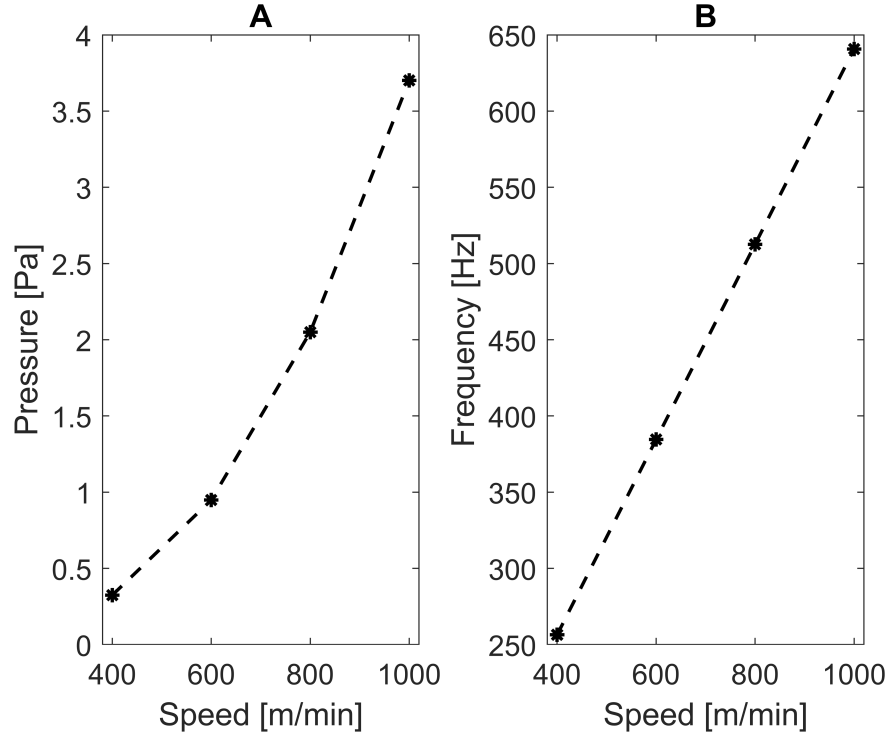


Figure 4.4: Amplitude (A) and frequency (B) of pressure modulation as a function of the air speed.

As expected, pressure is modulated over time and the frequency and amplitude of that modulation increase with the speed, as shown in Fig.4.4.

The results of the simulations are encouraging for the employment of a microphone to monitor the distance between knots over time, since the pressure values involved can be easily detected by microphones of the size of interest (some millimeters). The lower limit of detection of a microphone is given by thermal noise, shot noise and Johnson noise, but also by the thermal agitation of air molecules around the microphone, that generate an output signal even in absolutely quiet conditions. Taking for example a 22.4 mV/Pa microphone (EK3033, Knowles Electronics, Chicago, IL, USA), with a dimension of the order of few millimeters, its input noise level is of 26 dB SPL, corresponding to about 300  $\mu$ Pa. Hence, using this microphone, of the right size for our purposes, we should be able to detect the desired pressure modulation.

On the basis of the feasibility observations described so far, we will now understand which are the issues related to the implementation of this sensor and how we decided to proceed for its installation on the industrial plant for the knots detection.

## 4.2 Theoretical background

The microphone that we will employ experimentally is an electret condenser microphone. In few words, a condenser microphone consists of a stretched metal diaphragm that constitutes one plate of a capacitor, while the backplate is fixed. In this way, when a sound pressure wave hits the mobile diaphragm, the capacitance varies accordingly. Generally, a stable DC voltage is applied to the plates, in a way that the change in capacitance generates an AC signal proportional to the sound waves. In an electret microphone, the DC voltage is applied through the use of an electret, that is a dielectric with a quasi-permanent electric charge given by the alignment of the static charges in the material. A layer of this material is usually placed on the backplate and supplies the voltage for polarization, in a way that no external voltage needs to be applied [63].

The flat response of the microphone, guaranteed in the low frequency range (up to about 5 kHz), requires that the sensor is not saturated by high frequency contributions. For this reason, we decided to avoid to excite the microphone with components outside the frequency range of interest, using acoustic filters. The employment of acoustic filters is widely studied for example in the development of hearing protection devices in order to avoid the exposure of workers to damaging high frequency noise components [64]. Before going into the details of the design and test of the acoustic filters, I would like to give you an idea of the physics behind this concept.

### 4.2.1 Wave equation, speed of sound and sound pressure level

The physics behind an acoustic filter can be understood just with a comprehension of what are acoustic waves and which are their governing equations. Acoustic waves are pressure fluctuations occurring in a compressible fluid. To connect the motion of a fluid with its compression or expansion, a relation between the particle velocity ( $\vec{u}$ ) and the density ( $\rho$ ) is required. If we consider a small parallelepiped volume element, the inlet mass rate that flows in the volume needs to correspond to a time density variation. This consideration leads to the **continuity equation**:

$$\frac{\partial \rho}{\partial t} + \nabla \cdot (\rho \vec{u}) = 0 \quad (4.1)$$

if

$$\rho = \rho_0(1 + s) \quad (4.2)$$

with  $\rho_0$ , the density in equilibrium conditions, a weak function of time and  $s$  a small density variation, Eq.4.1 becomes:

$$\rho_0 \frac{\partial s}{\partial t} + \nabla \cdot (\rho_0 \vec{u}) = 0 \quad (4.3)$$

and if  $\rho_0$  is a weak function of space

$$\frac{\partial s}{\partial t} + \nabla \cdot \vec{u} = 0 \quad (4.4)$$

Additionally, the temporal variation of the particles velocity is related to a gradient pressure  $\nabla p$ , as indicated in the **Euler's equation**:

$$\rho_0 \frac{\partial \vec{u}}{\partial t} = -\nabla p \quad (4.5)$$

Considering the divergence of Eq.4.5

$$\nabla \cdot \left( \rho_0 \frac{\partial \vec{u}}{\partial t} \right) = -\nabla^2 p \quad (4.6)$$

the time derivative of Eq.4.4

$$\rho_0 \frac{\partial^2 s}{\partial t^2} + \nabla \cdot \left( \rho_0 \frac{\partial \vec{u}}{\partial t} \right) = 0 \quad (4.7)$$

and substituting for the divergence term, we obtain:

$$\nabla^2 p = \rho_0 \frac{\partial^2 s}{\partial t^2} \quad (4.8)$$

Considering  $\mathcal{P}$ , the instantaneous pressure in a certain spatial coordinate and  $\mathcal{P}_0$  the equilibrium pressure, the acoustic pressure is given by  $p = \mathcal{P} - \mathcal{P}_0$ . For fluids other than perfect gases we have:

$$\mathcal{P} = \mathcal{P}_0 + \left. \frac{\partial \mathcal{P}}{\partial \rho} \right|_{\rho_0} (\rho - \rho_0) \quad (4.9)$$

substituting for  $c_s$  as follows:

$$c_s^2 = \left. \frac{\partial \mathcal{P}}{\partial \rho} \right|_{\rho_0} \quad (4.10)$$

Eq.4.9 turns into

$$\mathcal{P} = \mathcal{P}_0 + c_s^2 (\rho - \rho_0) \quad (4.11)$$

and hence, due to Eq.4.2

$$p = \mathcal{P} - \mathcal{P}_0 = c_s^2 \rho_0 s \quad (4.12)$$

Considering this result, Eq.4.8 can be rewritten as:

$$\nabla^2 p = \frac{1}{c_s^2} \frac{\partial^2 p}{\partial t^2} \quad (4.13)$$

This is the linear, lossless **wave equation** for a wave propagating in media with sound speeds that are functions of space [65]. Considering the simple case of a plane wave propagating along the  $x$  axis, the wave equation turns into

$$\frac{\partial^2 p}{\partial x^2} = \frac{1}{c^2} \frac{\partial^2 p}{\partial t^2} \quad (4.14)$$

Any plane-wave disturbance moving with a constant velocity  $v$  has the form  $f(x - vt)$ . Substituting this solution in Eq.4.14, we easily derive that it satisfies the wave equation just provided that  $v$  is equal to  $c_s$ .

In this way, we have related the **wave velocity** to the property of the medium. In a sound wave, pressure varies with density without heat flow. According to Laplace, when sound travels in a gas, there is no time for heat conduction in the medium and so the propagation of sound is adiabatic, in the sense that pressure and temperature change adiabatically in the sound wave. The heat flow from the high pressure to the low pressure region is negligible as far as the wavelength is long compared with the mean free path. In this case, the small heat flow does not affect the speed, even if it involves a small absorption of the sound energy. So, for ideal gases, we need to consider the adiabatic relation  $PV^\gamma = c_1$ , with  $\gamma = c_p/c_v$  or, in other terms,  $P = c_2 \rho^\gamma$ .

From Eq.4.10,

$$c_s^2 = \frac{\gamma P}{\rho} = \frac{\gamma RT}{\mu} \quad (4.15)$$

with  $\mu$  the molecular weight [66]. At sea level, 21°C temperature and under normal atmospheric conditions, the speed of sound is 344 m/s.

Since we are dealing with pressure waves, a short parenthesis about the concept of **sound pressure level** (SPL) is necessary. SPL is a logarithmic measure of the sound pressure, relative to a reference value  $P_0$  that corresponds to the threshold of human hearing, where  $P_0 = 20 \mu Pa$ . Hence, SPL is defined as

$$SPL = \log_{10} \left( \frac{P}{P_0} \right) \quad (4.16)$$

in a way that 0 dB SPL is the lower limit of audibility and 160 dB is the threshold of pain, that corresponds to a pressure of 2 kPa.

#### 4.2.2 The acoustic impedance

Considering the complex form of the harmonic solution for Eq.4.14

$$p = Ae^{i(\omega t - kx)} + Be^{i(\omega t + kx)} \quad (4.17)$$

with  $k = \omega/c_s$ , and substituting it in the 1D version of Euler's equation (Eq.4.5) we get

$$u = \frac{p}{\rho_0 c_s} \quad (4.18)$$

At this point we can evaluate the acoustic impedance of a plane wave, that is a measure of the resistance a system offers to the acoustic flow caused by an applied acoustic pressure. The acoustic impedance  $z$  establishes the relationship between the acting sound pressure  $p$  and the resulting particle velocity  $u$  as

$$z = \frac{p}{u} \quad (4.19)$$

that for a plane wave is

$$z_{pw} = \rho_0 c_s \quad (4.20)$$

It is also called specific acoustic impedance of the medium because it is a property of the medium itself. When the acoustic wave is propagating into a pipe of cross sectional area  $S$ , we need to consider that the amount of fluid that can pass through the pipe in a unit of time is given by  $uS$  and it can be easily deduced that for a plane wave in a pipe, the acoustic impedance will be given by

$$z_{pwp} = \frac{\rho_0 c}{S} \quad (4.21)$$

The larger the surface of a radiating sound source or the cross section of a column of air, the lower the acoustic impedance that opposes its motion.

### 4.2.3 Acoustic filters

Eq.4.21 indicates that the acoustic impedance depends on the cross section of the pipe. Hence,  $S$  is a fundamental parameter in determining the reflection and transmission coefficients when a plane wave propagates in pipes with different cross sectional area. We are interested in studying the behavior of a plane wave propagating through a pipe changing two times the section. This situation can be simplified considering a plane sound wave propagating through three different media, with acoustic impedance  $z_1$ ,  $z_2$  and  $z_3$  respectively, as shown in Fig.4.5.

When an incident acoustic wave in medium 1 reaches the boundary between media 1 and 2, some of the energy is reflected and some is transmitted into the second medium and so on. The various transmitted and reflected waves then combine so that in the steady state we can assume to have the following

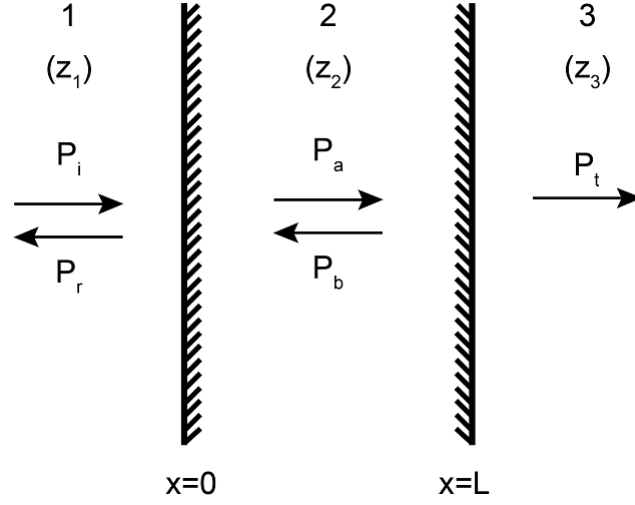


Figure 4.5: Reflection and transmission of a plane wave propagating through three different media with normal incidence.

equations for pressure:

$$\begin{aligned}
 p_i &= P_i e^{i(\omega t - k_1 x)} \\
 p_r &= P_r e^{i(\omega t + k_1 x)} \\
 p_a &= A e^{i(\omega t - k_2 x)} \\
 p_b &= B e^{i(\omega t + k_2 x)} \\
 p_t &= P_t e^{i(\omega t - k_3 x)}
 \end{aligned} \tag{4.22}$$

Imposing the continuity of the acoustic impedance in  $x = 0$  and  $x = L$

$$\frac{P_i + P_r}{P_i - P_r} = \frac{z_2}{z_1} \frac{A + B}{A - B} \quad \frac{A e^{-ik_2 L} + B e^{ik_2 L}}{A e^{-ik_2 L} - B e^{ik_2 L}} = \frac{z_3}{z_2} \tag{4.23}$$

we can easily calculate the reflection and hence the transmission coefficient. To guarantee energy conservation, the coefficients need to satisfy the following properties:

$$R = \frac{P_r}{P_i} \quad T = \frac{P_t}{P_i} \quad |R|^2 + |T|^2 = 1. \tag{4.24}$$

Using Eq.4.23 we obtain

$$R = \frac{(1 - z_1/z_3) \cos k_2 L + i(z_2/z_3 - z_1/z_2) \sin k_2 L}{(1 + z_1/z_3) \cos k_2 L + i(z_2/z_3 + z_1/z_2) \sin k_2 L} \tag{4.25}$$

and hence from Eq.4.24 we get the intensity transmission coefficient

$$|T|^2 = \frac{4}{2 + (z_3/z_1 + z_1/z_3) \cos^2 k_2 L + (z_2^2/z_1 z_3 + z_1 z_3/z_2^2) \sin^2 k_2 L} \tag{4.26}$$

that, in the simplified case of  $z_1 = z_3$ , leads to

$$|T|^2 = \frac{1}{1 + \frac{1}{4}(z_2/z_1 - z_1/z_2)^2 \sin^2 k_2 L} \quad (4.27)$$

If the variation of acoustic impedance is given by sound propagating in pipes with different cross sectional areas  $S_2$  and  $S_1$ , due to Eq.4.21, the transmission coefficient becomes

$$|T|^2 = \frac{1}{1 + \frac{1}{4}(S_2/S_1 - S_1/S_2)^2 \sin^2 k_2 L} \quad (4.28)$$

If for example we consider  $r_2 = 1$  mm, we can evaluate the transmission coefficient for different combinations of  $L$  and  $r_1$ , at a certain frequency. In Fig.4.6 (A) is shown the behavior of  $T$  for a frequency of 1.5 kHz as a function of  $L$  and  $r_1$ . We observe that transmittance increases for low  $r_1$  and high  $L$  values. In this way, we can design the filter according to the desired cutoff frequency.

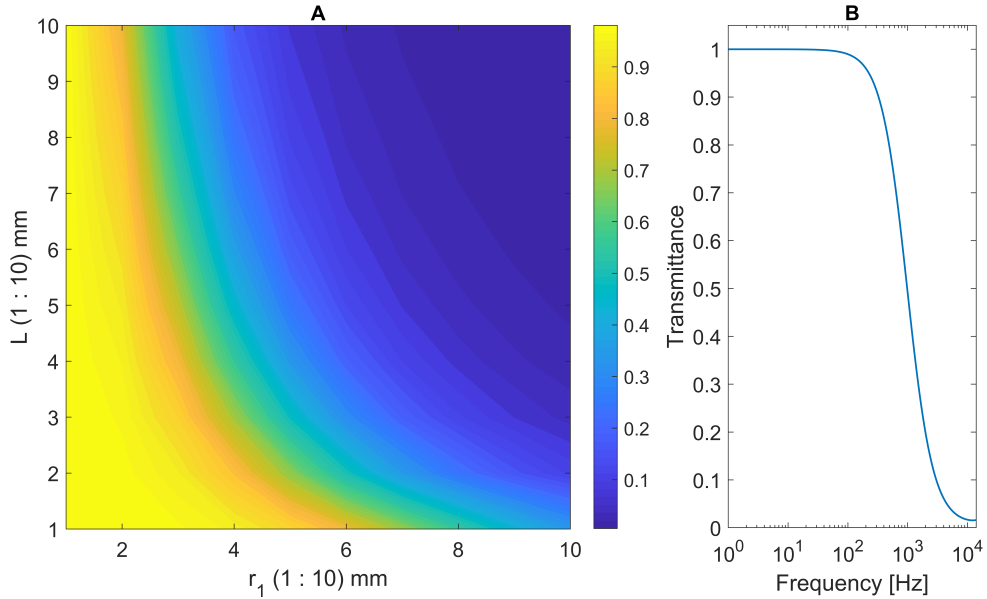


Figure 4.6: Transmittance (colorbar) for different combinations of  $L$  and  $r_1$ , for a fixed frequency value of 1.5 kHz (A). Transmittance variation with frequency, when  $r_1 = 3.5$  mm and  $L = 9$  mm (B).

If we are interested in a filter with a 1.5 kHz cutoff frequency (transmittance value of 0.3), the required parameters are  $r_2 = 3.5$  mm and  $L = 9$  mm. The result is shown in Fig.4.6 (B), indicating that the transmittance decreases as frequency approaches 1.5 kHz. In general, the geometry of the pipes can be properly changed to get a low-pass filter with the desired cutoff frequency.

### 4.3 Experimental measurements

#### 4.3.1 Experimental setup

The measurements reported in this chapter have been realized using the electret condenser microphone EK3033, Knowles Electronics as shown in Fig.4.7.

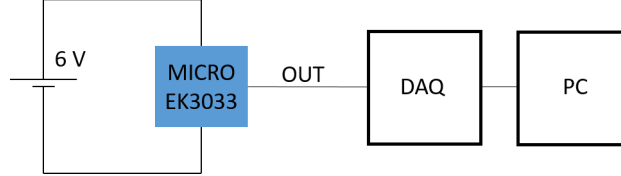


Figure 4.7: *Experimental setup for the acoustic measurements.*

The microphone is powered with an external battery of 6 V and the output voltage of the sensor is acquired by the **data acquisition board** (DAQ) NI USB-4432. To evaluate the frequency response, the signal is further processed using LabVIEW. The program performed the FFT of a 1 s signal, acquiring 40 kSamples with a sampling frequency of 40 kHz using a Hann window. Data processing and averaging is performed as described in Sec.3.2, considering 30 averages of the calculated signal PSD. In this way, the overall time required for each acquisition step was 30 s.

Also the time signal is acquired and saved on the PC, to be further analyzed with MATLAB.

#### 4.3.2 Acoustic filter design

We projected and tested filters with different cutoff frequencies, to evaluate the goodness of Eq.4.28 in the prediction of the behavior of the filter. We changed the geometrical parameters shown in Fig.4.8.

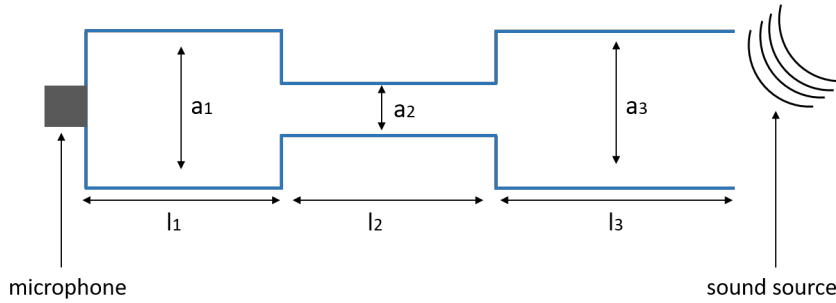


Figure 4.8: *Design and key parameters of an acoustic filter.*

In case of  $a_1 = a_3 = 8$  mm,  $a_2 = 2$  mm,  $l_1 = 14.6$  mm,  $l_2 = 9$  mm,  $l_3 = 29.4$  mm,



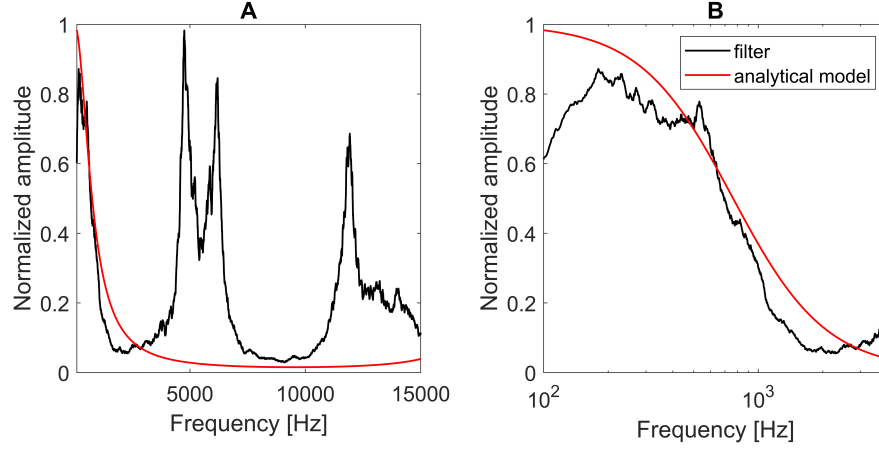


Figure 4.9: Comparison of the frequency response of a filter excited by white noise (black) with the analytical model (red) in the whole frequency range (A); x-log scale in the low frequency range, to draw the attention to the low frequency filter decay (B).

we stimulated the microphone with white noise and studied the frequency response, with the arrangement shown in Fig.4.8.

The comparison between the experimental results and the analytical model is reported in Fig.4.9.

The analytical model predicts well the slope and the cutoff frequency of the filter, as we can observe in Fig.4.9 (B), but it does not take into account the occurrence of the peaks at higher frequency values, that are shown in the experimental spectrum of Fig.4.9 (A). We hypothesize that the higher frequency components are caused by resonances of the pipes forming the filter, that are not taken into account by the simplified analytical model.

For this reason, we decided to perform an acoustic 3D FEM simulation of the filter, using the acoustics and pipe flow modules of COMSOL Multiphysics®. We reproduced the same filter geometry and constraints employed experimentally, and simulating a white noise solicitation at one end of the filter, we monitored acoustic pressure at the other end.

In Fig.4.10 we observe that the free microphone (A) measures high frequency components, damped when the filter is applied to the microphone (B). The FEM simulation reproduces well the frequency response observed experimentally, as clearly visible comparing Fig.4.10 (B) and (D).

So, we own a tool that predicts the behavior of the filter and that allows us to design the optimal geometry for the interlacing measurement.

The desired cutoff frequency is 2 kHz, avoiding unwanted resonances in the frequency range of interest. The geometry chosen was  $a_1 = a_3 = 7$  mm,

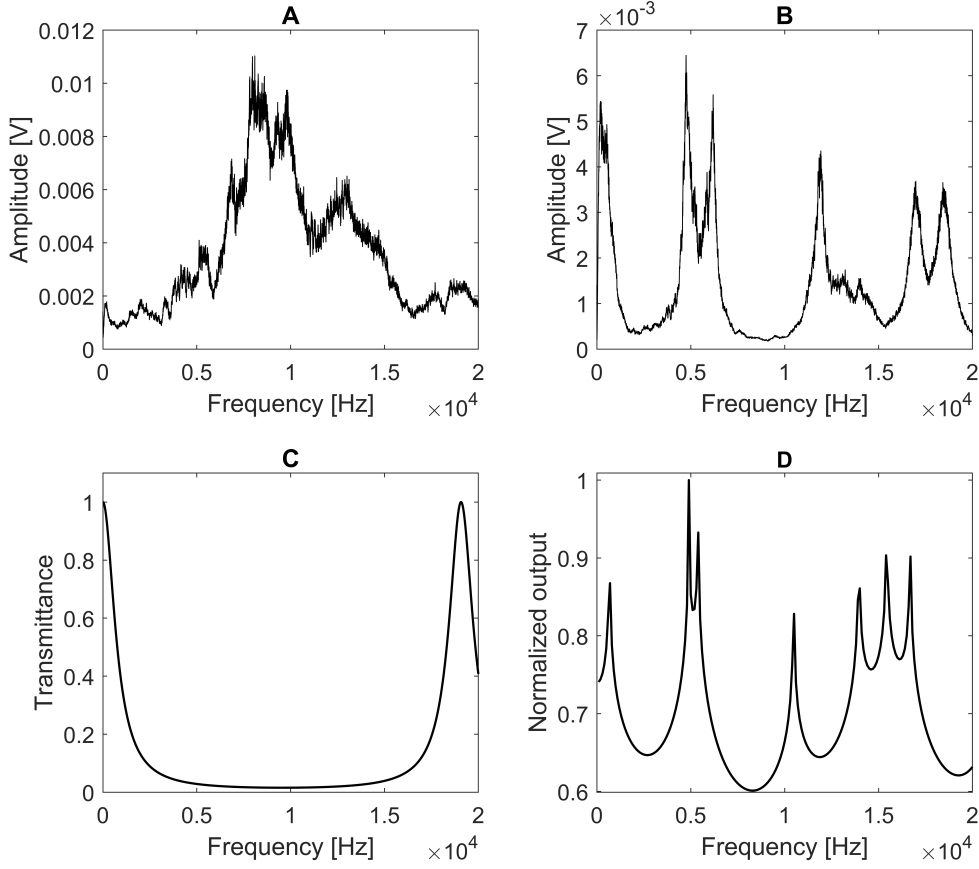


Figure 4.10: Experimental response of the free microphone excited by an external noise (A) and with the acoustic filter (B). Transmittance predicted by the analytical model (C). 3D FEM simulation with the same filter geometry used experimentally (D).

$a_2 = 2\text{ mm}$ ,  $l_1 = 10\text{ mm}$ ,  $l_2 = 6\text{ mm}$ ,  $l_3 = 7\text{ mm}$ . The comparison of the frequency response of the filtered microphone with respect to the free microphone (without any filter) is shown in Fig.4.11.

The response is similar up to about 2 kHz, while the higher frequency components are damped by the acoustic filter, as desired.

As a further test, we excited the microphone with the same external solicitation in both configurations, with and without the filter. The solicitation frequency was lower than the filter cutoff frequency. In both cases, we measured the same amplitude.

This result indicates that the filter is damping just the high frequency components, while the signal keeps unchanged in the frequency range of interest.

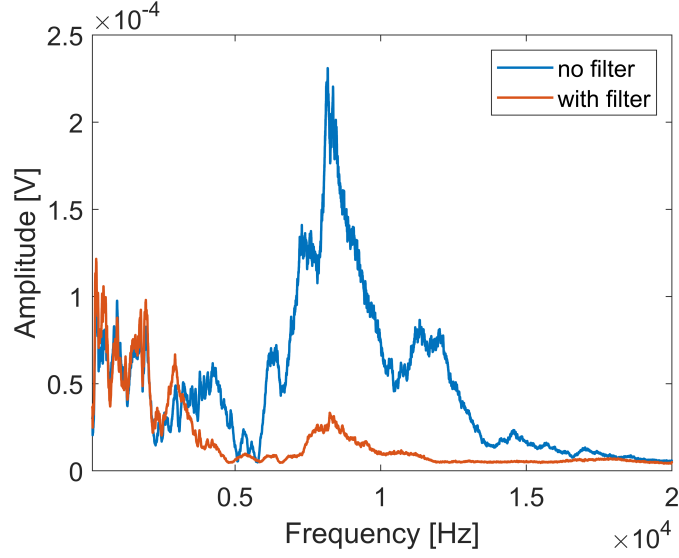


Figure 4.11: Comparison of the frequency responses of the free (blue) and filtered (red) microphone. This is the filter employed for the following measurements with the yarn.

### 4.3.3 Sensing of the interlaced yarn

Using the filter just described, we decided to test the capability of the microphone to sense the interlacing yarn. We performed the measurement with two microphones, one aligned with the running yarn (in front of the yarn, about 2 mm away), while the other one is moved about 1 cm away from the yarn (non aligned), as schematized in Fig.4.12.

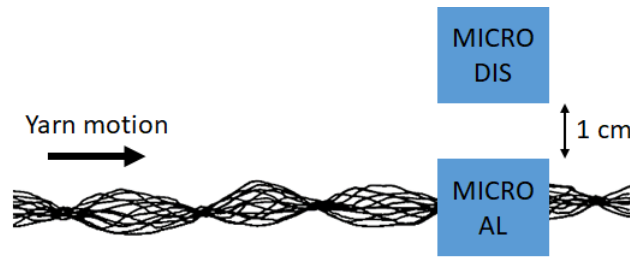


Figure 4.12: Relative sensors positions with respect to the running yarn, aligned (micro al) and not aligned (micro dis).

The simulation predicted a damping of the pressure modulation moving away from the yarn (Sec. 4.1.2). For this reason, we expect that the not aligned microphone does not sense interlacing. The measurements were performed with an interlaced yarn running with a speed of 400 m/min, acquired and analyzed

as reported in Sec. 4.3.1; the microphone output signal has been divided by its sensitivity (22.4 mV/Pa) to obtain a pressure information. The comparison of the resulting spectra, obtained from the 30 averaged power spectral density, is shown in Fig.4.13.

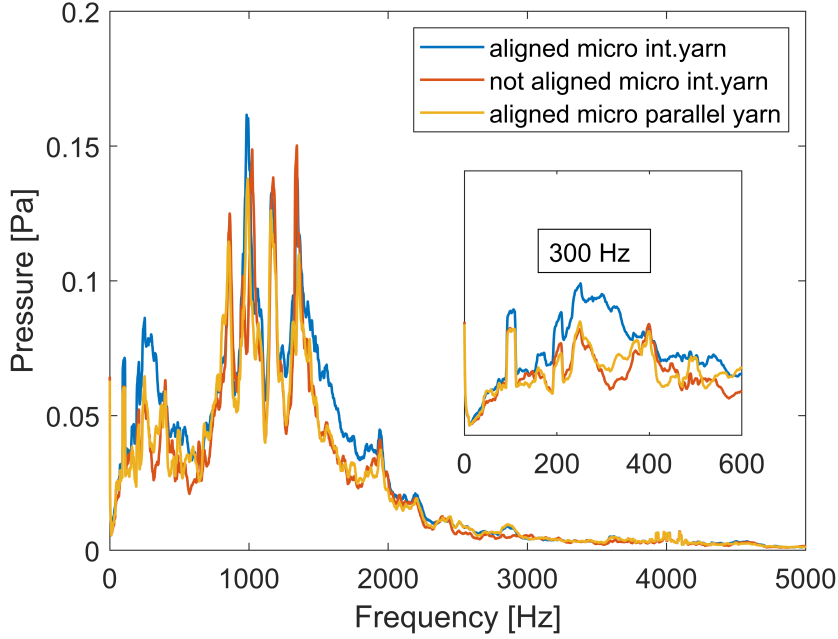


Figure 4.13: Acoustic spectra recorded with the filtered microphone aligned with the interlaced yarn (blue), not aligned with the interlaced yarn (red) and aligned with a parallel yarn (yellow). Inset: zoom of the low frequency region, with an indication of the frequency component present only in the blue spectrum.

We observe that the three spectra show almost the same frequency components, except for one peak around 300 Hz, present just when the microphone is aligned to the running interlaced yarn.

In order to understand if this component is related to the interlacing process, we performed the measurement changing the **yarn speed**. Differently from the previous case, we consider an already interlaced yarn, running with increasing speed values. For this reason, we expect to measure the same mean knots distance in the different cases. The resulting spectra reported in Fig.4.14 indicate again the same frequency components, except for one new peak, increasing in amplitude and frequency with the yarn speed, as predicted by the simulation (Fig.4.4). In addition, we observe a **baseline contribution** in the low frequency range, probably caused by some irregularities in the yarn profile. The yarn is not smooth, since it has been texturized before interlacing (Sec. 1.1.2). If the baseline components are caused by texturization, they should be

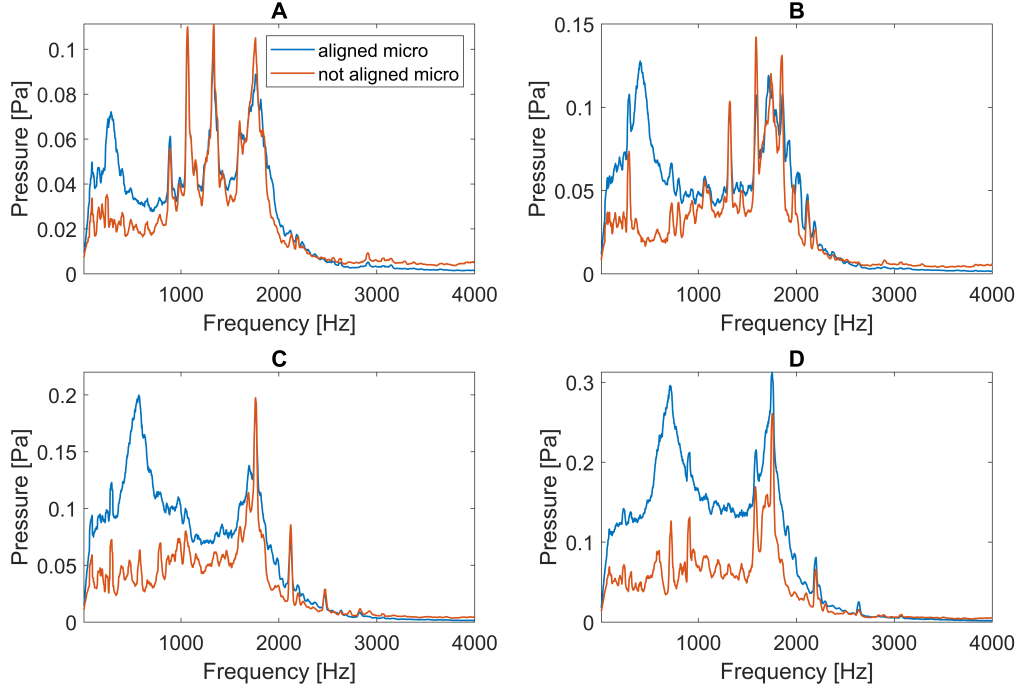


Figure 4.14: Acoustic spectra recorded with the filtered microphone for different yarn speed values, aligned (blue) and not aligned (red) with the interlacing yarn; ; 400 m/min (A), 600 m/min (B), 800 m/min (C), 1000 m/min (D).

present also with the parallel (not-interlaced) yarn. For this reason, we compared the signal measured by the aligned microphone both with an interlaced and a parallel running yarn.

In Fig.4.15 we observe that also the parallel yarn exhibits the baseline low frequency components. We deduce that they are caused by the irregular profile, given also by yarn torsion, rotation and oscillation. It is reasonable to suppose that this contribution is higher when the yarn is interlaced since the interlacing process introduces additional irregularities in the final yarn.

We still need to demonstrate that the new frequency component corresponds to the interlacing frequency. For this reason, in parallel to the microphone measurement, we performed simultaneously a **high speed video** of the interlaced yarn for each yarn speed. We analyzed the frames of the video in order to acquire the yarn profile over time. The FFT of the width of the interlaced yarn over time gives an information about the frequency of the process, that can be easily compared with the one measured by the acoustic measurement. We fit both the acoustic and the high speed spectra with a Gaussian distribution, as shown in Fig.4.16 (A), having subtracted the baseline signal from the spectrum. From the Gaussian fit, we extracted the central frequency of the

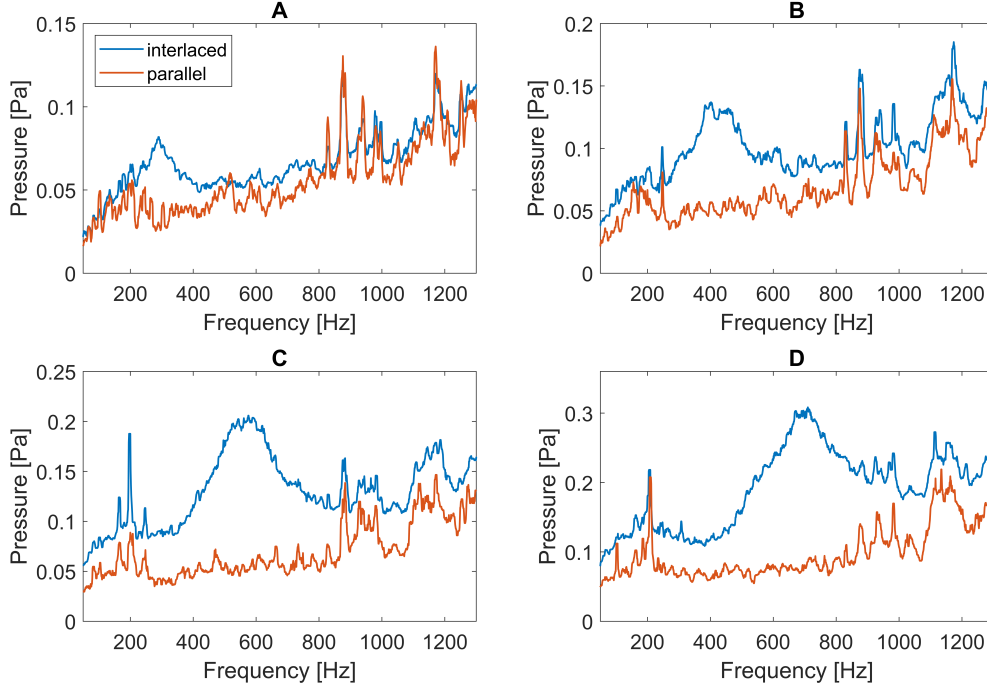


Figure 4.15: Acoustic spectra recorded with the filtered microphone at different yarn speed, aligned with the interlaced (blue) and parallel (red) yarn; 400 m/min (A), 600 m/min (B), 800 m/min (C), 1000 m/min (D).

distribution and repeating the measurements we calculated the error in the estimate. In Fig.4.16 (B) we observe an agreement in the frequency obtained with the two approaches. This result allows us to state that the microphones, positioned few millimeters away from the running interlaced yarn, sense the knots in the yarn and give an estimate of the mean value of knots per meter (Fig.4.17, B). The distance between knots is constant with the yarn speed, as expected, since we are analyzing the same yarn running at increasing speed values, while in the previous case we were changing the yarn speed during interlacing (Fig.2.6).

In Fig.4.17 (A) is shown that the amplitude of pressure modulation increases almost linearly with the yarn speed, as indicated also by the FEM simulation (Fig.4.4). The pressure modulation predicted by the simulation was about one order of magnitude higher than the measured one. The yarn was modeled with an ideal regularly shaped, rigid object, while we are actually dealing with an irregular, moving, plastic object, that dissipates part of the energy. In any case, both the experimental measurement and the FEM simulation point at an increase in the pressure modulation with the yarn speed.

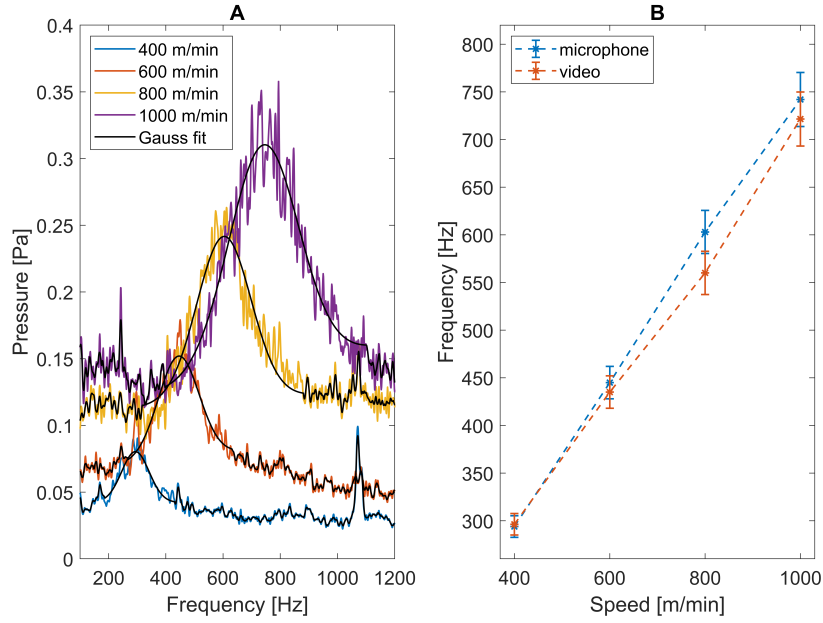


Figure 4.16: Gaussian fit of the acoustic spectra for increasing yarn speed values (A). Comparison of the central frequency of the Gaussian distribution obtained with the microphone (blue) and with the high speed analysis (red) (B).

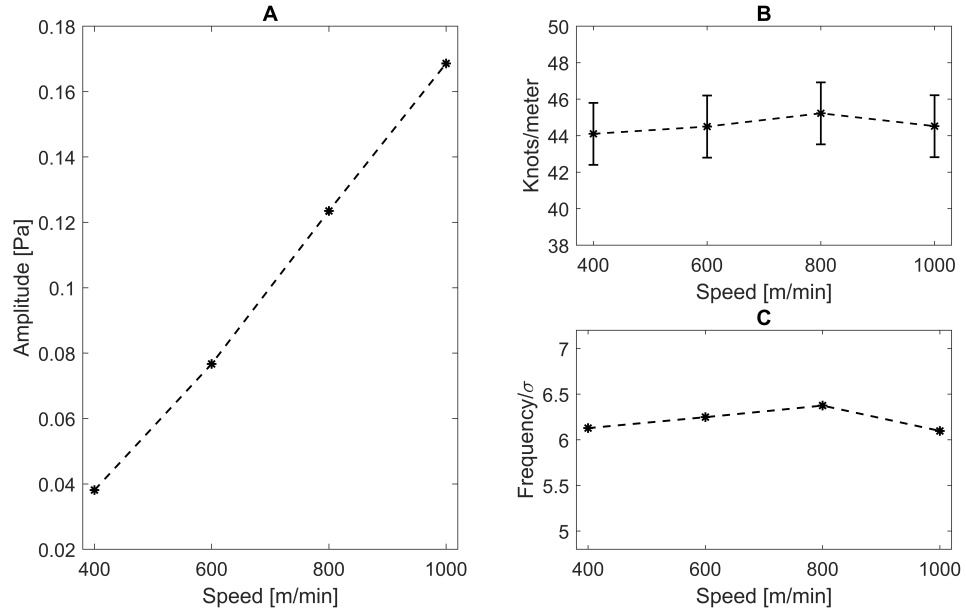


Figure 4.17: Parameters obtained from the Gaussian fit of Fig.4.16. Amplitude of pressure modulation (A); evaluation of the knots/meter (B); central frequency divided by the Gaussian width (C).

Fig.4.16 (A) indicates an increase in the width of the Gaussian distribution with the yarn speed; the relative width  $F_0/\sigma$  is constant (Fig.4.17, C).

This parameter accounts for the regularity of the process and is expected to be constant, since we are analyzing the same yarn running with different speed values. Also in this case the contribution of spectral leakages is not affecting the width of the distribution. Since the signal analyzed is 1 s long, the main lobe width for a Hanning window is 2 Hz, while typical  $\sigma$  values range from 40 Hz to 120 Hz increasing the yarn speed.

#### 4.3.4 Improvement of yarn signal over external noise

The baseline signal and the higher frequency components that we observe in the spectra of Fig.4.14 are caused by external noise sources, such as the gears and engines of the machineries, people speaking and moving in the surroundings and other sources of industrial noise. We investigated three different ways to reduce those unwanted contributions.

**Anechoic chamber** The first idea analyzed was to place the microphone into an anechoic chamber, in order to insulate the sensor from the external environment. We chose as sound absorber a fibrous porous material, in our case a sort of felt. In such a material, sound waves enter the pores and lose energy hitting the walls due to viscous and thermal effects. Part of the energy is dissipated via friction with the walls, part is lost due to thermal conduction. This is the reason why for the absorption mechanisms to be effective, the air path needs to be interconnected and an open pores structure is needed. The absorption efficiency is maximum for higher particles velocity values. In low frequency perturbations, particles need to travel higher distances to reach high speed values. So, a porous material acts as a low pass filter. The maximum absorption is reached when the thickness is a quarter of wavelength, that corresponds to the maximum particles speed.

When the absorber is mounted on a rigid backing, the particle velocity close to the boundary is small and hence in that region the absorption is low. In order to avoid too high materials thickness, it is possible to space porous absorbers away from the wall [67].

In our case, the anechoic chamber needs to be small enough to fit the industrial machine (maximum size of about  $10 \times 20$  cm). To guarantee the maximum efficiency of absorption in the low frequency range of our interest, we should employ a porous material about 15 cm thick. If we need to cover the whole chamber with the absorber, the minimum size of the chamber should be of about 40 cm, too large for our purposes.

There are also materials that block sound waves, characterized by a high den-



sity, low stiffness and a high loss factor. The loss factor gives a measure of the intrinsic damping of viscoelastic materials, defined as the ratio between the imaginary and real part of the complex elastic modulus. The imaginary part accounts for the energy dissipated, while the real part is related to the energy stored by the material. For example lead, compared to other metals, is characterized by a higher loss factor, of  $(2 - 70 \times 10^{-3})$ , with respect for example to aluminum, characterized by a loss factor of  $0.03 - 6 \times 10^{-3}$  [68].

For this reason, we decided to cover the surface of a box ( $10 \times 20$  cm) with lead sheets and to place inside the chamber a 5 mm thick layer of felt. However, the acoustic resonances of the box were sources of additional noise. Additionally, the chamber could not be completely closed, but two holes for the yarn transition were necessary. Comparing the measurements performed with and without the absorber, we did not appreciate any significant improvement, due to the limitations just described.

This result pushed us towards a different approach for the external noise reduction.

**Cross correlation of two microphones signals** We took inspiration from the functioning of the human binaural system that allows the localization of sound sources. The model that explains this phenomenon was first proposed by Jeffress [69] and is based on a cross-correlation type mechanism. It considers an interconnection between the fibers in the left and right ear. Observing which fiber from each ear receives an impulse at the same time, the delay between the two impulses is estimated and hence the source is localized. In this way, a binaural listener can concentrate on the speech coming from a particular location, suppressing noise from the other places (also called binaural cocktail party effect). Likewise, a multi-microphone approach is used to enhance signal and reduce unwanted background noise. If microphones are placed at different physical locations, the target signal is recorded at each microphone with a small delay. This delay can be estimated cross correlating the signals from the different microphones. Compensating for this delay and then averaging, the signal is enhanced, since it is added constructively. On the other hand, the random contributions are reduced, since they are added destructively, or in any case are combined in a more unpredictable fashion. The resulting signal to noise ratio will be greater (or at worst equal to) that of the single microphone. Of course, the higher the number of microphones employed, the better the SNR value.

This method is also commonly known as delay and sum beamforming [70]. For a correct estimation of the delay between two signals, the issue of spatial aliasing needs to be considered. The maximum distance between the sensors

corresponds to half the wavelength of the maximum frequency contained in the signal.

For example, for a frequency of 1 kHz, the maximum distance is given by

$$d_{max} = \frac{c}{2f} \simeq 17 \text{ cm.} \quad (4.29)$$

So, we decided to try this approach, placing two microphones aligned with the yarn at a distance of 4 cm from each other and changing the yarn speed. We cross correlated the signals acquired with the two microphones to obtain the relative delay (Fig.4.18, A), then we compensated for that delay, averaged the two results in time and performed the FFT. In Fig.4.18 (B) is shown the comparison of the spectrum resulting from the single microphone measurement with the one obtained after compensation.

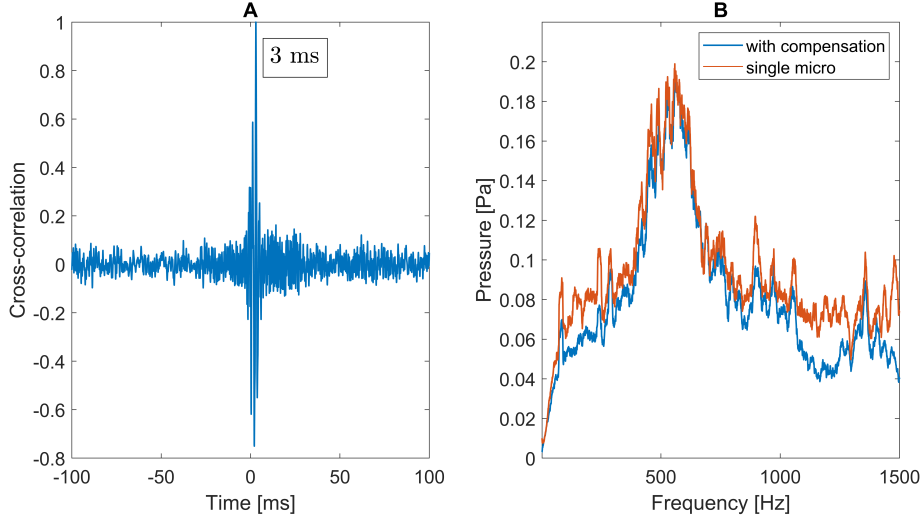


Figure 4.18: Cross correlation of signals acquired with the two microphones in case of 800 m/min yarn speed, the peak in the cross correlation at 3 ms indicates the relative signal delay (A). Comparison of the spectra of the compensated and averaged signal with the one obtained from the single microphone (B).

That comparison does not indicate any substantial signal over noise enhancement with the compensation approach, probably due to the fact that the improvement becomes more evident when a higher number of microphones is employed.

**Differential approach** Another possible approach to reduce the external noise using two microphones consists in performing a differential measurement when the microphone is aligned or not aligned to the yarn. The microphones

need to be placed close enough to each other in a way that the noise can be considered correlated (displaced about 1 cm from the yarn).

The pressure sensed by the aligned microphone contains both the signal and noise information, while the not-aligned microphone senses only the noise contribution. As a result, the difference should allow to enhance the signal.

The aim of the measurement is to discriminate the pressure modulation caused by interlacing over the other contributions. For this reason, the most significant measurement of background signal is the one given by a parallel yarn running close to the aligned microphone, with the same machine conditions of the interlaced one. So, we performed a measurement starting with the running interlaced yarn, that after about 20 s turns into parallel. We compared both the frequency spectra and the signals in time, considering the aligned and not-aligned microphones and the time difference between the two. The measurements were repeated for different values of yarn speed; here, in Fig.4.19 is reported just the case of 800 m/min yarn speed.

The frequency spectra indicate that, when the microphone is not aligned to the yarn, the low frequency spectrum is flat both with the interlaced and parallel yarn (Fig.4.19, D), while when the microphone is aligned, the interlaced yarn shows the expected frequency component around 600 Hz (Fig.4.19, E). Interestingly, the FFT of the difference of the two signals (Fig.4.19, F) shows a reduction of the unwanted noise contributions in the measurement.

The improvement in the measurement with the differential approach is evident also if we evaluate the RMS of the signal obtained both with the parallel and the interlaced yarn in the three configurations. We believe that the most significant estimate of the noise of our measurement is the pressure modulation induced by the parallel yarn, since we are interested in the component caused by the yarn profile change and not by irregularities in the yarn or by its oscillations. For this reason, in our case the SNR is given by the squared ratio of the RMS of the interlaced signal divided by the RMS measured with the parallel yarn. The SNR obtained with the differential measurement is more than two times higher than the one measured with the microphone aligned with the yarn, as reported in Table 4.1. This result gives a hint of the measurement improvement with the differential approach, simply looking at the time signal. However, for a better comparison of the capability of detecting interlacing, we need to evaluate the signal and noise components just in the frequency range interested by the process.

To extract the power contained in a signal bandwidth, we exploit the Parseval's theorem, that relates the energy of a signal in time  $x(t)$  with its Fourier

transform  $X(\omega)$  as:

$$\int_{-\infty}^{\infty} |x(t)|^2 dt = \int_{-\infty}^{\infty} |X(\omega)|^2 d\omega. \quad (4.30)$$

In our case, the spectral resolution is 1 Hz. So, the power of the signal is given by the sum of the squared FFT spectrum, in the interlacing frequency range. For example, for the measurements reported in Fig.4.19 (D, E, F), we considered the sum of the squared spectra, in the bandwidth from 350 Hz to 800 Hz.

The signal to noise ratio resulting from this calculation for the three sensor configurations is reported in Table 4.1 as  $SNR_{bdw}$ . The capability of detection of an interlaced with respect to a parallel yarn, improves about 7 times in the differential configuration, with respect to the single microphone approach.

Hence, we can conclude that for our purposes, the differential approach is more

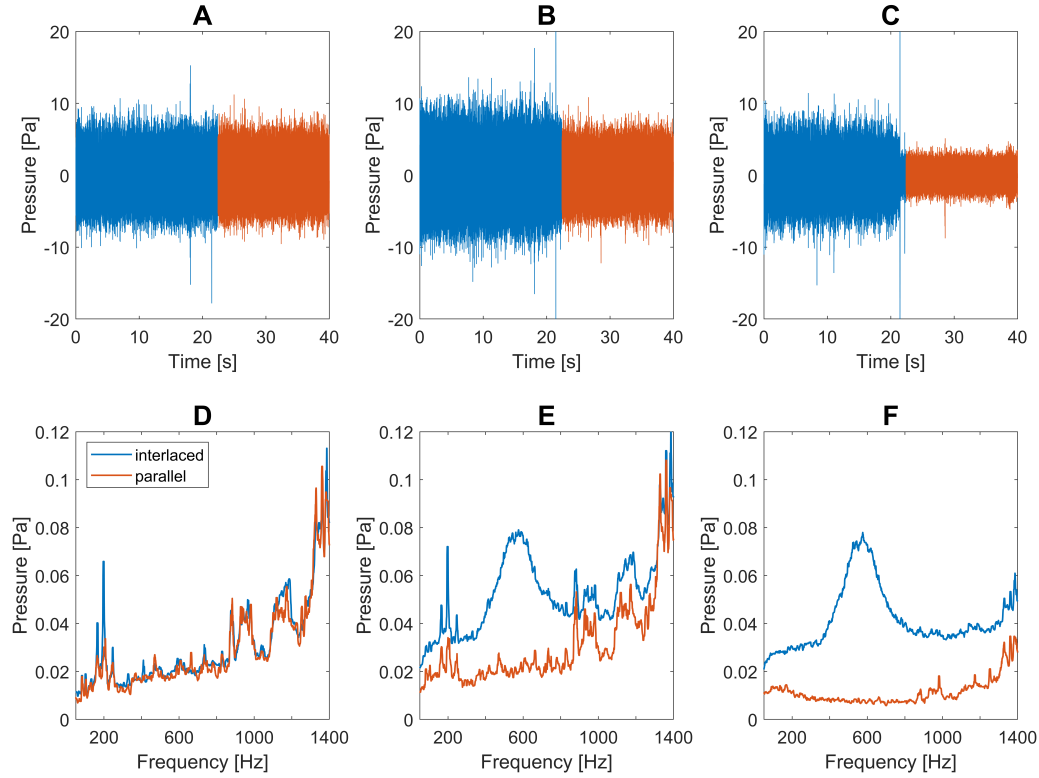


Figure 4.19: Pressure modulation over time caused by a running yarn (800 m/min yarn speed), interlaced (blue) and after 20 s parallel (red). Measured by a not aligned microphone (A), microphone aligned with the yarn (B), time difference between the two signals (C). Corresponding FFT of the interlaced (blue) and parallel (red) signals (D, E, F).

	Not aligned microphone	Aligned microphone	Difference
SNR	1	2	5
$\text{SNR}_{bdw}$	1	7	47

Table 4.1: SNR, calculated as the squared ratio of the RMS values for different microphones configurations.  $\text{SNR}_{bdw}$  calculated from the integrals of the squared spectra of Fig.4.19 in the frequency bandwidth interested by interlacing (350-800 Hz).

effective than the cross-correlation measurement if we are dealing with small spaces where just two microphones can be employed.

## 4.4 Chapter conclusions

In this chapter, we proposed and optimized a microphone-based measurement, to sense the pressure modulations caused by a running interlaced yarn. First, we performed a FEM simulation of the system; we observed the hypothesized pressure modulation and verified that it should be detectable by a microphone. We designed an acoustic filter in order to avoid frequency components that could saturate the sensor. Additionally, we compared and discussed three approaches to improve the signal over external noise and we found that a differential technique is the most effective in our case.

Keeping in mind the partial conclusions reached, we move towards the investigation of a different on-line sensing technique, for a final comparison of the two methods. For this reason, more general conclusions will be given in Sec.5.5.



# 5

## Optical sensing of an interlaced yarn

### Contents

---

<b>5.1</b>	<b>Theoretical background . . . . .</b>	<b>90</b>
5.1.1	Basic operating principles of a photodiode . . . . .	90
5.1.2	Load resistance and transimpedance amplifier . . . . .	92
5.1.3	Position sensitive detectors . . . . .	93
<b>5.2</b>	<b>Materials and methods . . . . .</b>	<b>95</b>
5.2.1	Description of the experimental setup . . . . .	95
5.2.2	Sensor calibration . . . . .	97
<b>5.3</b>	<b>Experimental measurements . . . . .</b>	<b>100</b>
5.3.1	Detection of yarn modulation . . . . .	100
5.3.2	Sources of noise . . . . .	102
5.3.3	Evaluation of the mean distance between knots . . . . .	104
5.3.4	Reconstruction of the yarn profile from the time signal . . . . .	107
<b>5.4</b>	<b>Signal processing to detect irregular patterns . . . . .</b>	<b>110</b>
5.4.1	Threshold proportional to the signal amplitude . . . . .	111
5.4.2	Cross-correlation analysis . . . . .	113
<b>5.5</b>	<b>Comparison of the acoustic and optical approach . . . . .</b>	<b>123</b>
5.5.1	Simultaneous measurement of the mean interlacing frequency . . . . .	123
5.5.2	Signal to noise ratio evaluation and comparison . . . . .	124
5.5.3	Detection of missing or irregular knots . . . . .	126

---

**Overview** The simple proof of principle idea behind the measurement with a photodiode is represented in Fig.5.1. Placing the yarn between the sensor and a source of light (such as a LED), the shadow of the yarn is projected on the sensor. In correspondence to a knot, more light is hitting the photodiode and the output signal should be higher with respect to the not-interlaced segments. Whether this idea is suitable to monitor on-line the interlacing process is the key question developed in this chapter. First, the main physical properties of photodiodes are recalled. In this way, the reader can better understand the main issues related to their experimental implementation. The sources of disturbance will be investigated, to optimize the measurement. A cross correlation signal processing approach is proposed, to move from a mean to a punctual analysis of the knots-distance.



*Figure 5.1: Schematic representation of the photodiode sensing.*

## 5.1 Theoretical background

### 5.1.1 Basic operating principles of a photodiode

Photodiodes are semiconductor devices that absorb photons and generate a current, proportional to the incident power of light. In order to understand the key features for the employment of such a sensor, we need to give a glance at its basic operating principles. The cross section of a photodiode is shown in Fig.5.2, where we can see that it is simply a P-N junction.

In the scheme, the P-type region is the photosensitive surface, while the N-layer acts as substrate. The speed and responsivity of the photodiode can be controlled changing the thickness of the bulk substrate. When the photodiode active area is illuminated by light of energy greater than the band gap, an electron-hole pair occurs throughout the material. Due to the built-in voltage across the depletion region of the P-N junction, the electrons generated by light are swept away and are collected by the cathode, in contact with the N-layer, while on the holes are collected in the P-layer positive electrode. When the electrodes are connected to an external circuit, a current is generated.



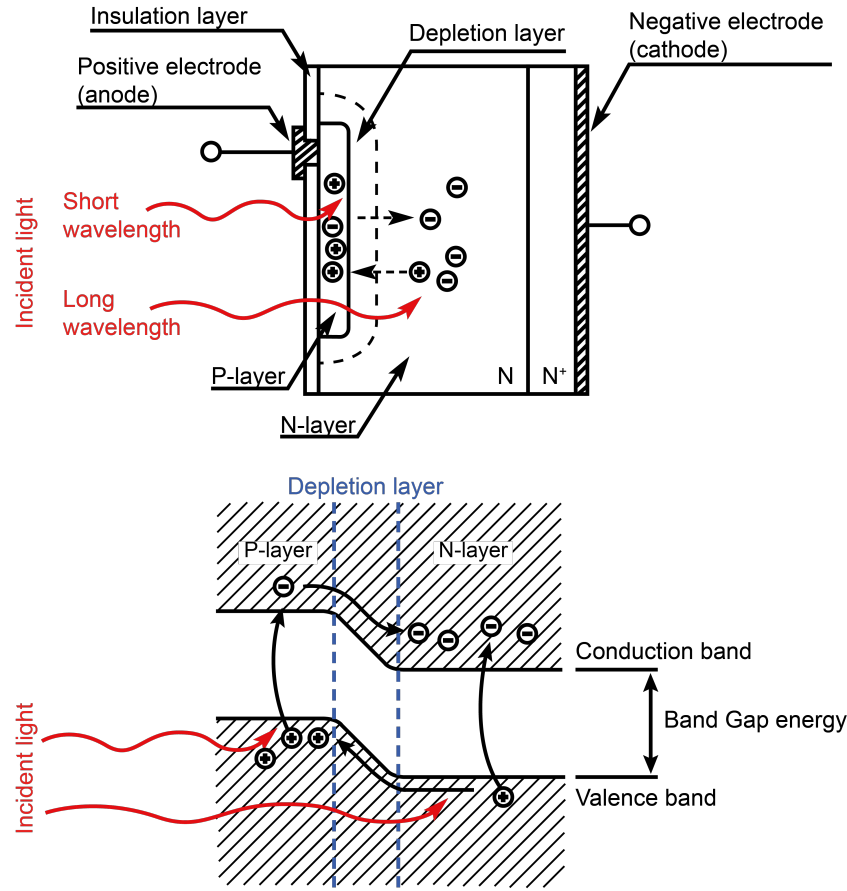


Figure 5.2: Silicon photodiode cross section (top); P-N junction energy state (bottom).

A reverse bias of the junction (also called **photoconductive mode of operation**) expands the depletion region. As a consequence, more of the diode material is affected by the accelerating field and the speed and linearity of the device are improved; on the other hand, dark and noise currents are increased. However, even in absence of the external bias, a depletion region develops at the junction due to its built-in voltage. This unbiased mode of operation is called **photovoltaic mode** and is preferred when the photodiode is used in low light level applications, due to the lower level of noise involved [71].

A model of the photodiode with discrete circuit components is necessary to allow an analysis of the application circuits. It is immediate to imagine a photodiode as an ordinary diode, but with the addition of an internally generated current derived from illumination.

The resulting **equivalent circuit**, reported in Fig.5.3, shows an ideal diode,

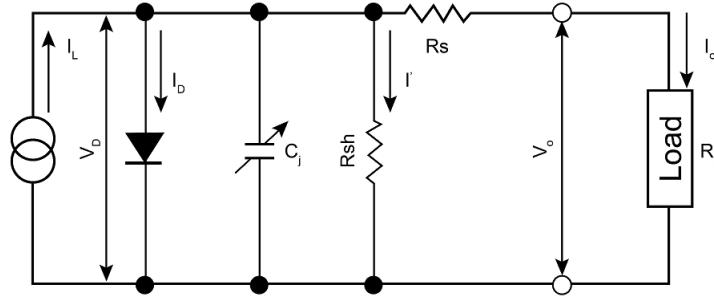


Figure 5.3: Equivalent circuit for a silicon photodiode.

a current source and accompanying parasitic elements.

The shunt resistance  $R_{sh}$  is the slope of the current-voltage curve at the origin. The series resistance  $R_s$  is caused by the resistance of the contacts and of the undepleted silicon. The junction capacitance  $C_j$  is linked to the fact that the boundaries of the depletion region act as the plates of a parallel plate capacitance.

### 5.1.2 Load resistance and transimpedance amplifier

The junction capacitance  $C_j$  plays a fundamental role when we just let the photodiode dump its current into a load resistor, as in Fig.5.3. If  $R_L$  is large, the gain will be large, but the response is slow, since the time constant will be given by  $\tau = R_L C_j$ . On the other hand, if we choose a small resistor to get a small  $\tau$ , the gain will be low. Additionally, high values of load resistance  $R_L$  do not significantly shunt the diode current, leaving part of that current to circulate within the diode. This causes an expansion of the depletion region and hence a change in the diode internal resistance. As a result, the response of the photodiode is non linear for different incidence light levels. This limit considered, we need a way to absorb the diode current without producing a voltage across it. For example, we can feed the photodiode output current directly into a transimpedance amplifier (Fig.5.4).

The current initially reacts with the high input impedance of the op-amp. Then, the open loop gain of the amplifier increases the resulting input voltage, driving the feedback resistor with an output voltage  $V_O$ . This causes the diode current to flow away from the amplifier input impedance to  $R_f$  and virtually zero voltage at the op-amp input is restored. Actually, the open loop gain of the amplifier is finite and leaves part of the voltage across the photodiode and its capacitance. This generates a signal oscillation, also caused by the input capacitance of the op-amp, when used with a feedback resistor.

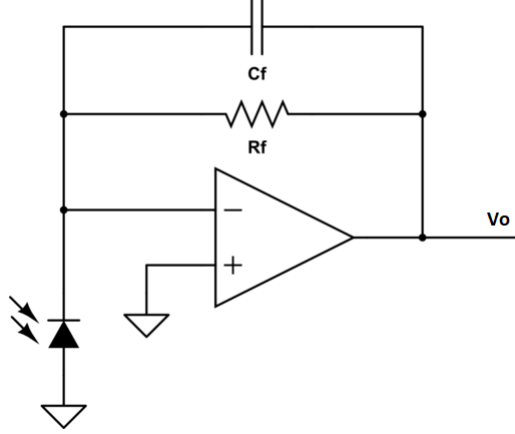


Figure 5.4: Photodiode with transimpedance amplifier.

To restore frequency stability, we can use a feedback capacitance  $C_f$ , in parallel to the feedback resistance, forming a lowpass filter with a time constant  $\tau = C_f R_f$  [72].

### 5.1.3 Position sensitive detectors

The variation of the yarn profile that we aim to detect with a photodiode could be caused both by the modulation given by the knots, but also by a yarn oscillation. For example, a previous study that employed a linear CCD indicated a variation in the detected diameter due to a yarn rotation [40]. In that case, the issue was solved superimposing two orthogonal views of the yarn motion. This is the reason why we are interested in monitoring the position and radial oscillation of the yarn over time.

Different methods have been studied to sense the position of the incident light. The most common implies the use of an array of many small detectors, in other words a linear CCD. This technique reaches high resolution values given by the pixel size, of  $7\mu\text{m}$  for more recent sensors (e.g. S13774, Hamamatsu). The readout system requires an A/D converter for each pixel and the rate of acquisition depends mainly on the exposure time and on the clock of the shift register. In the case of the sensor mentioned previously, the maximum readout speed is 100 klines/s. The main drawbacks are that linear CCDs are expensive and require additional electronics for readout.

On the other hand, a position sensitive detector is cheaper and a single A/D converter is necessary for readout. Typical errors in position detection range from  $\pm 20 - 60\mu\text{m}$ , with a  $f_{3dB} = 35\text{kHz}$  when the load resistance is  $1\text{k}\Omega$  (S5629-02, Hamamatsu).

Fig.5.5 (left) shows a schematic view of the cross section of a position sen-

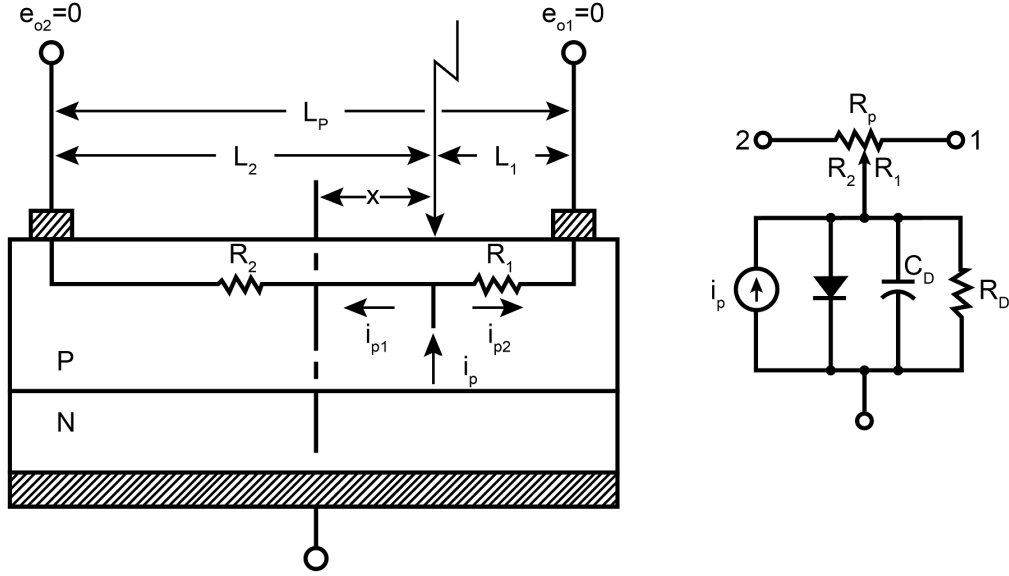


Figure 5.5: Scheme of the cross section of a position sensitive detector; the black arrow impinging from the top represents the incoming light (left). Equivalent circuit model of a position sensitive detector (right).

sitive detector that suggests the operating principle of this simple detector. The photosensitive area is also a resistive layer, in a way that when a light spot strikes the position sensitive detector, the generated electric charge flows through the resistive layer and is extracted from the output electrodes. The current is divided in two components in inverse proportion to the distance between the incidence position of light and the corresponding electrode [73]. For the circuit analysis, the equivalent model is modified with respect to the traditional photodiode, introducing  $R_1$  and  $R_2$  as the two segments of a potentiometer, where the position of the potentiometer wiper represents the location of the light beam on the photodiode (Fig.5.5, right). In this way, we can easily obtain

$$i_{p1} = \frac{R_2}{R_1 + R_2} i_p \quad i_{p2} = \frac{R_1}{R_1 + R_2} i_p \quad (5.1)$$

considering that  $R_1 = \rho L_1$  and  $R_2 = \rho L_2$ , we derive that

$$x = \frac{i_{p1} - i_{p2}}{i_{p1} + i_{p2}} L_P \quad (5.2)$$

indicating that the position of the light input signal is proportional to the difference between the currents collected by the two electrodes.

## 5.2 Materials and methods

### 5.2.1 Description of the experimental setup

The video analysis reported in the previous chapter (Sec.4.1.1, Fig.4.1) indicated that the yarn oscillates with a maximum amplitude of 3.5 mm. Additionally, we observed that the open yarn segments cover about 40% of that size, while the knot covers the 17%, in a way that the contrast between the interlaced and not interlaced region is about 23%. It is intuitive that we aim at reducing as much as possible the size of the active area of the photodiode, in order to enhance the relative difference between the opening and knots regions and hence to improve the contrast in the signal. This is the reason why we were interested in the extent of the maximum oscillation amplitude, since it corresponds to the minimum allowed sensor size, that is 3.5 mm. One example is the photodiode OSD15-5T Centronic, with an active area of  $3.8 \times 3.8$  mm. To enhance contrast, we partially covered the **photodiode**, in a way that the sensitive area is  $1 \times 3.5$  mm, lightened by a green LED (central wavelength of 520 nm). The photodiode is responsive in the range 430-900 nm. The distance between the photodiode and the light source is 4 cm. In order to enlighten uniformly the active area of the photodiode, the light from the LED source was slightly widened by means of a divergence lens. As a result, the light is emitted with an approximately conical shape characterized by a half-opening angle of  $10^\circ$ .

The circuitual scheme is reported in Fig.5.6, indicating that the photodiode was used in the transimpedance amplifier configuration.

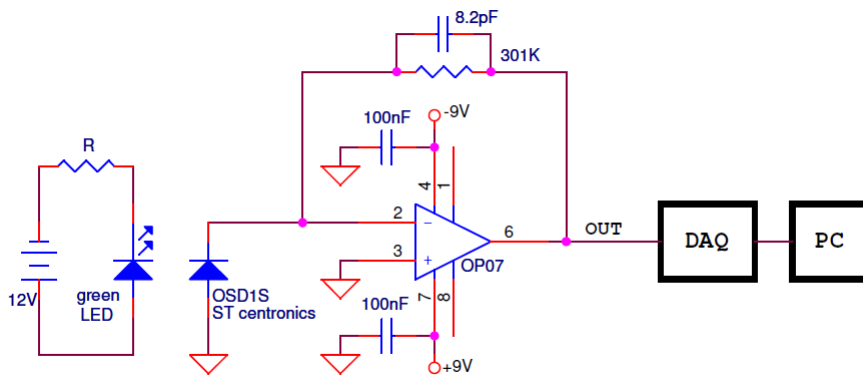


Figure 5.6: Circuitual scheme for the photodiode, with a green LED illumination.

We employed also a **position sensitive detector**, with a spectral response ranging from 760 to 1100 nm and a photosensitive area of  $1 \times 6$  mm (S5629-02

Hamamatsu). In this case, we enlighten the yarn with an infrared LED characterized by a central frequency of 836 nm. The distance between the photodiode and the light source is 4 cm also in this case.

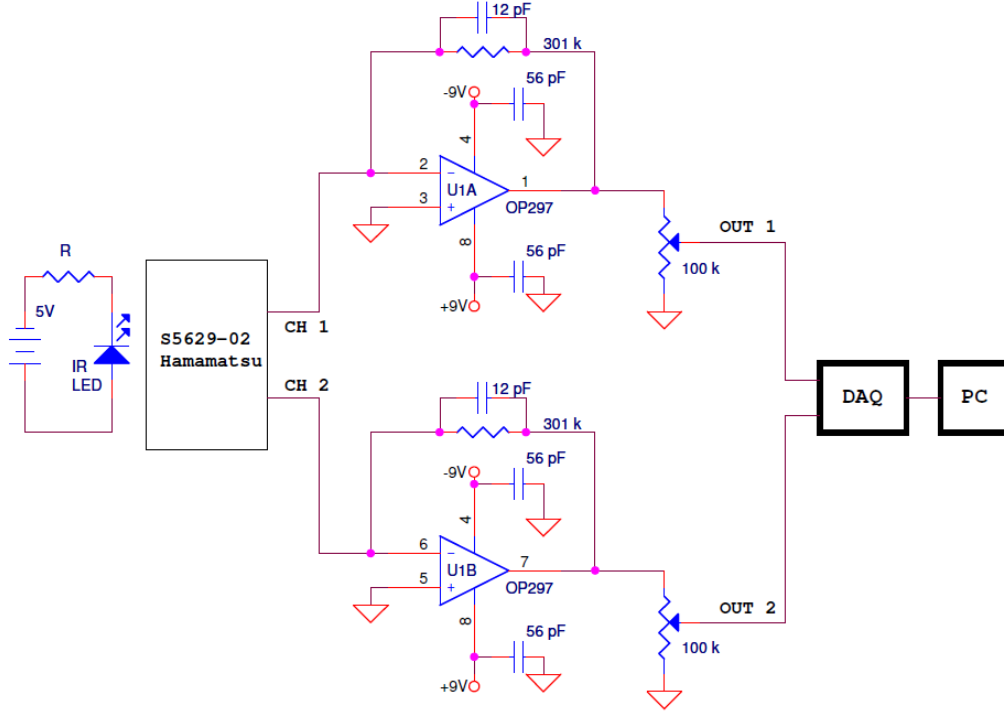


Figure 5.7: Circuitual scheme for the position sensitive detector, with IR LED illumination.

In Fig.5.7 we observe that the output of each channel of the photodiode is linked to a trimmer. The two trimmers are adjusted in a way that when the active area of the photodiode is uniformly enlightened, the resulting output signals are equal. A slightly different output is indeed caused by the small intrinsic differences in the electric components of the two circuits.

In both cases, the output signal of the sensors is acquired by the **data acquisition board** (DAQ) NI USB-4432 and the signal is further processed using LabVIEW. The program performs the FFT of a 1 s signal using a Hann window, acquiring 40 kSamples with a sampling frequency of 40 kHz, to have a 1 Hz spectral resolution. Data processing and averaging is performed as described in Sec.3.2, considering 30 averages of the calculated signal PSD. In this way, the overall time required for each acquisition step was 30 s. Also the time signal is acquired and saved on the PC, to be further analyzed with MATLAB. The measurements were performed mounting the photodiode on an industrial production machine. For each measurement, we acquired the baseline signal

with the photodiode switched off, turned on and with and without the yarn positioned, still, in front of the photodiode. Then, we performed the measurement with an already interlaced yarn, considering different yarn speed values, ranging from 400 m/min to 1000 m/min. The yarn speed is changed varying the speed of rotation of the rolls guiding the yarn, keeping a tension of 70 cN. We performed the measurements both with the interlaced and the parallel yarn. The distance between the sensor and the yarn was of about 5 mm.

### 5.2.2 Sensor calibration

The output signal of the photodiode is proportional to the incident light, that in turn depends on the yarn diameter. For this reason, we are interested in calibrating the sensor, in a way that we manage to find a relation between the output voltage and the yarn diameter. We located an optical chopper between the LED and the visible photodiode and placed metallic wires of different diameters in the empty space between the wheel blades (inset A of Fig.5.8). The wire diameters are: 0.2, 0.31, 0.5, 0.63, 0.71, 0.9 and 1 mm. In this way, as the chopper wheel is rotating, the different wires pass in front of the photodiode and their shadow is projected on the sensor.

The resulting signal, detected by the visible photodiode, is reported in Fig.5.8. We observe a low voltage signal when the wheel blade is darkening the photodiode, followed by a complete illumination of the active area, corresponding to the maximum voltage. After the peak, we observe a successive signal reduction as the photodiode is partially covered by the wire. For example, the fifth signal oscillation of Fig.5.8 corresponds to the transition of the 0.71 mm wire. In the inset of Fig.5.8 is reported in green the full illumination condition, followed by a partial shadowing caused by the wire (in red). As expected, we observe that increasing the wire diameter, the shadow increases. If we consider the mean value of the red region and we divide it by the mean value of the green signal, we obtain the relative shadowing caused by the wire. This ratio, evaluated for each wire diameter, is the key parameter for the sensor calibration; we will call it normalized amplitude.

We calibrated the sensor in both configurations: with the load resistance and with the transimpedance amplifier. Of course, the second configuration is more stable and linear, but it requires additional electronic components that increase the costs, maintenance and damage likelihood. For this reason, we decided to evaluate the sensor calibration in both configurations. We calculated the normalized amplitude for the different wire diameters changing both the incident light intensity and also the distance between the wires and the photodiode. The light intensity emitted by the LED increases linearly with the power supply.

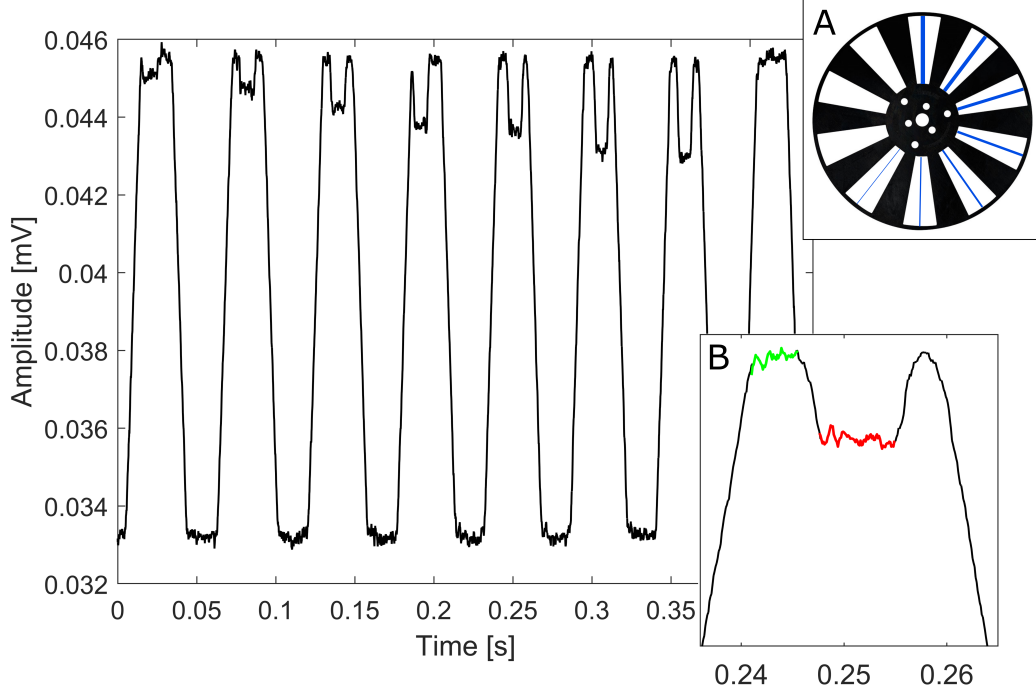


Figure 5.8: Time signal recorded for the visible photodiode calibration, with an insight into the fifth period of oscillation (inset B), in green is shown the full illumination condition, in red the partial shadowing caused by the wire. The wire diameter increases in time (from 0.2 to 1 mm) as the chopper wheel is rotating, as indicated in inset A.

In the load resistance configuration, in Fig.5.9 (A) we observe that the normalized amplitude is decreasing linearly with the yarn diameter. The slope, extracted from a linear fit and reported in Fig.5.9 (B), increases with the light intensity and this change causes a signal modulation of about 19%. In the diameters range of interest for our purpose (0.6-1.4 mm, that corresponds to the yarn dimension), we would commit an error on the diameter estimate of about 25% with a change of working conditions.

On the other hand, using the transimpedance amplifier configuration, the normalized amplitude still decreases linearly with the wire diameter, but the slope remains almost constant with the incident light intensity. We observe a small 1% fluctuation that allows a good diameter estimation (within 0.5% of uncertainty in the diameter range of interest). In addition, we also analyzed the response changing the distance between the photodiode and the wire. The slope is slightly increasing with distance, causing about a 3% signal variation for each millimeter of oscillation (Fig.5.9 (C, D)).

This variation is attributed to the  $10^\circ$  opening angle of the green LED light.



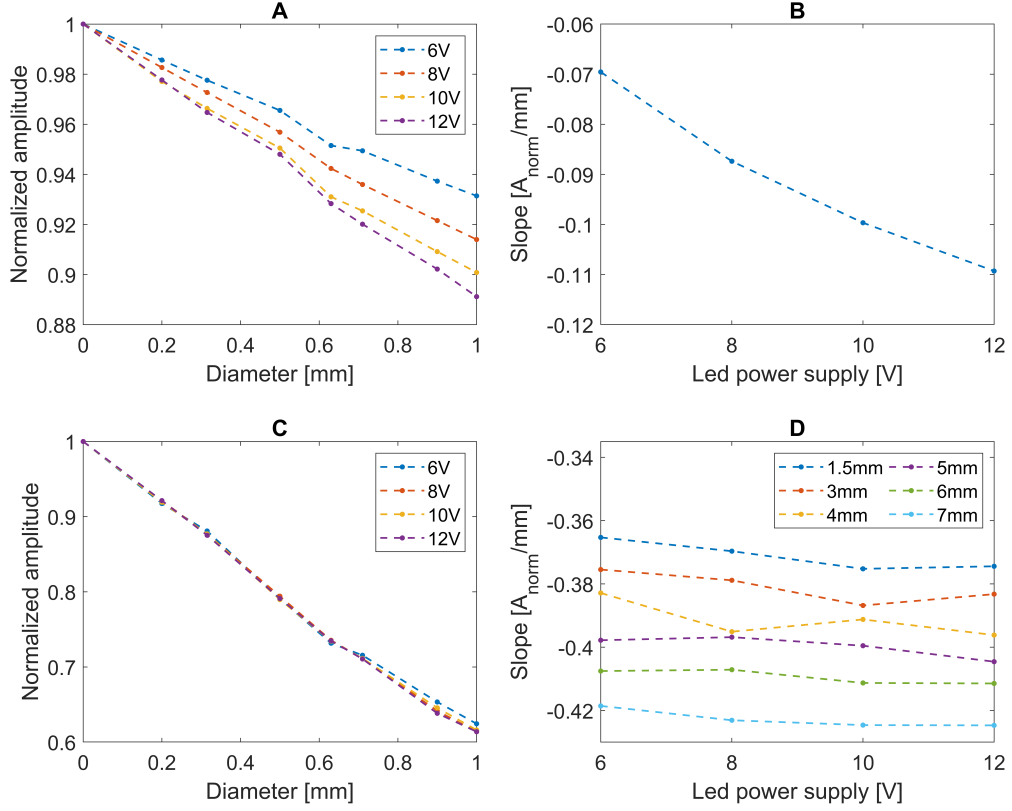


Figure 5.9: Load resistance configuration, signal variation with the wire diameter and the incident light intensity (A), slope of the previous curves as a function of light intensity (B). Transimpedance amplifier configuration, signal versus wire diameter (C) slopes of previous curves, changing also the distance wire-sensor (D).

The fit indicates that an unknown wire diameter can be predicted using the calibration with a measurement uncertainty due to linearity of about  $20\ \mu\text{m}$ . Hence, we conclude that if we want to measure and monitor the yarn diameter, we need to use the photodiode in the transimpedance amplifier configuration if we need a repeatability of the measurement, varying the external working conditions.

On the other hand, if we want to minimize the electronic components needed for the sensor, we can also use the load resistance configuration, but the diameter information is not repeatable. In that case, we should just observe a modulation caused by knots.

We could also consider to decrease the load resistance, set to the value of  $10\ \text{k}\Omega$  in this case, but at the expense of a further reduction of the signal and of the

modulation produced by the yarn, when we are already dealing with small signals (few mV of amplitude, as in Fig.5.21).

### 5.3 Experimental measurements

#### 5.3.1 Detection of yarn modulation

To observe if the photodiode is sensitive to the yarn profile variation, we used the experimental setup described in Sec.5.2.1. We enlightened with the green LED the yarn running with a speed of 800 m/min and we detected the signal with the visible photodiode (OSD15-5T Centronic). We compared the averaged frequency spectra of the signals obtained both with an interlaced and a parallel yarn, where the measurement with the parallel yarn is considered as the background reference.

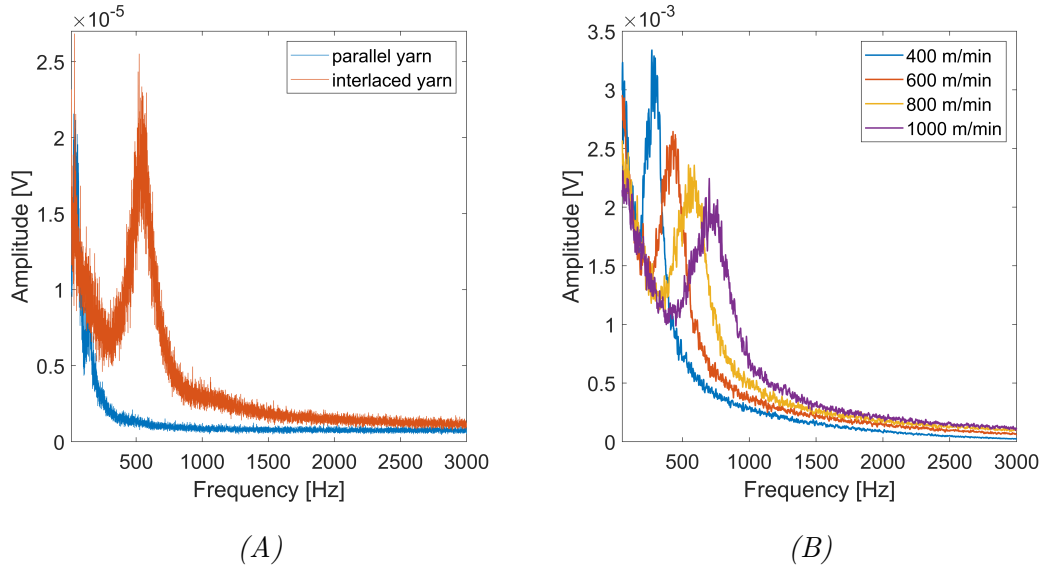


Figure 5.10: Frequency spectrum of the signal acquired with the photodiode, both with running parallel and interlaced yarn (800 m/min) (A), comparison of the spectra increasing yarn speed values (B).

In Fig.5.10 (A) we observe a clear frequency component around 530 Hz just with the interlaced yarn, while the parallel yarn shows a flat signal in this frequency band. The repetition of the same measurement changing the yarn speed indicates a shift of this component towards higher frequency values with the yarn speed (Fig.5.10, B). To individuate the central frequency of the distribution, we subtracted the baseline from the spectrum and fit it with a Gaussian (Fig.5.11, A).

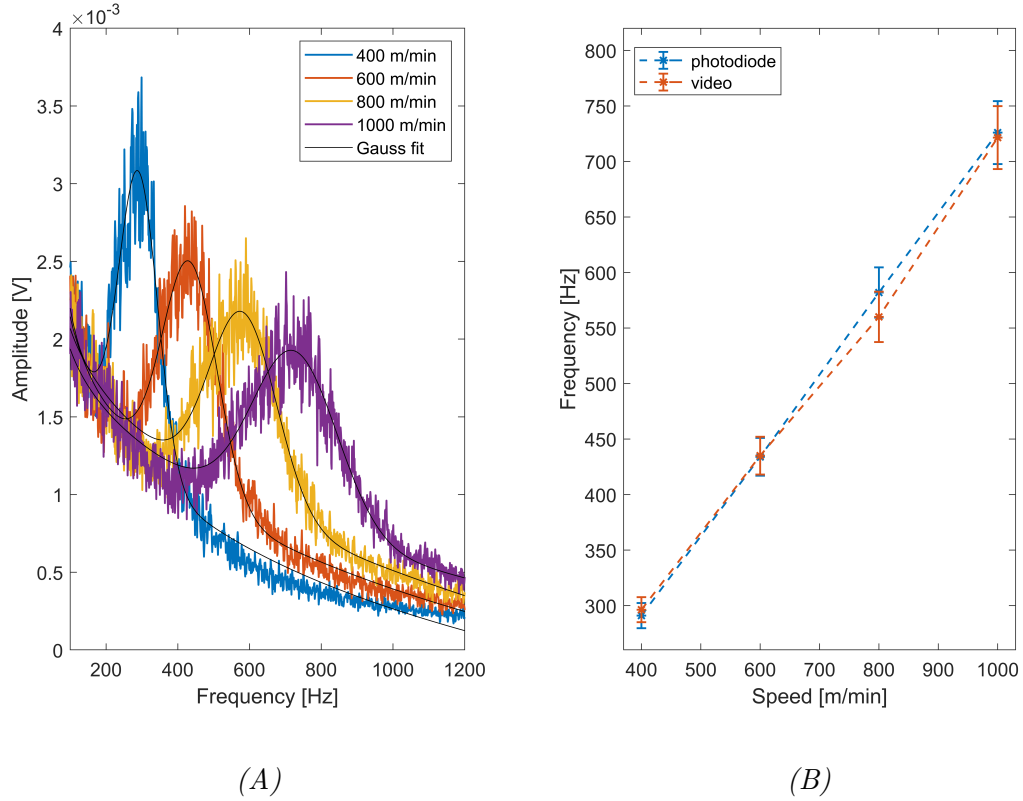


Figure 5.11: Gaussian fit of photodiode frequency spectra varying the speed of an interlaced yarn (A), central frequency obtained both with the video and with the photodiode (B).

So far, we are still not sure that the signal modulation we are observing is actually caused by the periodic knots in the interlaced yarn. For this reason, we performed a high speed video of the running yarn, simultaneously to the acquisition with the photodiode. Processing the frames of the video, we reconstructed the yarn profile over time and we evaluated its FFT. The frequency values predicted with the two techniques are in agreement (Fig.5.11, B). So, the modulation of the signal acquired with the photodiode is actually related to the interlacing process.

From the frequency values and the yarn speed, we can easily calculate the mean distance between knots. In Fig.5.12 we observe that the estimated value of knots/meter is stable with the yarn speed, as expected, since we are sensing the same yarn (already interlaced), just with a change in its running speed. Also the relative width of the frequency distribution remains almost constant with the yarn speed, since the same yarn is characterized also by the same pattern of irregularities.

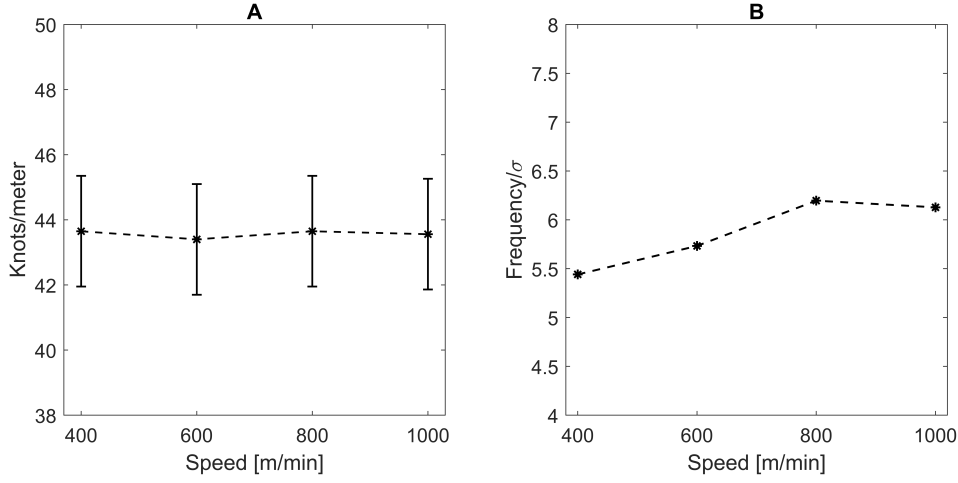


Figure 5.12: Key parameters obtained from the Gaussian fit for different yarn speed values: knots/meter (A) and relative width of the distribution (B).

### 5.3.2 Sources of noise

Once verified that the frequency component is actually related to the yarn profile modulation, we focused our attention on the noise affecting the measurement. The signal in time acquired with the photodiode indicates a low frequency oscillation, superimposed to the faster modulation given by the alternation knots-not interlaced segments (Fig.5.13, A). The corresponding FFT indicates that this component is peaked around 33 Hz (Fig.5.13, B). Additionally, we observe a baseline signal that increases for lower frequency values. Previous studies attributed the low frequency contributions to the yarn rotation [40].

We asked ourselves which are, in our case, the reasons laying behind the baseline noise and the 33 Hz component. One source of noise could be the **external illumination** or variation in the light intensity caused by the motion of objects nearby the sensor.

In addition, a contribution to the noise is given by the **irregularly shaped yarn profile** and by the **yarn oscillation**. As a matter of facts, the LED source, widened by means of a divergent lens, does not result in parallel rays hitting the yarn. As already discussed in Sec.5.2.2 this fact causes a 3 % signal modulation for an oscillation of the yarn of 1 mm. Those observations let us hypothesize that the 33 Hz component is caused by the yarn oscillation. Otherwise, it could be caused by a periodic irregularity in the yarn profile (for example due to surface filaments), that adds to the modulation caused by interlacing.

We investigated further these hypotheses by means of a high speed camera and

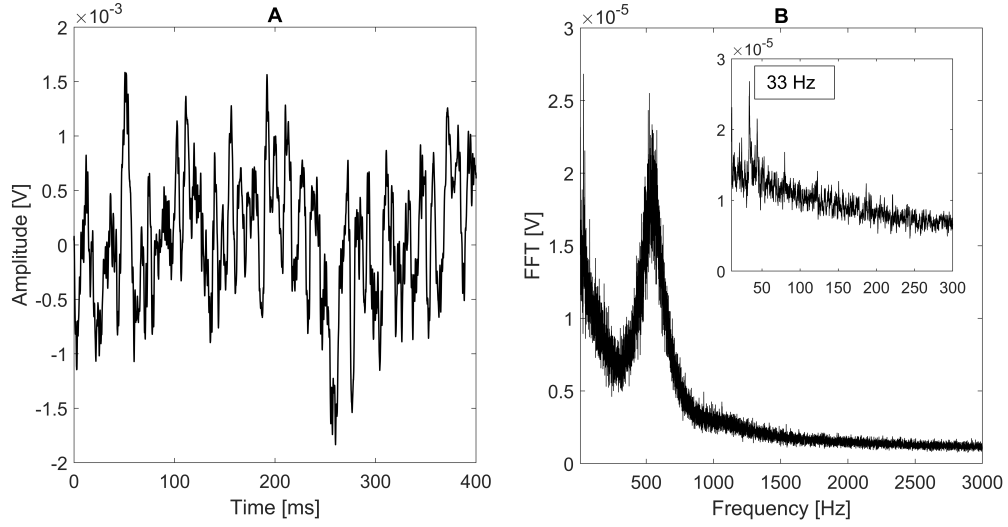


Figure 5.13: Signal acquired with the photodiode, showing high and low frequency modulations (A). Corresponding FFT, with a zoom in the low frequency range (B).

a position sensitive detector. With the **high speed video**, we observed the yarn oscillation in the direction between the sensor plane and the LED. From each frame we extracted the position of the yarn and its diameter.

Monitoring the yarn width over time, we observe an increase of the FFT signal for low frequency values (Fig.5.14 A, B). So, the background components detected with the photodiode are partially caused by the irregular yarn shape. The yarn position over time of Fig.5.14 (C, D) indicates that the yarn oscillates at the same frequency (33 Hz) detected by the photodiode (Fig.5.13, B).

To further investigate the possibility that the background noise is caused by an external light disturbance, we decided to employ a different illumination system, using an infrared LED (emission peaked around 836 nm). In this way, we can isolate the light modulation caused by the yarn from the other external contributions. For this purpose, we need to use a photodiode with a spectral response range centered in the infrared region. In addition, we are interested in monitoring the yarn oscillation also in the photodiode plane. Indeed, this oscillation could be a source of background noise, due to more likely changes in the yarn profile during the oscillatory and rotational motion. To reach both these purposes, we decided to use a **position sensitive detector**, with a spectral response range from 760 to 1100 nm (S5629-02 Hamamatsu). We performed a simultaneous measurement using both sensors and the resulting spectra are reported in Fig.5.15. In Sec.5.1.3 was explained that the difference of the two IR channels is sensitive to the yarn position. The FFT of the difference indicates a low frequency contribution (up to about 140 Hz) caused by the yarn

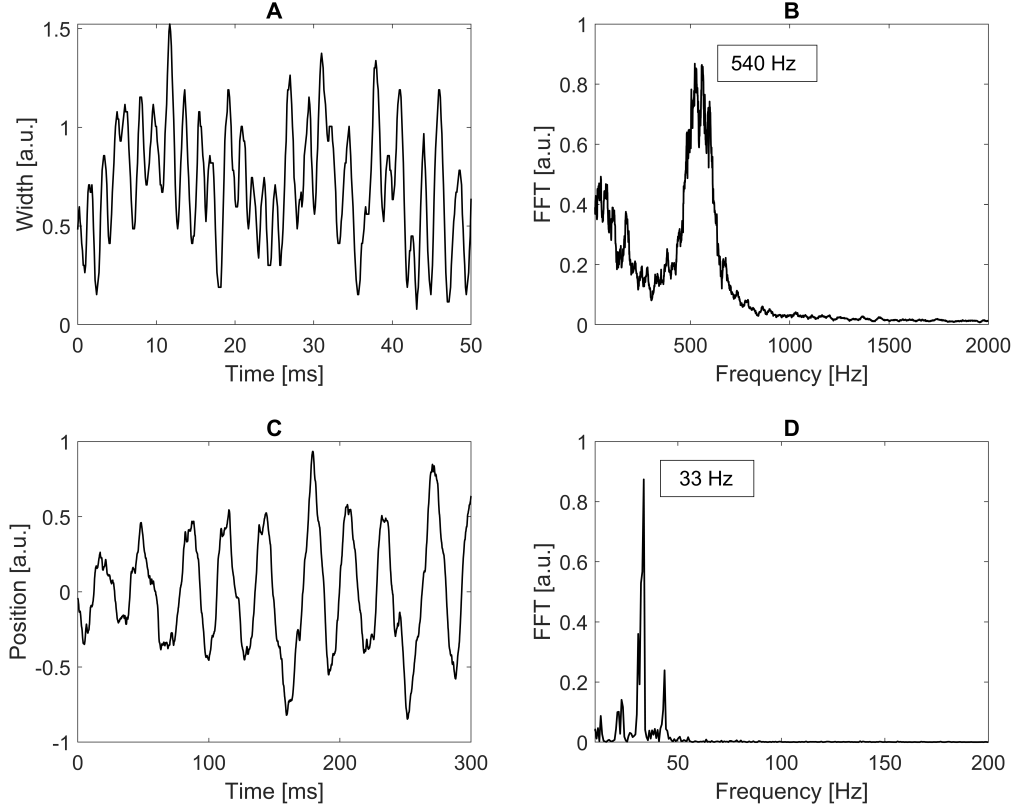


Figure 5.14: High speed video analysis of the yarn motion; width of the yarn over time (A), FFT of the width of the yarn (B), motion of the yarn around its mean position (C), FFT of the position of the yarn over time (D).

oscillation in the sensor plane (Fig.5.15, A). These components are less marked in the spectrum given by the sum of the two channels, as an indication that they are caused by the yarn oscillation. If we compare the spectrum given by the sum of the two channels of the IR sensor with that obtained with the green LED, we observe a similar response, also in the low frequency range (Fig.5.15, B), indicating that the external lighting gives a small contribution to the background noise. However, the main causes of disturbance can be attributed to the yarn oscillation, to its random motion and to its irregular profile. For this reason, the stability of the yarn needs to be improved as much as possible.

### 5.3.3 Evaluation of the mean distance between knots

So far, we have demonstrated that the photodiode is sensitive to the yarn diameter variations caused by interlacing. The center of the frequency distri-

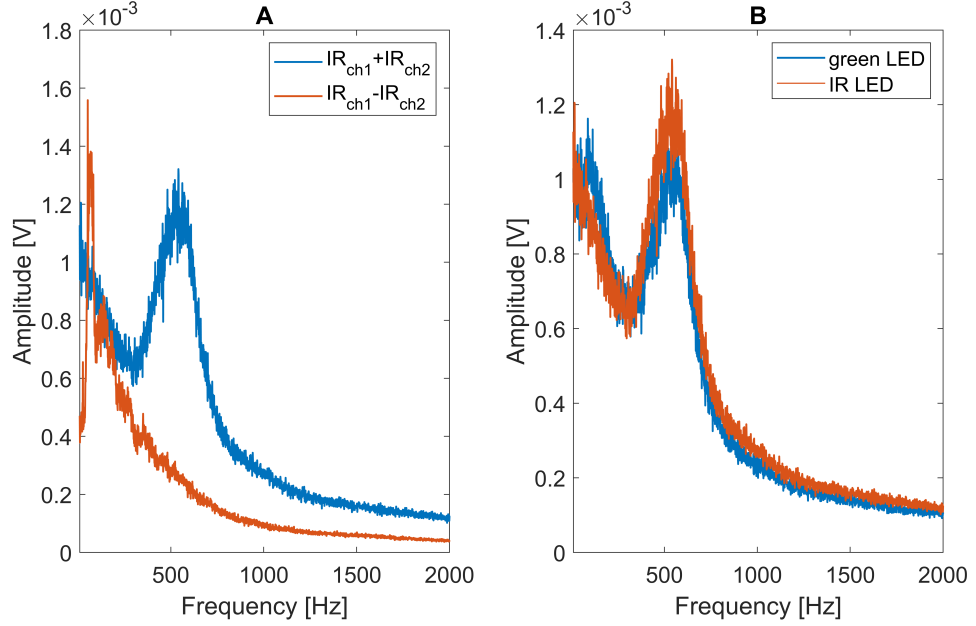


Figure 5.15: Frequency spectra obtained with a 800 m/min running yarn; comparison of the sum and difference of the two channels of the position sensitive detector (A), comparison of the spectra of the IR position sensitive detector (sum of two channels) and the visible detector (B).

bution gives an estimate of the mean knots distance, while the width contains the information on the regularity of the process. Two issues are related to this statistical, mean analysis.

- We are estimating the most frequent distance between knots over at least tens of meters of yarn, but we do not have any information about occurrence of not interlaced segments.
- We are counting all constrictions in the yarn as knots, while actually some knots are too weak to be considered.

In the company, when the quality control laboratory measures the mean knots distance on the already interlaced yarn, it fixes a threshold above which a constriction is considered a knot, while below it is evaluated as too weak to be counted. For this reason, we should predict more knots per meter with respect to the company.

To verify this result, we decided to detect with the photodiode a yarn that is later analyzed by the company quality control laboratory.

We performed long measurements (5 min), repeated four times during the same yarn production lot to evaluate also the stability of the sensor (about 2 hours

interval from one measurement to the following one). When the machine is turned on, the photodiode is continuously exposed to mechanical vibrations and other external noise sources. The measurements have been performed for 6 days, considering 6 different yarn production lots (variation of yarn linear density, yarn speed employed for the production, number of filaments forming the final yarn). Here, just two measurements will be analyzed and compared. The first one (called **lot A**) has been performed on a yarn with a speed of 1000 m/min, 2700 dtex density and 128 filaments. The second (called **lot B**) is a yarn produced with a speed of 700 m/min, with 3000 dtex density and 126 filaments.

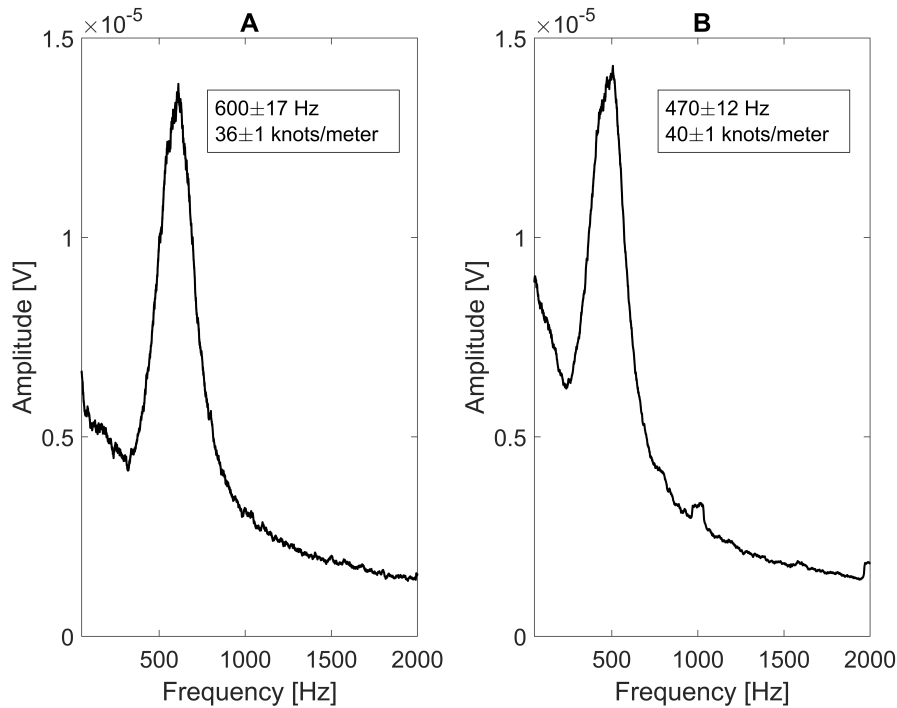


Figure 5.16: Frequency spectra of the signal acquired with the visible photodiode: yarn of lot A (A), yarn of lot B (B) with predicted values of knots/meter.

In Fig.5.16 are reported the frequency spectra in the two cases and the knots per meter estimated from the central frequency of the distribution. This value of knots/meter needs to be compared with the one given by the quality control laboratory. In this case, the knots per meter are determined using the capacitive knot-counting device described previously (Sec.1.1.3, entanglement testing). A brief recap: a cantilever beam, constituting one plate of a capacitor, is leaned against the yarn and moves following its profile. In this way, since the knots are thicker than the not interlaced segments, the signal is propor-



tional to the strength of the knots as shown in Fig.5.17. The company quality control fixes a threshold above which the interlacing is strong enough to be considered a knot. The choice of the threshold is based on the value of knots per meter that the company normally has experienced, with that particular type of yarn, processed in that specific way. It is an arbitrary threshold based on the company experience.

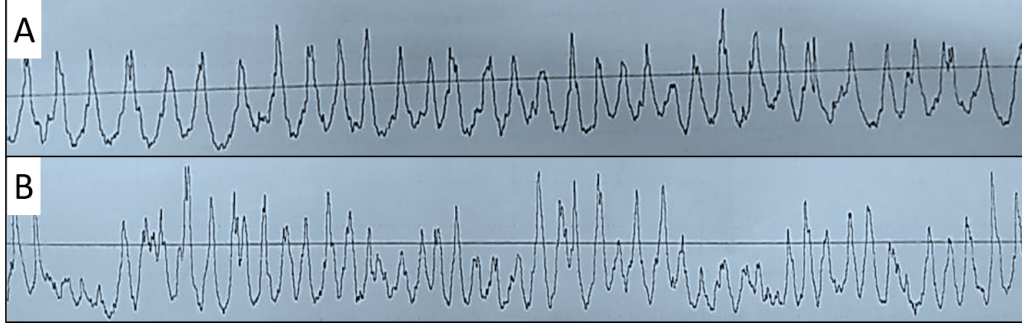


Figure 5.17: Data recorded with the capacitive knots-counting machine of the quality control laboratory on lots A and B, resulting in 35 knots/meter and 36 knots/meter, respectively.

The quality control laboratory measures 35 knots/meter for lot A and 36 knots/meter for lot B. Comparing this result with Fig.5.16, we observe that the photodiode analysis predicts the knots per meter in the case of lot A, while in case of lot B the value is overestimated. This fact can be easily explained considering that, in case A, the profile of Fig.5.17 is regular and almost all peaks are considered as knots, while in case B we observe more not-interlaced segments or weaker knots (under threshold). These irregular regions are counted by the photodiode analysis, but excluded by the quality control. This is the reason why we overestimate the value of knots per meter in the second case, since we are counting as knot each oscillation in the photodiode signal. In other words, the difference between the predicted and the actual value of knots per meter gives a hint of the regularity of the process.

To sum up, this analysis allowed us to explain why and to which extent the interlacing frequency estimated from the FFT of the photodiode data exceeds the real value.

#### 5.3.4 Reconstruction of the yarn profile from the time signal

We aim to develop a technique that monitors the knots distance and that accounts for the irregularities in the interlacing process, during the yarn production. We want to analyze the yarn profile in time, knot by knot, moving towards a punctual analysis of the knots distance. We need to know if each

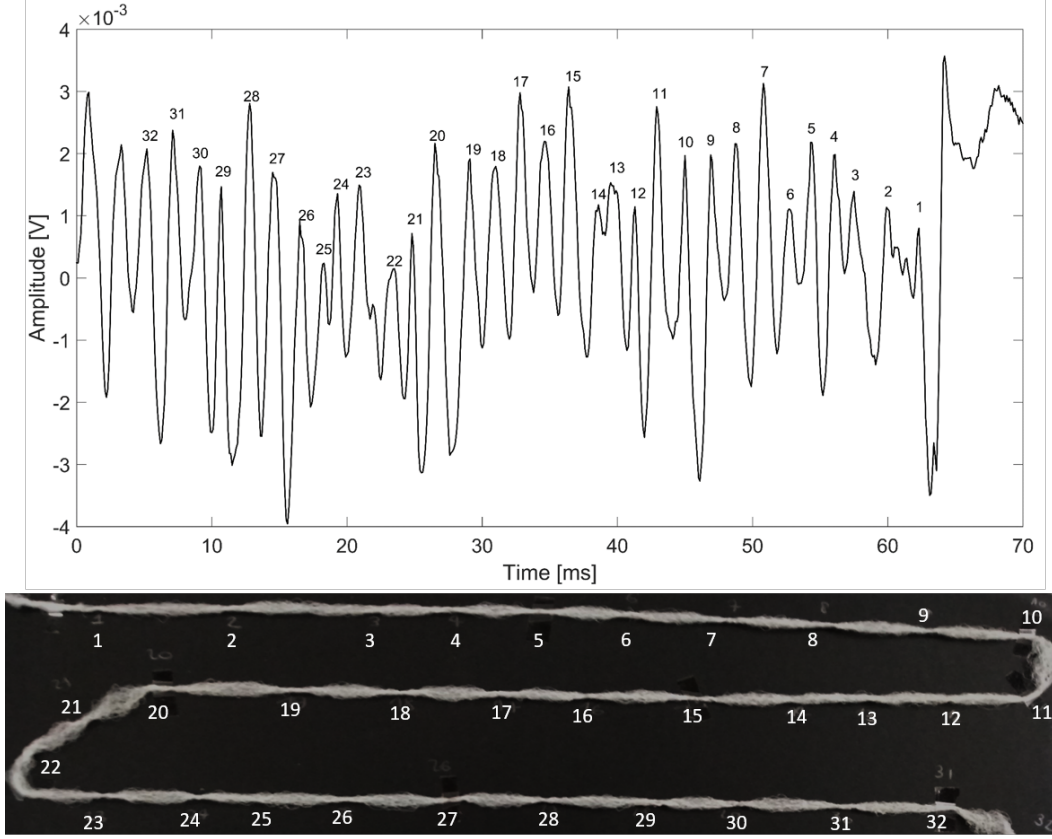


Figure 5.18: Top: signal in time with the peaks enumeration. Bottom: corresponding yarn section with a numeric index for each knot.

peak in the time signal acquired with the photodiode (reported for example in Fig.5.13) is caused by a knot.

To understand this behavior, we **compared the time signal to the corresponding yarn segment**. We managed in the comparison, considering an interlaced yarn that ends into a parallel one; in this way we have a marker that allows us to backtrack which part of the yarn corresponds to a selected time signal. In Fig.5.18 are reported both the signal in time and the image of the corresponding yarn segment. The enumeration of the peaks in the time signal compared to the knots on the yarn (Fig.5.18), suggests a good agreement. If we take for example the distance between knot 1 and 2 (we call it  $d_{1,2}$ ) and  $d_{2,3}$ , it is bigger than  $d_{3,4}$  and  $d_{4,5}$ . The same behavior is observable also in the time signal. This is just an example to show the correspondence between the distance observed on the yarn and the one predicted from the time signal. Since the time signal acquired with the photodiode is related to the yarn profile, we are also interested to estimate the actual **yarn diameter** over time.

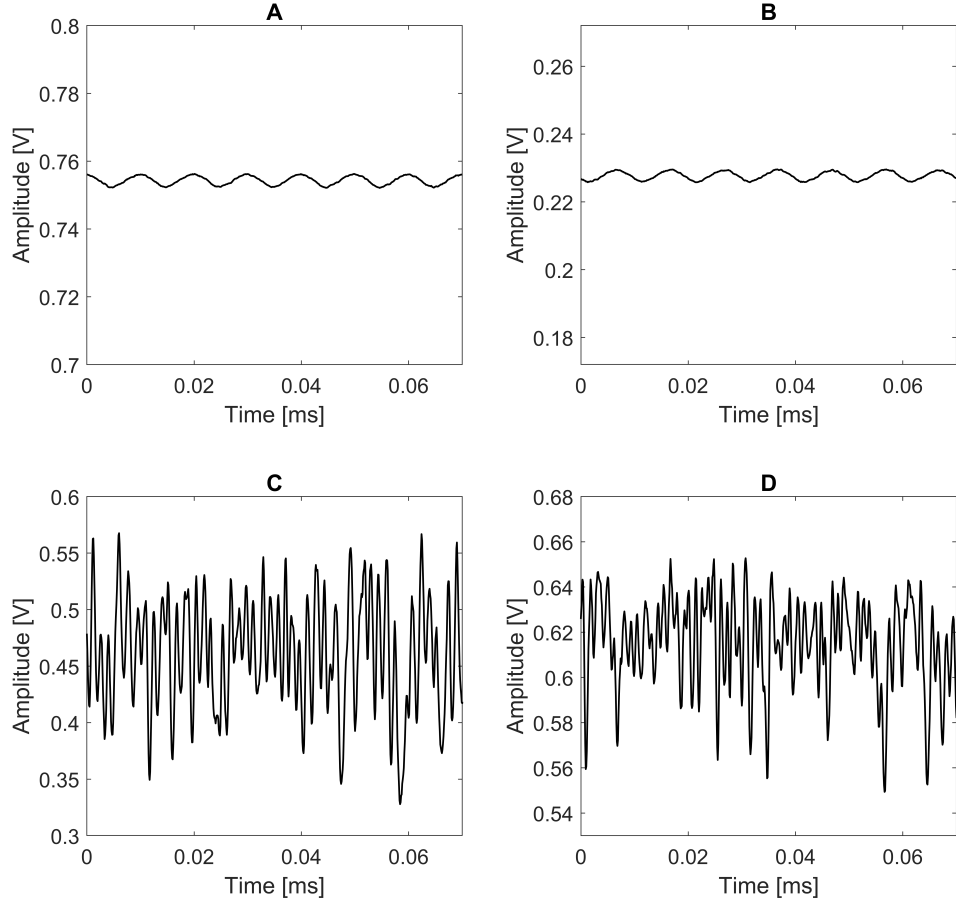


Figure 5.19: Time signal recorded in different configurations. Illumination of the photodiode by the external and LED light (A), triple end yarn placed in front of the photodiode (B), triple end yarn running with a speed of 1000 m/min (C), single end yarn running at 1000 m/min (D). A different range for the y-axis is chosen intentionally, to observe the extent of signal (diameter) modulation, besides its mean value.

We considered a mean value of the slopes obtained for the sensor calibration ( $-0.4 A_{norm}/\text{mm}$ ), reported in Fig.5.9 (D), to calculate the yarn diameter over time. For this analysis, data were acquired in DC coupling mode, to know the absolute voltage value. In Fig.5.19 (A) is reported the baseline signal, when the photodiode is not shadowed by the yarn, the LED is switched on and also the external light is collected by the sensor (that causes the 100 Hz signal oscillation observed). The mean signal, of 0.75 V, is the normalization factor (explained in Sec.5.2.2). Then, we placed the yarn, still in front of the photodi-

ode (Fig.5.19, B), the mean signal was of 0.23 V, that corresponds to a diameter of about 1.7 mm. When the same yarn is running with a speed of 1000 m/min (Fig.5.19, C), the tension is higher and the diameter is consequently smaller (it is oscillating from 0.7 mm to 1.1 mm). As a further confirmation, we also analyzed the signal modulation caused by a thinner yarn (single end yarn, see Sec.1.1.3) and in this case the diameter oscillates between 0.4 mm and 0.6 mm (Fig.5.19, D).

In addition to a distance information, we observe in Fig.5.18 that we have also an insight into the **shape and strength of the knots**. Stronger knots, such as knots 7, 19, 26, 29, cause a sharp and well-defined peak in time, while for looser knots, like 13, 22, 25, the peaks are broader and less defined. With stronger knots we mean the cohesion points characterized by a higher contrast between open and interlaced diameter.

This result is encouraging towards a punctual analysis of the data acquired with the photodiode. We aim to highlight the irregular patterns in the signal in order to exclude the weak knots from the counting process. In this way, we should reproduce the result obtained by the quality control laboratory.

## 5.4 Signal processing to detect irregular patterns

Each peak in the time signal corresponds to a modulation in the yarn profile. So, counting the number of peaks we can easily determine the interlacing frequency. Additionally, we can evaluate only the significant peaks fixing a threshold on the signal amplitude. In this way, we can exclude the weaker knots and the irregularities.

However, looking at the time signal of Fig.5.18, we observe that this approach is complicated by the low frequency oscillation of the time signal. We already investigated the causes of those low frequency components and we identified the yarn oscillation as a probable reason.

So, we decided to filter the data with a high pass minimum-order filter with a stopband attenuation of 60 dB (highpass function implemented in MATLAB), cutting away the frequency components below 100 Hz, as shown in Fig.5.20, where we can observe that the filter preserves the same signal amplitude for the frequency values above 100 Hz, while it cuts the lower components.

In Fig.5.21 we observe a comparison of the time signal before (A) and after (B) filtering. As expected, the filtering procedure reduces the low frequency oscillations that prevents us from using a fixed threshold.

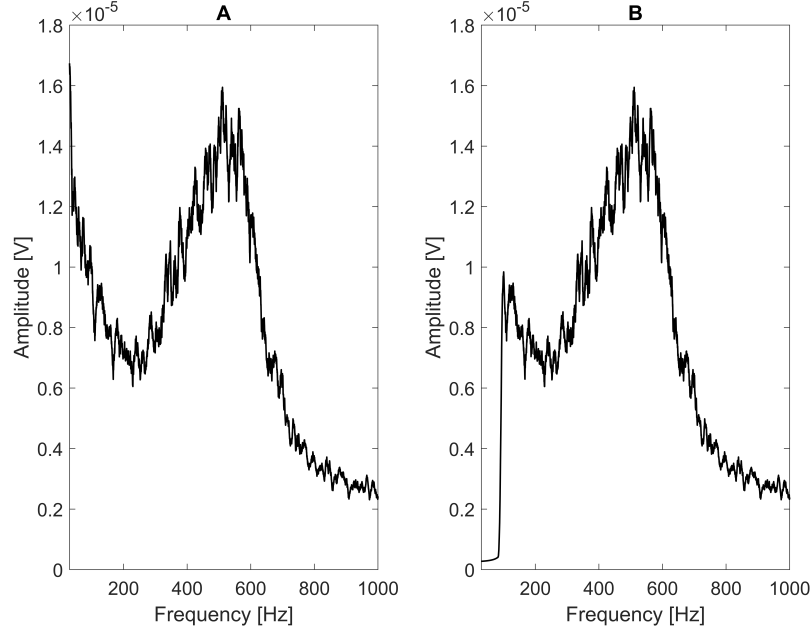


Figure 5.20: FFT of the original signal (A), FFT of the high-pass filtered signal, with a 100 Hz cutoff frequency (B).

#### 5.4.1 Threshold proportional to the signal amplitude

In Fig.5.21 (A) a threshold proportional to the RMS of the signal is considered. However, we observe that we are considering under threshold and hence we are missing regions with regular and sharp peaks, without counting them as knots. On the other hand, filtering the signal (Fig.5.21, B), the mean value is more stable and the **fixed threshold** is more significant in determining the regular regions. However, we observe that besides the baseline signal oscillation we have also an amplitude modulation, probably caused in turn by the yarn oscillation in the photodiode plane. For this reason, we decided to fix a threshold, from time to time proportional to the signal RMS (Fig.5.21, C), over about 5 periods of signal oscillation. We will call  $c_{thr}$  the constant of proportionality. With this **mobile threshold approach**, we count more effectively the regular peaks. However, we observe that also in this case we are occasionally missing some regular patterns.

To verify the validity of this method, we analyzed the time signal of the **lot A** and **lot B** using the procedure just described. We fixed a mobile threshold and counted as knots all the peaks that exceed that amplitude value. From the time difference between the peaks and knowing the yarn speed, we could easily establish the spatial distance between knots.

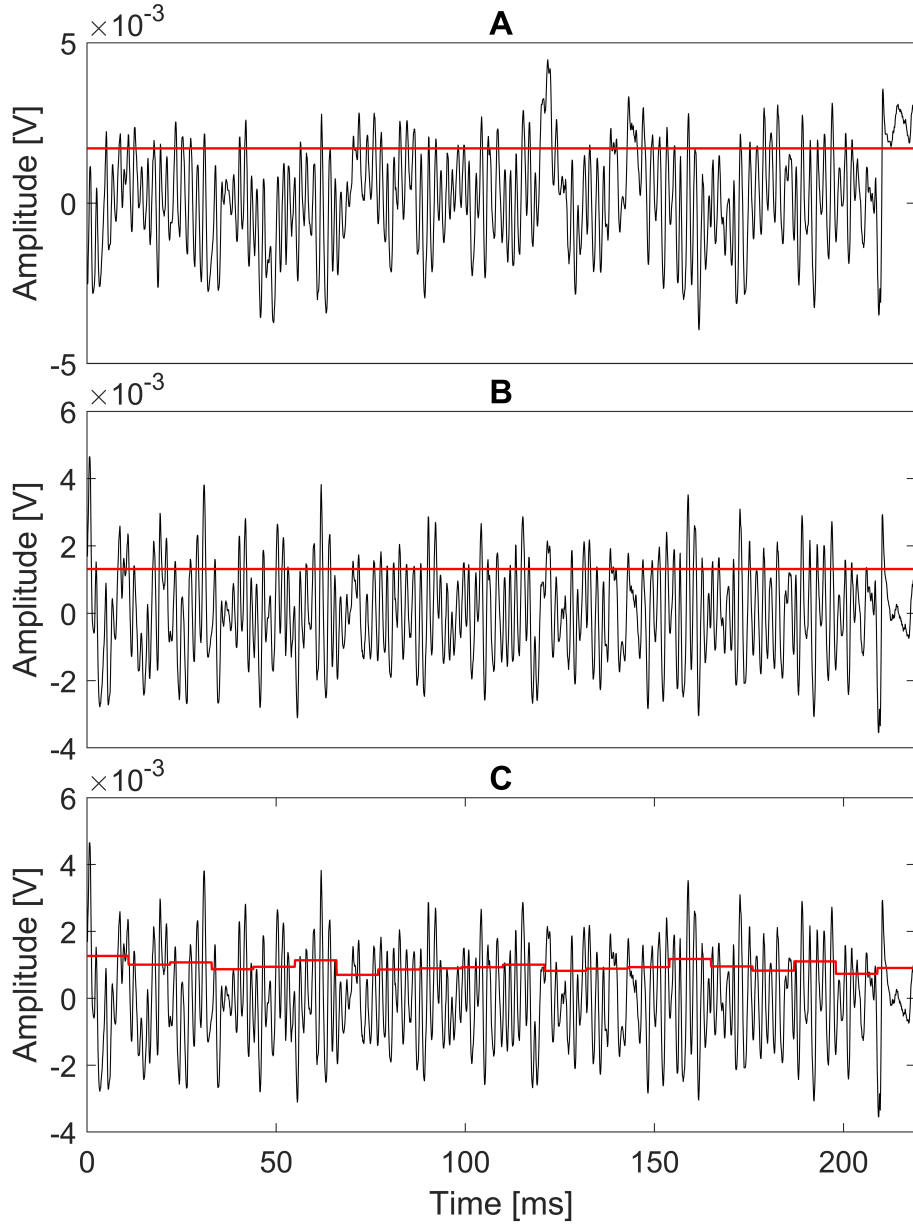


Figure 5.21: Original time signal (black) with a threshold given by its RMS (red)(A); filtered time signal with a RMS threshold (B); filtered signal with a mobile threshold proportional to the RMS of 5 signal periods (C).

Then, we fixed  $c_{thr}$  to obtain the same value of knots/meter established by the quality control laboratory of the company.

In particular, for lot A with  $c_{thr} = 0.9$  we calculate 35 knots/meter and for lot B with  $c_{thr} = 1.02$  we estimate 36 knots/meter. Fixed  $c_{thr}$  for a type of

yarn in the way just described, we asked ourselves if this analysis gives **reproducible results** on repeated measurements performed on the same yarn production. Analyzing the repeated measurements also on different lots, using the same  $c_{thr}$  value, we found a good reproducibility, within a variation of one knots/meter in the estimated value. This result indicates that, once fixed the threshold, we can perform the time analysis on-line, to evaluate the regularity and the stability of the yarn over time. However, the method described so far is quite artificial, both in the choice of the  $c_{thr}$  value and in the mobile threshold approach.

The main target of our sensing technique is to point out the irregularities in the yarn, such as not interlaced regions, variations of periodicity or weak knots. This justifies our interest in improving further our analysis, processing data in order to highlight the irregular sections of the time signal.

#### 5.4.2 Cross-correlation analysis

##### Correlation with a regular signal segment

The irregularities in a signal can be pointed out comparing it with a regular sample. We extracted a **regular time pattern** from the time signal, such as the 5-periods oscillations of Fig.5.22 (A, B). We compare this "probe" to the original signal (part of the original time signal is shown in Fig.5.22, C), shifting each time the probe of one acquisition period (in our case the lag was  $10^{-4}$  s). We performed the same analysis with samples of different length, but in the end we chose the probe with 5 oscillations as it is effective in the detection of irregular patterns of the order of 5 periods (or higher). The extent of the correlation amplitude modulation of a 5-periods probe with a signal showing different periods defects will be discussed and reported in Fig.5.31.

In other words, we are performing the cross-correlation of two discrete-time sequences,  $x$  and  $y$ . As a matter of facts, the cross-correlation  $C_{xy}$  measures the similarity between  $x$  and shifted (lagged) copies of  $y$  as a function of the lag as:

$$C_{xy}(m) = \sum_{n=0}^{N-m-1} x_{n+m} y_n^* \quad (5.3)$$

Since in our case  $x$  and  $y$  have different sizes, we appended zeros at the end of the probe, until the same length is reached. The cross correlations between the signal and the two probes (performed with a custom MATLAB function) are reported in Fig.5.23.

A comparison with the original signal of Fig.5.22 (C) indicates that a lower cross correlation corresponds to an irregular signal pattern. The higher the irregularity, the lower the cross correlation.

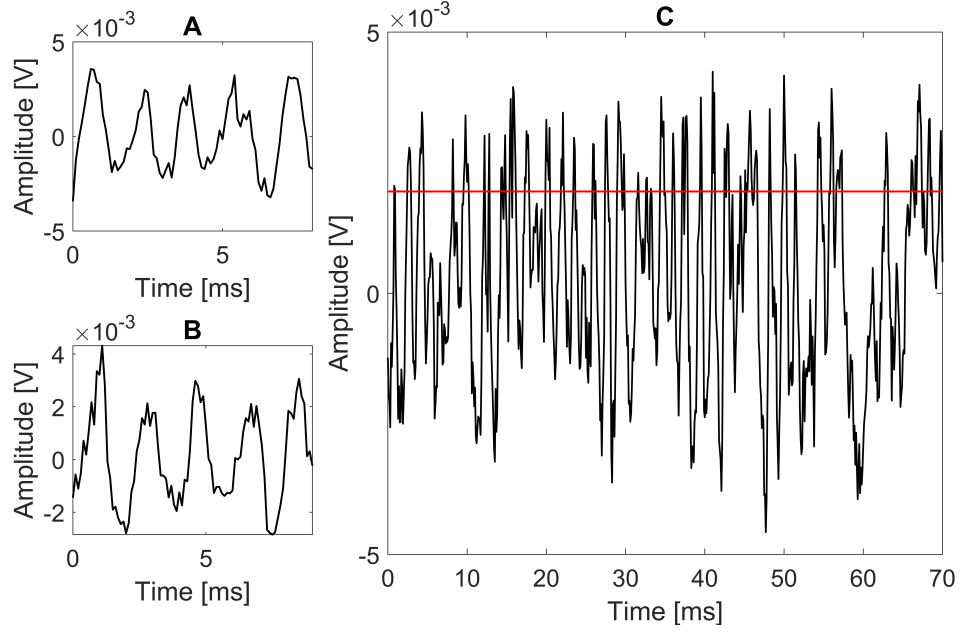


Figure 5.22: Regular 5-periods time segment (A), (B), extracted from the original photodiode time signal (C); in red the RMS of the signal amplitude.

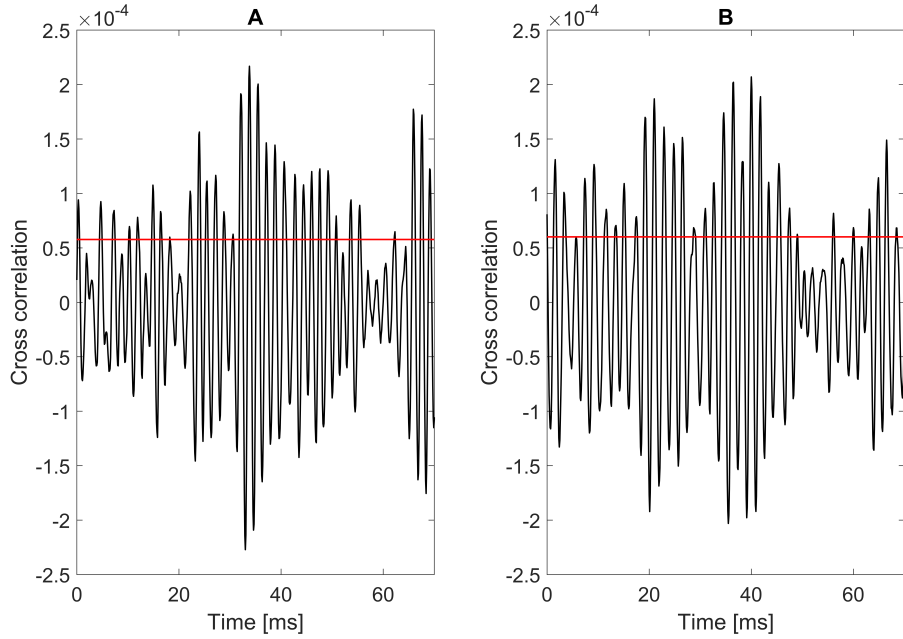


Figure 5.23: Cross correlation with probe A of Fig. 5.22 (A), and with probe B (B); in red the RMS of the cross correlation.



However, the result depends on the particular shape of the probe we are considering. Indeed, the probes A and B have different features both in terms of frequency and shape of the peaks.

Hence, also the cross correlation highlights different irregular patterns, as results from the comparison of Fig.5.23 (A) and (B).

#### Correlation with a Gaussian wave packet

For the limitations just described, we need to find a more general probe, that contains all the frequency components of the original signal and with a regular shape of the peaks.

For this purpose, we consider the FFT of the original signal and fit it with a Gaussian, as shown in Fig.5.24 (A). The inverse Fourier transform of the Gaussian is a signal in time, with a regular shape, that contains all the frequency components of the original signal. For this reason, we decided to use this **normalized Gaussian wave packet** (Fig.5.24, B) as the probe that will be correlated with the original time signal. The Gaussian profile ensures also a reduction of the spectral leakages effects with respect to the previous probe. As a matter of facts, the correlation in time corresponds to a conjugate product in the frequency domain. In the previous case, selecting a 5-periods section of the original signal, we applied a rectangular window to the time sequence, characterized by multiple side lobes in the frequency domain.

The cross correlation between the Gaussian probe and the time signal is shown in Fig.5.25 (B). Comparing this result with the original signal (Fig.5.25, A), we observe that we are effectively detecting the irregular patterns.

**RMS-based threshold** Since the correlation amplitude is proportional to the signal regularity, it is easier to use a fixed threshold to count the number of knots and irregular regions. To validate this method, we need to compare the knots per meter evaluated with the mobile threshold described previously with those obtained using a fixed threshold on the cross correlation. We analyzed the long, repeated measurements performed on the yarn that was checked also by the quality control laboratory (lot A and B of Fig.5.17, described in Sec.5.3.3). Fig.5.26 shows the comparison of the two approaches.

The thresholds have been chosen proportional to the RMS value of the signal, but with a proportionality constant  $c_{th}$  that allows to obtain the same knots per meter as the quality control laboratory ( $c_{th} = 0.3$  for lot A and  $c_{th} = 0.6$  for lot B).

The cross correlation analysis highlights that lot A (Fig.5.26, B) is more regular than lot B (Fig.5.26, D), since more peaks are below threshold in the small signal segment shown in the figure. Again, we observe that the cross correlation

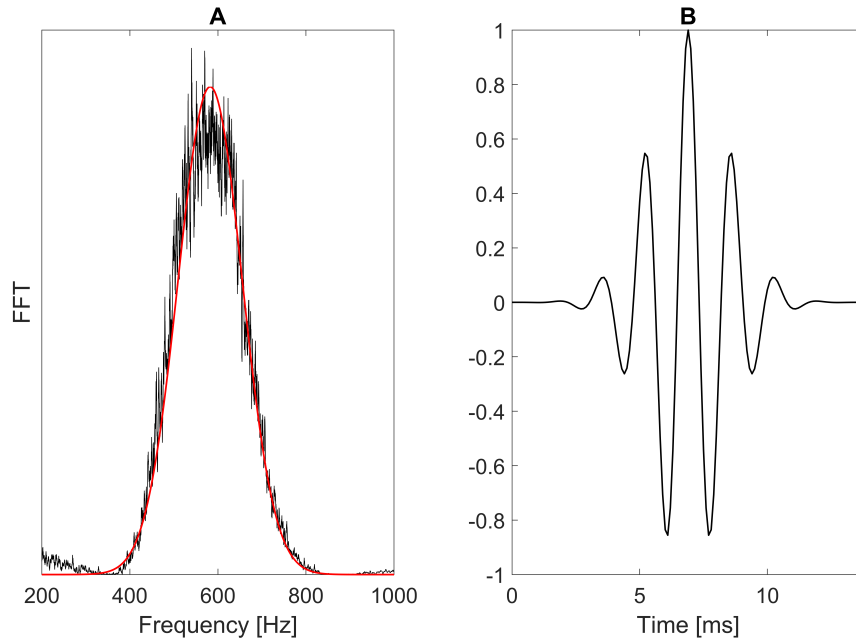


Figure 5.24: FFT of the original signal with a Gaussian fit (red)(A); normalized inverse FFT, resulting in a Gaussian wave packet (B).

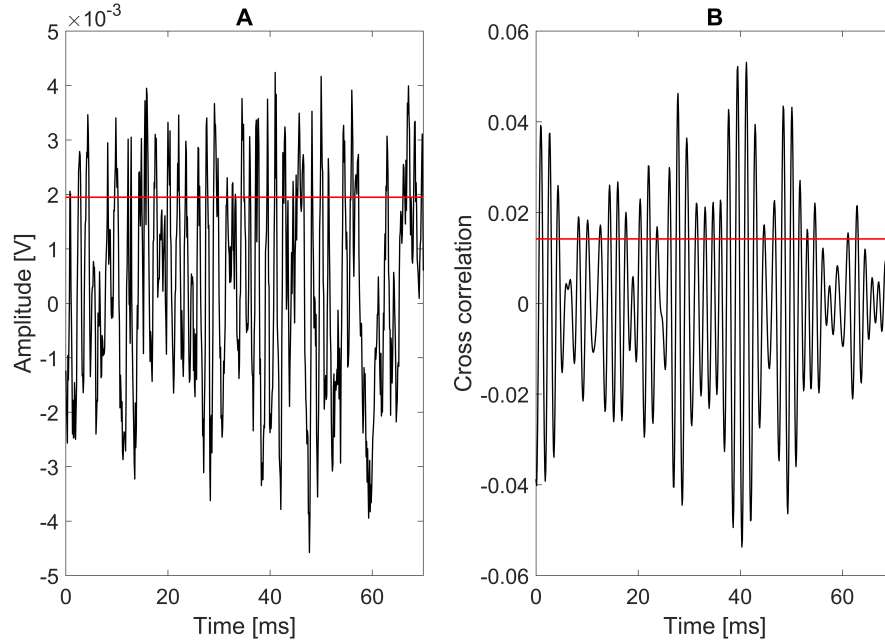


Figure 5.25: Original time signal (A); cross correlation with the Gaussian probe (B). In red is reported the rms of the signal.

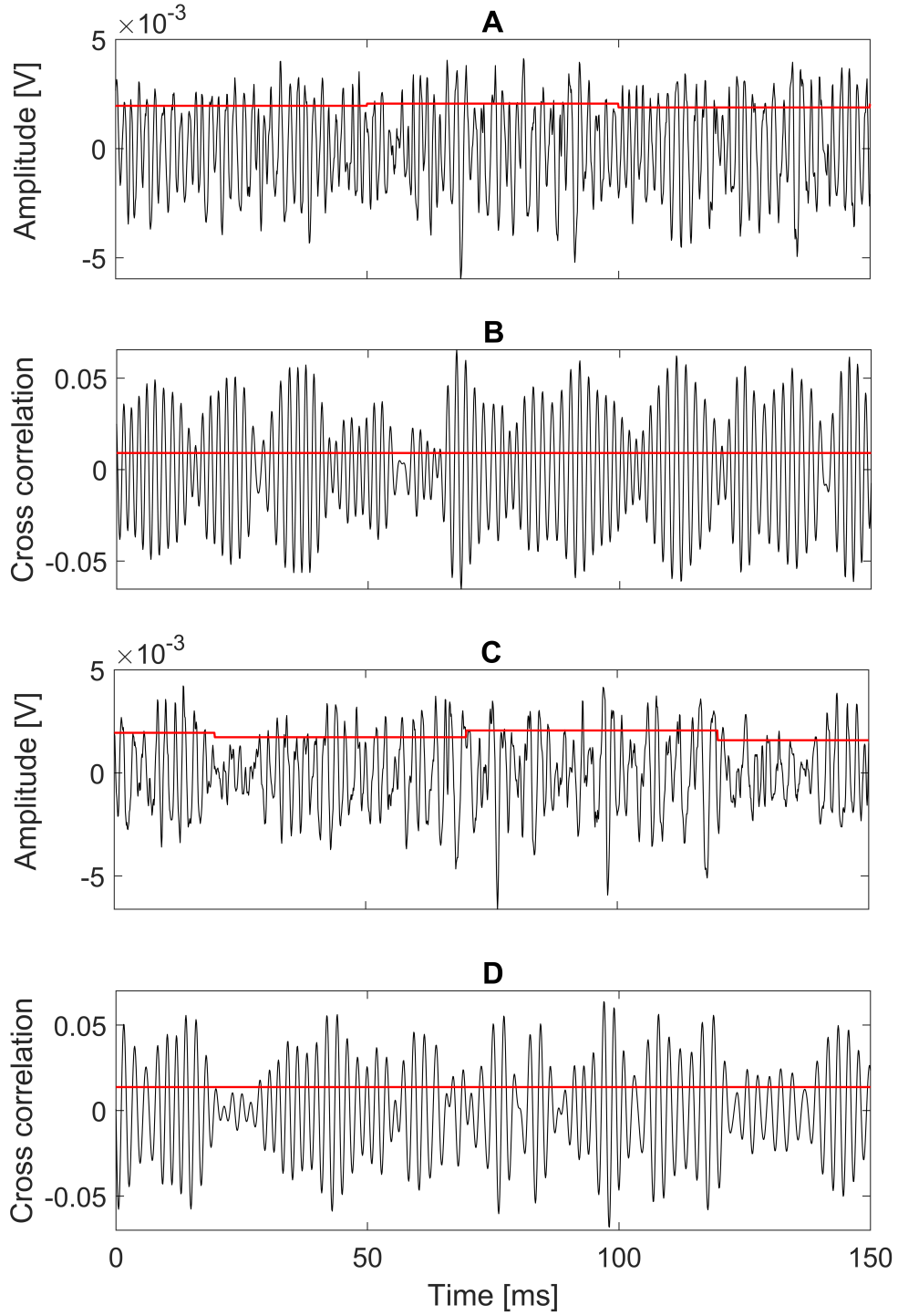


Figure 5.26: Original signal in time with a threshold proportional to the rms,  $c_{th} = 0.9$  for lot A (A),  $c_{th} = 1.02$  for lot B (C), corresponding cross correlation with the Gaussian probe,  $c_{th} = 0.3$  for lot A (B),  $c_{th} = 0.6$  for lot B (D).

is more effective in highlighting the irregularities in the time signal and this allows us to analyze also the frequency of occurrence of a particular defect. We can consider for example the number of consecutive knots that are under threshold. In this way, we estimate the length of an irregular segment and we know how often one or more knots are missing. If we count the occurrence of each defect, we have an estimate of the overall regularity of the process.

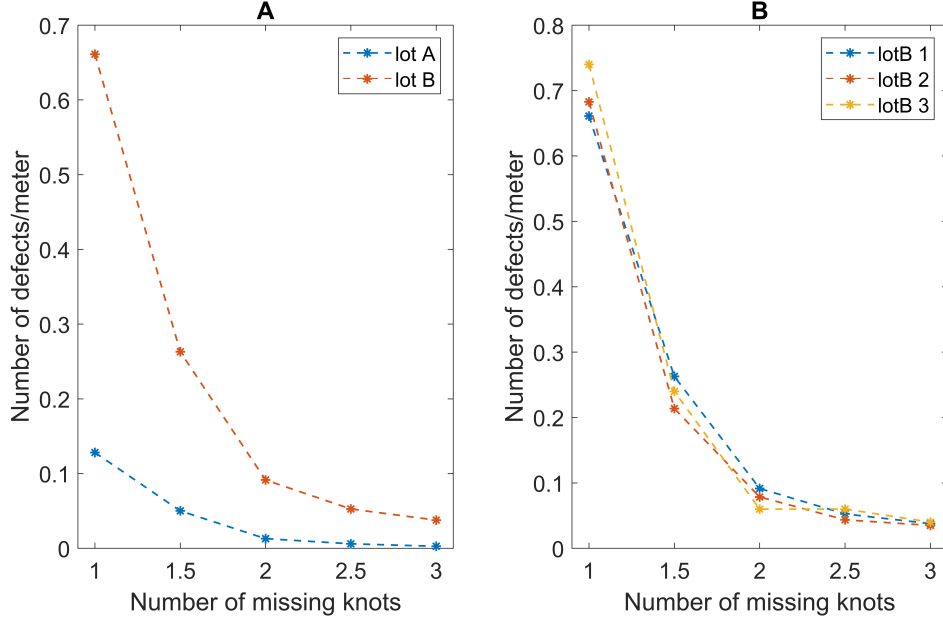


Figure 5.27: Number of defects per meter of yarn as a function of the length of the defect. Comparison between two different lots (A). Comparison of repeated measurements on the same lot B (B).

In Fig.5.27 (A) we observe a comparison of the regularity of lot A and lot B in terms of number of defects per meter of yarn. As expected, the frequency of occurrence of a defect is about 5 times higher for lot B than for lot A. In addition, we observe that the value decreases with the length of the defect. We tested also the regularity of the same lot (lot B) during the yarn production. In other words, we performed the analysis of the yarn regularity on the data acquired in different times during the production of the same lot. Fig.5.27 (B) shows a good agreement of the results and this indicates a stability in the yarn production conditions.

**Threshold based on the correlation with a parallel yarn** So far, we fixed a threshold that is still dependent on the arbitrary value of  $c_{th}$ , chosen in a way that the calculated value of knots per meter equals the one measured by

the quality control laboratory of the company. We would prefer to perform a more rigorous and general analysis.

Additionally, fixing a threshold proportional to the RMS value of the cross correlation, we consider also the random fluctuations given by a not-correlated signal. To better explain this point, we take two signals acquired with the photodiode, given by an interlaced and a parallel yarn running with a speed of 1000 m/min. The spectrum of the interlaced yarn exhibits a characteristic frequency of 680 Hz, while the parallel yarn shows an almost flat and not structured spectrum in that frequency range (Fig.5.28, A). This means that, for the interlaced yarn we are expecting to count knots with a frequency of 680 Hz (about 40 knots/meter), while in the parallel yarn no knot should be counted. We used the counting procedure described previously, using the cross correlation method. We correlated both signals in time with the Gaussian wave packet centered around 680 Hz shown in Fig.5.28 (B).

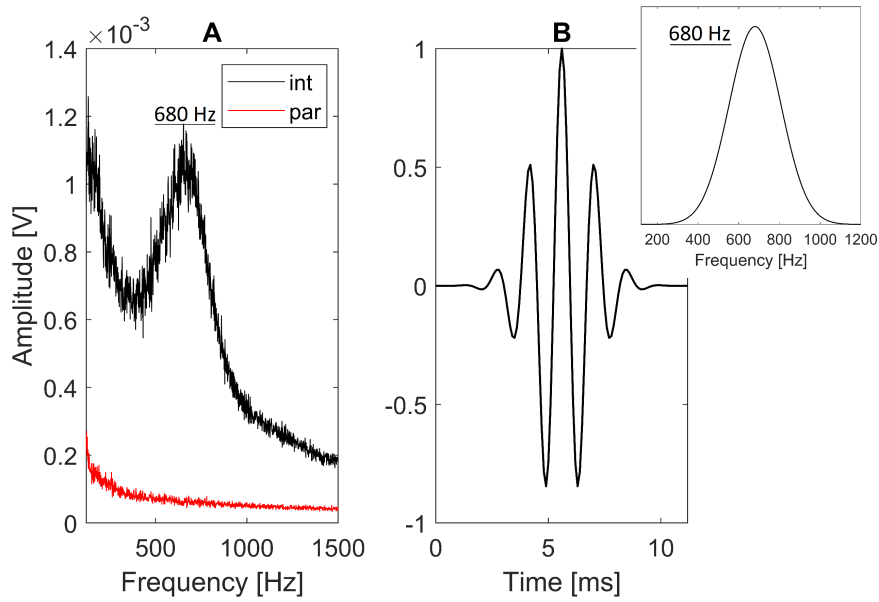


Figure 5.28: Spectra of an interlaced (black) and parallel (red) yarn running at 1000 m/min (A). Gaussian wave packet correlated with the interlaced and parallel yarn time signals, with an insight into its frequency spectrum (B).

In Fig.5.29 (A, B) are shown the results in both cases. If we fix a threshold proportional to the RMS of the correlation ( $c_{th} = 0.4$ ), both for the interlaced and for the parallel signal, we count about 40 knots/meters in both cases and also the frequency of occurrence of the defects is the same (Fig.5.29, C). In other words, we are counting the same number of knots, also in a random signal given by the parallel yarn. Clearly, this is a bug in the way we decided

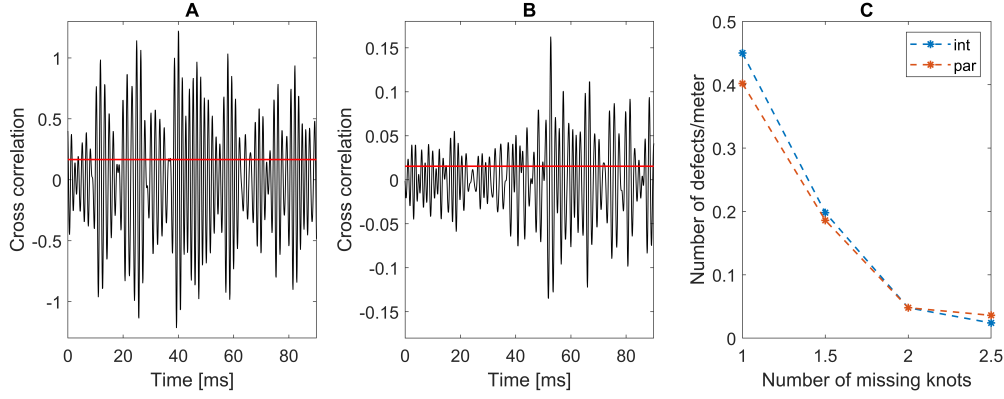


Figure 5.29: Cross correlation of a Gaussian wave packet with the signal given by a running (1000 m/min) interlaced yarn (A) and a running parallel yarn (B), in red is reported the threshold ( $RMS \cdot 0.4$ ). Comparison of the number of defects counted in each meter of yarn as a function of the defect length (C).

to fix the threshold.

Actually, the key difference clearly visible in Fig.5.29 (A, B) is the correlation amplitude, 10 times higher for the interlaced yarn with respect to the parallel yarn. This observation suggests us a further improvement in the analysis.

When one or more knots are missing, in that region the yarn is parallel. This means that the value of the cross correlation approximates the parallel yarn condition in case of missing knots. As a result, an accurate, general and strict threshold is given by the amplitude of the correlation of the Gaussian probe with a parallel yarn signal. In this way, we should count both knots and defects, excluding the random fluctuations in the signal.

The correlation with the parallel yarn shows the occurrence of peaks caused by electric disturbances. For this reason, instead of the maximum of the cross correlation, we considered four times its RMS value. Using this threshold, Fig.5.30 (B) indicates that just the spikes are counted in a parallel yarn, while the same threshold applied to the interlaced yarn allows to count knots.

With this approach, we count knots and defects only when the yarn is interlaced (Fig.5.30, C).

### Sources of cross correlation amplitude modulation

In order to further discuss and investigate the best way to fix a threshold value, we asked ourselves which are the causes of variation in the amplitude of the cross correlation. A reduction of the correlation could be given by missing knots or by a variation in the knots distance.

If we take the simplified case of a sinusoidal signal (to model our system),

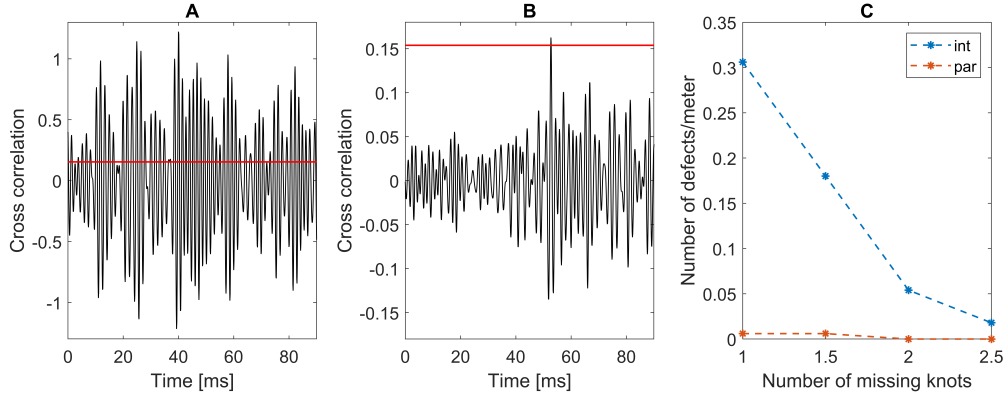


Figure 5.30: Cross correlation of a Gaussian wave packet with the signal given by a running (1000 m/min) interlaced yarn (A) and a running parallel yarn (B), the threshold in red is given by  $4 \cdot \text{RMS}$  of the parallel signal over the entire duration of the measurement (10 s). Comparison of the number of defects counted in each meter of yarn as a function of the defect length (C).

oscillating with a frequency of 680 Hz, a missing knot corresponds to a hole of one period in the signal, two periods-hole for two missing knots and so on, as shown in Fig.5.31 (A).

The cross correlation of this sinusoidal signal with the Gaussian wave packet, centered around 680 Hz (Fig.5.8, B) gives the result shown in Fig.5.31 (B). We observe that fixing a threshold proportional to the RMS of the signal, we detect different defects according to the value of the proportionality constant ( $c_{th}$ ). For example, if  $c_{th} = 0.07$  we detect only a 5-periods or longer defect, while if  $c_{th} = 0.3$ , 3 or more missing knots are detected.

Additionally, also a frequency and phase variation of the signal generates a decrease in the cross correlation (Fig.5.31, D), smaller than the one caused by the holes. In this case, a value of  $c_{th}$  higher than 0.65 allows to detect those defects. This is not a general result, since it depends on the extent of the phase and frequency variation, on the width of the Gaussian probe and on the combination of the three effects we have just mentioned. Our aim is just to highlight the main advantages and drawbacks regarding the employment of the cross correlation for the detection of missing knots. We understood that not only the absence of a knot is affecting the amplitude of the cross correlation, but also a phase or frequency variation. The best threshold needs to be chosen according to the particular defect we are interested to detect.

As a further investigation, it would be interesting to relate the type of defect predicted by the cross correlation with the corresponding yarn section.

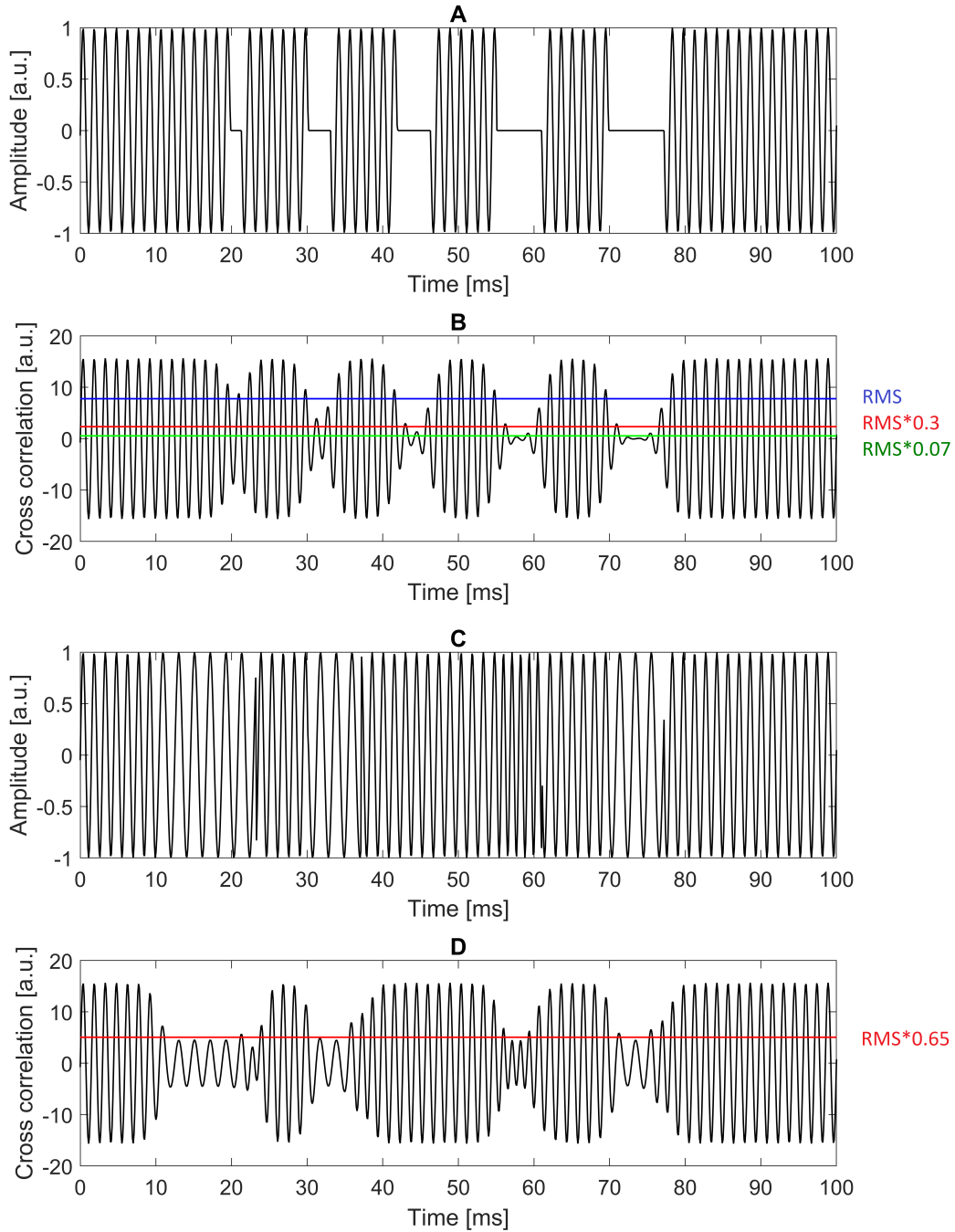


Figure 5.31: Sinusoidal signal, with a frequency of 680 Hz and with 1-5 periods holes (A); cross correlation of the sinusoidal signal with a Gaussian wave packet ( $f_0 = 680$  Hz,  $\sigma_f = 180$  Hz, in time  $\sigma_t = 5.6$  ms, Fig.5.8, B). Different threshold values are shown, RMS\*0.07 green, RMS\*0.3 red, RMS blue.

Sinusoidal signal, with a main frequency of 680 Hz, frequency and phase modulations (to 480 Hz and 880 Hz) (C); cross correlation with the Gaussian wave packet (D).

In red is reported the RMS\*0.65.



## 5.5 Comparison of the acoustic and optical approach

Thus far, we explored two different approaches to sense on-line the interlacing process. Now, we are interested in comparing the two techniques, analyzing pros and cons of those methods.

In dirty environments, where lubricating oils can be employed, a microphone is favored. However, this technique is sensitive also to the external noise, that adds to the small pressure fluctuations given by the yarn. On the other hand, the photodiode allows to evaluate the yarn regularity and its diameter over time, since the measurement is less affected by noise.

### 5.5.1 Simultaneous measurement of the mean interlacing frequency

Besides those general considerations, we want to compare the different sensors in terms of knots-detection capability. For this reason, we performed a simultaneous analysis mounting on the industrial machine the visible photodiode (green), the position sensitive detector (IR) and the microphones (micro) in the arrangement shown in Fig.5.32.

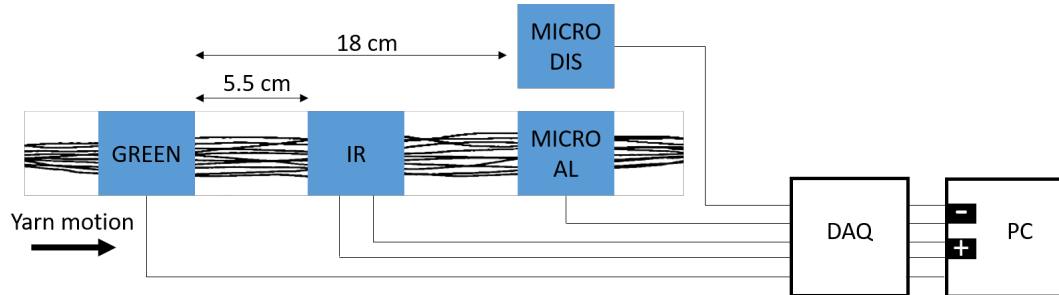


Figure 5.32: Relative positions of the sensors for the simultaneous measurement performed on the industrial machine. Green is the visible photodiode with the green LED; IR is the position sensitive detector with the IR LED; micro-all and micro-dis are the microphones, aligned and not aligned with the running yarn. For the analysis, we considered the sum of the two IR channels and the difference of the microphones time signals.

The measurements were performed using a parallel and an interlaced yarn and repeated for different yarn speed values (400, 600, 800, 1000 m/min). As indicated in Fig.5.32, we analyzed the sum of the two output signals of the position sensitive detector and the difference between the aligned and not-aligned microphone.

The FFT spectra for three increasing yarn speed values shown in Fig.5.33 indicate, as expected, the same central value of interlacing frequency for the

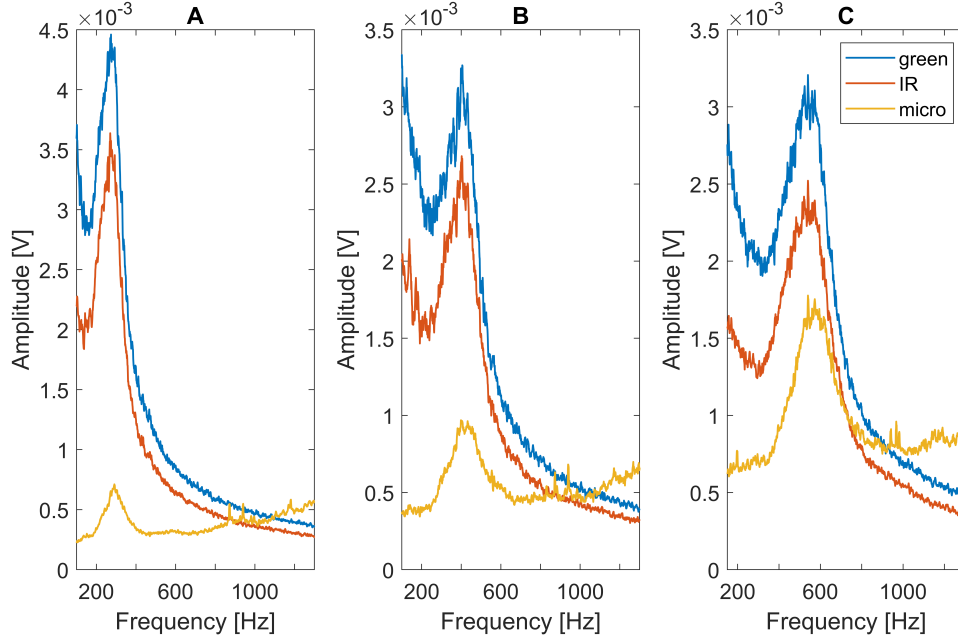


Figure 5.33: Frequency spectra obtained from the simultaneous measurements: green (visible photodiode), IR (sum of the two output channels of the position sensitive detector), micro (difference between aligned and not-aligned microphone), for different yarn speed values: 400 m/min (A), 600 m/min (B), 800 m/min (C).

three sensors. This is the first proof of agreement in the response of the three different sensors for the same analyzed yarn.

### 5.5.2 Signal to noise ratio evaluation and comparison

Besides this result, we aim to compare the sensors, in terms of capability of detecting a yarn profile modulation, with respect to a parallel yarn configuration. In Fig.5.34 is reported a comparison of the frequency response of the three sensors for a parallel and an interlaced yarn.

We calculated the integrals of the power spectral density in the bandwidth of interest (e.g. from 400-800 Hz for a 800 m/min yarn speed), both for the parallel and interlaced yarn. For each frequency value, the PSD indicates the power of that component, since the spectral resolution is 1 Hz. In this way, the SNR of our measurement is given by the power of the interlaced signal in the bandwidth of interest, divided by the power of the parallel signal in the same bandwidth, as described in Sec.4.3.4. We calculated the SNR for each sensor and yarn speed, as well as the SNR average and standard deviation over different yarn speed values.

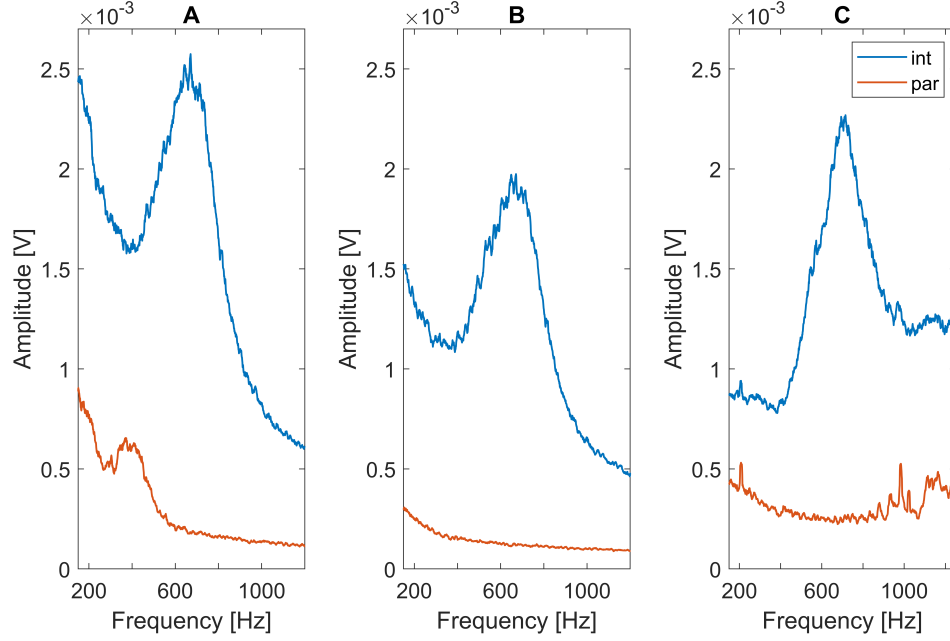


Figure 5.34: Comparison of the frequency spectra for a running interlaced (blue) and parallel (red) yarn (1000 m/min) for the green sensor (A), the IR position sensitive detector (B) and the microphone (C).

The SNR values, reported in Table 5.1, indicate that all sensors are effective in distinguishing the contribution given by an interlaced yarn with respect to a parallel yarn, without any knot. The low performance of the visible photodiode is caused by the high baseline signal given by the parallel yarn, that shows a component around 300 Hz probably caused by a yarn oscillation normal to the plane of the sensor (Fig.5.34, A). On the other hand, the IR detector measures a lower baseline signal (Fig.5.34, B), since it is less sensitive to yarn oscillations and external noise. As far as the microphone is concerned, the signal resulting from the parallel yarn increases with the yarn speed, because of a higher

Yarn speed (m/min)	Green SNR	IR SNR	Micro SNR
400	32	212	59
600	22	171	46
800	34	183	47
1000	45	135	32
<b>Average SNR</b>	$35 \pm 10$	$175 \pm 30$	$45 \pm 10$

Table 5.1: SNR averaged over 4 yarn speed values, for the different sensors.

instability in the yarn motion, that causes a higher pressure modulation. For this reason, we observe the slight decrease of the microphone SNR with the yarn speed.

Considering the average SNR values, the microphone and the visible photodiode show a similar performance, 4 times lower than the SNR of the position sensitive detector.

This estimation of the SNR accounts for the capability of detecting knots over a parallel yarn, but it is still a mean information. It does not consider that the time signal of the microphones is more difficult to relate to an irregular yarn profile or missing knots, due to higher frequency components. On the other hand, the photodiode is sensitive only to the yarn modulation, allowing for a more immediate estimation of the true knots distance and irregularity. To further investigate that point, the time signals of the sensors are compared and analyzed.

### 5.5.3 Detection of missing or irregular knots

Up to now, we have just analyzed the response of the sensors in terms of their capability of detecting the mean interlacing frequency. But we are also interested in the regularity of interlacing. In other words, we are asking ourselves if the sensors can detect irregular distances between knots and in that case, if the sensors agree in that detection. We have seen that the photodiode signal oscillates due to the knots periodicity and we managed in relating a peak in the time signal to a specific knot (Fig.5.18). However, the time signal of the microphone contains also contributions other than the pressure modulation given by the knots. This behavior is clear from the frequency spectra of Fig.5.35 (A, B). The high frequency components characterizing the microphone spectrum, prevent a direct relation between the time signal and the yarn structure. So, a direct comparison of the time signals of the different sensors does not exhibit an evident correspondence, as shown in Fig.5.35 (C, D). Filtering data with a bandpass digital filter, we can compare just the components in the frequency range interested by the interlacing process. The signals, filtered with the bandpass function implemented in Matlab, from 150 Hz to 1000 Hz, are shown in Fig.5.35 (E, F). Also in this case, it is difficult to perform a direct comparison of the time signals, since the physical processes causing the modulations are also different in the acoustic and optical cases.

As an attempt to overcome this limitation, we extracted from the time signal the contributions in the interlacing frequency range, with the correlation method described previously. For each speed, we considered a different Gaussian wave packet, with the same frequency distribution given by the interlaced yarn.

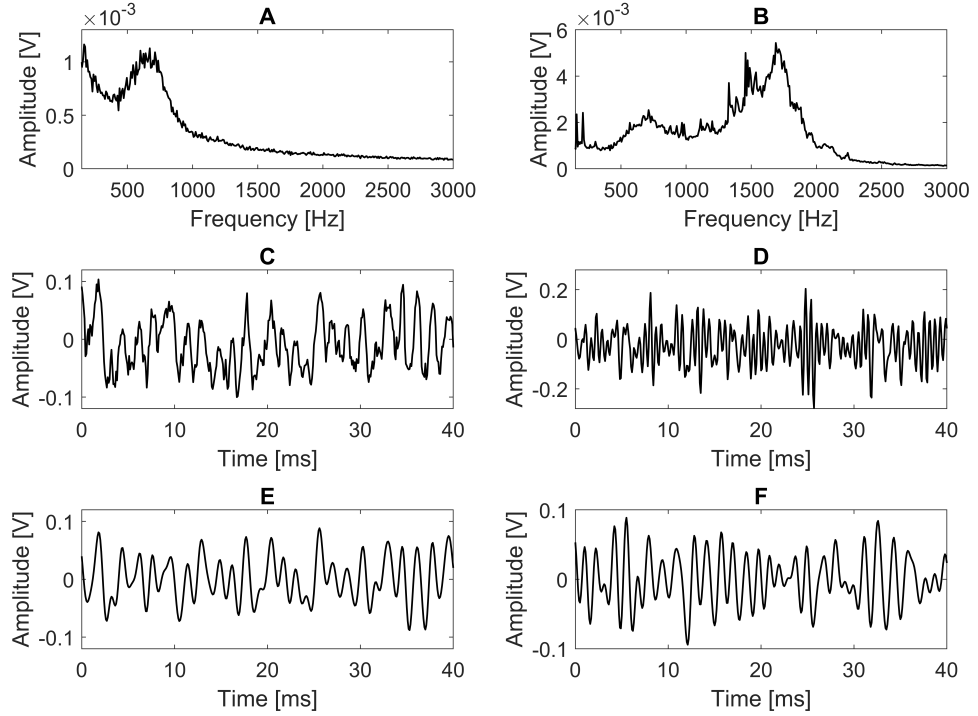


Figure 5.35: Frequency spectra and time signals acquired with the green photodiode (A, C), and the microphone (B, D). For a direct comparison, the time signal of the microphone is shifted of 10 ms due to the relative positions of the sensors. The yarn speed is 1000 m/min. Signals (C) and (D) filtered with a bandpass filter, from 150-1000 Hz (E, F).

We correlated the Gaussian wave packet with the band-passed time signals of the different sensors (from 150 Hz to 1000 Hz) and then we shifted the results, to compensate for the delay given by the relative sensors displacement. For a better comparison of the results, we consider the envelope of the positive amplitude of the correlation, reported as a black line in Fig.5.36.

The envelopes of the cross correlation for the different sensors, together with the positive cross correlation amplitude are shown in Fig.5.37. A common trend in the three sensors is clearly observable. On the other hand, the signal resulting from the parallel yarn, besides being less correlated, shows also a different pattern.

This visual partial agreement in the responses of the three sensors needs to be verified. We cross correlated the envelopes for the three sensors in order to quantify the similarity in the different cases. In Fig.5.38 is shown the cross

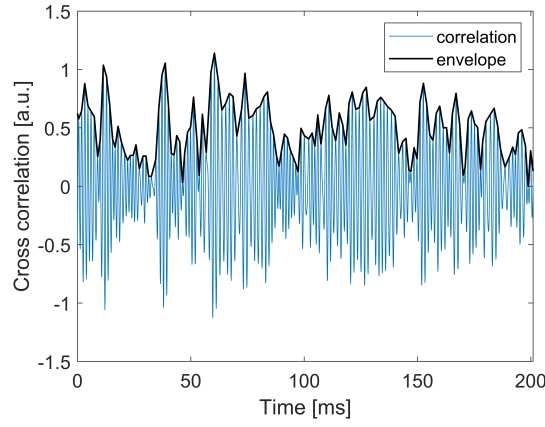


Figure 5.36: Cross correlation of the time signal recorded with the visible photodiode with a Gaussian wave packet centered around 680 Hz. In black is reported the envelope of the positive cross correlation amplitude. The interlaced yarn speed was 1000 m/min.

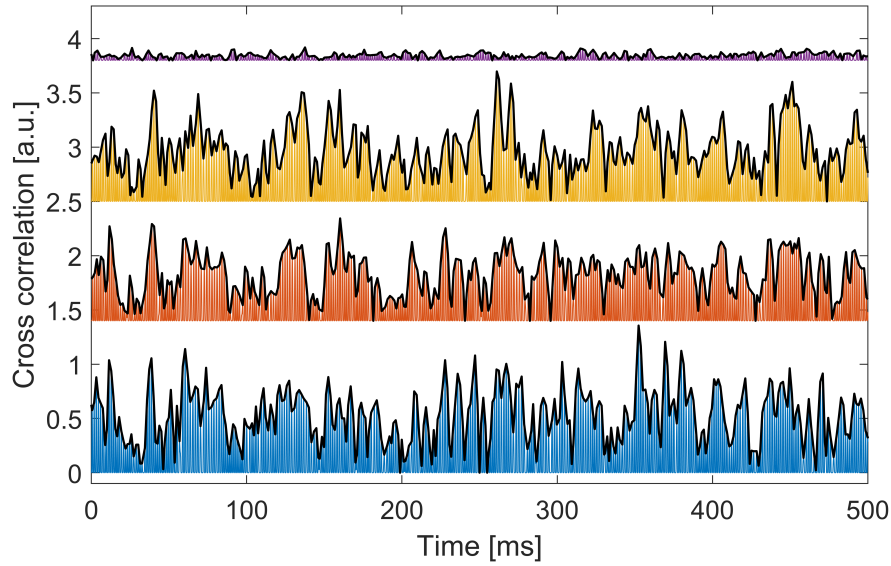


Figure 5.37: Positive values of the cross correlation between a Gaussian wave packet and the time signal for an interlaced yarn acquired with the visible photodiode (blue), IR position sensitive detector (red), microphone (yellow) and for a parallel yarn with the visible photodiode (violet). The IR signal is shifted of 3 ms, the microphone of 11 ms to compensate for the delay given by the relative sensors displacement. The signals are shifted along the y-axis for a better comparison of the envelopes of the cross correlation (black contour).

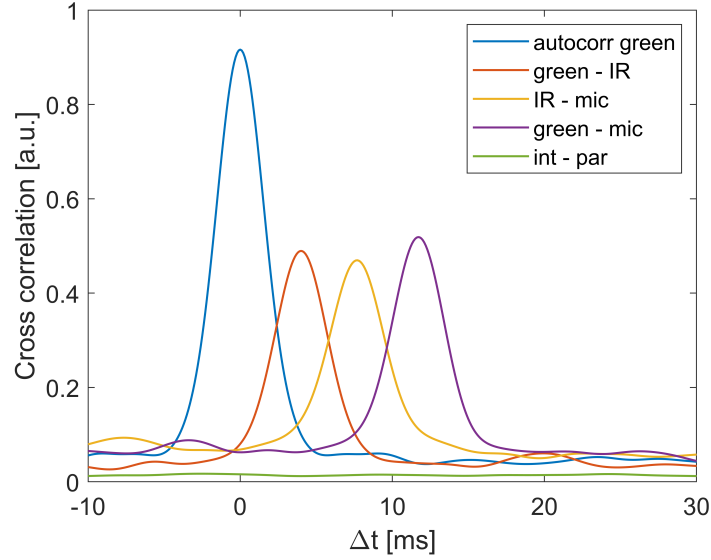


Figure 5.38: Cross-correlation between the envelopes shown in Fig.5.37 of the 3 sensors for an interlaced yarn (red, yellow, violet). In blue is reported, as reference, the autocorrelation value. In green is shown the cross correlation between the envelopes of an interlaced and a parallel yarn.

correlation between the envelopes of the sensors and also the correlation between an interlaced and parallel yarn signal. As a reference of the maximum peak value, we calculated the autocorrelation of each signal.

We observe that the envelopes of the sensors are well correlated (about one-half of the maximum correlation value), while the envelopes of the parallel and interlaced yarn are not correlated at all. The delay detected in the cross correlations is exactly caused by the relative displacement of the sensors. This is a further confirmation of the correctness of the analysis.

This result proved that the three sensors are actually detecting the same irregularity in the signal. In other words, a punctual analysis of the yarn profile can be performed even with the microphone. This observation is just preliminary and needs further investigations to find the best way to extract the information in terms of regularity in the knots distance for the three sensors.

### Chapter conclusions

Here, we studied a photodiode-based sensing technique. The sensor has been calibrated to quantify and monitor the yarn diameter over time. We demonstrated that for a good diameter estimation (uncertainty of about  $20\text{ }\mu\text{m}$ ), a transimpedance amplifier configuration is necessary. The photodiode is sensitive to the yarn profile modulations in the interlacing industrial working

conditions and we found that the main noise source in such a measurement is the random yarn diameter variation due to its oscillation and rotation. First, we performed a frequency analysis and we found a component at the expected value for interlacing. Then, we analyzed the time signal to extract an information also about the process regularity in terms of missing or weak knots. Once found a matching between the signal in time and the knots-pattern on the corresponding interlaced yarn, we compared different techniques to evaluate the yarn regularity. The best analysis proposed is based on the cross correlation between the time signal and a Gaussian wave packet, to highlight the irregular patterns. This method permits a real time signal analysis, ensuring a punctual and quantitative information on the process stability.

Finally, we compared the acoustic and optical sensors and we found a good agreement in the predicted interlacing frequency values. We analyzed also the time signals with the proposed cross-correlation analysis and then the envelopes of the cross correlation have been correlated again. In this way, we demonstrated that both the microphone and the photodiode are sensing the same defects in the yarn. So, we proved that also the microphone is suitable for a punctual real-time yarn analysis.



## Conclusions and future perspectives

This work dealt with the investigation of a process commonly employed in textile industries, called **interlacing**. By means of a jet of compressed air, the fibers constituting a multi-filament yarn are intermingled with each other, creating the cohesion points necessary for the yarn post manufacturing, such as weaving or knitting. In the first chapter, we reported different studies about interlacing, found in literature. Actually, the process is still not fully characterized and understood, especially for the geometry of the interlacers commonly employed in industries.

One issue that textile companies are facing, is related to the regularity of the process. Indeed, missing, weak or not regular knots occur without a clear reason, creating not-homogeneous patterns in the final fabric. For this reason, the distance between knots needs to be monitored, on-line during yarn production, with a sensor cheap enough to be implemented on hundreds of interlacers used in an industrial plant. This issue laid the foundations of the PhD research work.

The problem was faced from a wider perspective than the simple investigation of an on-line sensor, starting with the study the dynamics of knots formation. By means of a **high speed imaging** technique we observed that the air flow, moving in twin vortexes, plays a key role in the fibers intermingling. The filaments are opened and spread by the air jet, enter the vortexes and two entangling regions are created on both sides, before and after the air nozzle. By means of a tracer, we observed the air motion, having a first hint of the flow instability. It would be interesting to further improve this measurement in order to better characterize the air motion. In particular, we aim to track particles moving in the air flow to quantify its vorticity and stability.

We suggested that the interaction of the yarn with the air flow causes a modulation of vortexes and shock waves, responsible in turn of the periodicity of interlacing. To verify this hypothesis we monitored the **vibrations** in front of the interlacer, optimizing an accelerometer-based experimental procedure. However, no vibration in the interlacing frequency range was detected, indi-

cating that, if the yarn causes a flow modulation, it does not occur at a defined frequency.

Moving towards the development of an on-line monitoring sensor, we examined an **acoustic technique**, based on the idea that a running interlaced yarn, due to its periodic profile, causes periodic pressure modulations in its surroundings. The microphone sensitivity in the frequency region of interest has been optimized by means of an acoustic filter. Additionally, we compared different multi-microphones techniques to enhance the signal and we found that in our case a differential measurement using an aligned and not-aligned microphone is the most effective. In this way, we could reach the required sensitivity to detect the yarn modulation and we estimated the correct mean distance between knots. We performed the measurement during the yarn production, on the industrial machine, before yarn collection into reels. This technique is cheap and non invasive, but it is affected by external noise disturbances.

For this reason, we investigated also an **optical sensing** technique, based on the use of a photodiode that monitors the shadow of the yarn over time. We studied the effects of yarn oscillations and rotations on the measurement, using also a position sensitive detector. A step forward for complete characterization of the yarn motion could be realized with two perpendicular position sensitive detectors. We managed in estimating the yarn diameter and its fluctuations with a proper sensor calibration and we evaluated the mean distance between knots.

Then, we moved from a mean to a punctual time analysis of the yarn profile. Different techniques that highlight irregular patterns in the profile, due to missing or weak knots, were compared. The best method proposed and analyzed deals with the correlation of the time signal acquired with the photodiode with an optimal, regular Gaussian probe. We investigated different approaches to fix a threshold on the correlation, in such a way that amplitudes below that value indicate the occurrence of an irregularity in the yarn profile. In the end, we performed simultaneous measurements with the different sensors (i.e. microphone, photodiode and position sensitive detector). We verified that all sensors detect the same value of interlacing frequency. The position sensitive detector resulted more effective in recognizing an interlaced with respect to a parallel yarn. Additionally, we demonstrated that the three sensors detect the same irregularities on an interlaced yarn.

The analysis proposed here can be easily implemented for the on-line diagnosis of the process regularity. Indeed, once fixed the optimal Gaussian probe,

we can perform the analysis directly on the signal in time, since it is low time consuming. If we analyze for example a 10 s signal, the computational time required to evaluate the mean knots distance, fix the threshold and characterize its irregularities is about 1 s. The response is fast enough to propose a further step: when the sensor detects an irregular production, the key parameters affecting interlacing, like the yarn speed or tension, can be changed accordingly, to restore the process regularity on-line. In this way, we could reduce time and product waste.

Additionally, one could think to simulate the yarn motion to calibrate the optical system properly. This means that we could create an artificial video with different simulated acquisition settings, to reproduce the yarn motion in several conditions. We could for example consider to vary the yarn speed, the image noise or the spatial resolution, in a way that the real system is emulated, in various working configurations. This ideal reproduction could be useful for example to verify the feasibility of a measurement with a particular sensor, avoiding an ad hoc experiment with the high speed camera. Additionally it could be used as calibration to evaluate the difference between a real measurement and an ideal one, to quantify the process regularity.



## Bibliography

- [1] <https://www.aquafil.com>.
- [2] L. W. McKeen. *Film properties of plastics and elastomers*. William Andrew, 2017.
- [3] C. Giori and B.T. Hayes. Hydrolytic polymerization of caprolactam. i. hydrolysis—polycondensation kinetics. *Journal of Polymer Science Part A-1: Polymer Chemistry*, 8(2):335–349, 1970.
- [4] B. L. Deopura, R. Alagirusamy, M. Joshi, and B. Gupta. *Polyesters and polyamides*. Elsevier, 2008.
- [5] H. K. Reimschuessel. Nylon 6. chemistry and mechanisms. *Journal of Polymer Science: Macromolecular Reviews*, 12(1):65–139, 1977.
- [6] J. E. McIntyre. *Synthetic fibres: nylon, polyester, acrylic, polyolefin*. Taylor & Francis US, 2005.
- [7] R. J. Crawford. *Plastics engineering*. Elsevier, 1998.
- [8] D.V. Rosato. Extruding plastics-a practical processing handbook. 1998.
- [9] R. A. Charvat. *Coloring of plastics: Fundamentals*, volume 35. John Wiley & Sons, 2005.
- [10] M. Lewin. *Handbook of fiber chemistry*. Crc press, 2006.
- [11] R. Sinclair. *Textiles and fashion: materials, design and technology*. Elsevier, 2014.
- [12] F. W. Billmeyer. Textbook of polymer science. 1971.
- [13] A. R. Bunsell. *Handbook of properties of textile and technical fibres*. Woodhead Publishing, 2018.
- [14] D. R. Holmes, C. W. Bunn, and D. J. Smith. The crystal structure of polycaproamide: Nylon 6. *Journal of Polymer Science*, 17(84):159–177, 1955.

- [15] A. Galeski, A. S. Argon, and R. E. Cohen. Morphology of nylon 6 spherulites in bulk. *Die Makromolekulare Chemie: Macromolecular Chemistry and Physics*, 188(5):1195–1204, 1987.
- [16] V. K. Kothari and N. B. Timble. Air-jet texturing: Effect of jet type and some process parameters on properties of air-jet textured yarns. 1991.
- [17] A. Sparavigna, E. Broglia, and S. Lugli. Beyond capacitive systems with optical measurements for yarn evenness evaluation. *Mechatronics*, 14(10):1183–1196, 2004.
- [18] W. G. Van Holten. Continuous filament interlacing, bulking or tangling apparatus, July 30 1968. US Patent 3,394,440.
- [19] Jr W. W. Bunting and N. T. Larson. Compact interlaced yarn, May 30 1961. US Patent 2,985,995.
- [20] M. Acar, W. L. Dudeney, J. Jones, M. R. Jackson, and W. Malalasekera. Laser fusion to impart cohesion to textured filament yarns. *Journal of industrial textiles*, 34(3):181–193, 2005.
- [21] M. Juraeva, D. Joo Song, and K. Jin Ryu. An optimum design study of the yarn-channel shape of the air-interlacing nozzle by analysis of fluid flow. *Textile Research Journal*, 82:474–483, 03 2012.
- [22] S. W. Chau and W. L. Liao. Determination of yarn interlacing frequency of triangular interlacing nozzles through a compressible flow simulation. *Textile Research Journal*, 78(8):699–709, 2008.
- [23] Y. Iemoto, S. Tanoue, and H. Qiu. Numerical simulation of effects of size of circular yarn duct of interlacer on airflow patterns. *Journal of Textile Engineering*, 56(3):87–96, 2010.
- [24] C. Simmen. Method and entanglement nozzle for reproducing knotted yarn, February 5 2009. US Patent App. 11/886,767.
- [25] H. Qiu, Y. Iemoto, and S. Tanoue. Yarn motion in interlacers with various cross-sectional shapes of yarn duct. *Journal of Textile Engineering*, 53(2):59–67, 2007.
- [26] Y. Iemoto, S. Chono, and T. Tanaka. Study on interlaced yarn, part 4. *Journal of the Textile Machinery Society of Japan*, 41(2):57–63, 1988.
- [27] Y. Iemoto, S. Chono, and T. Tanaka. Study on interlaced yarn, part 6. *Journal of the Textile Machinery Society of Japan*, 43(2):44–50, 1990.

- [28] Y. Iemoto, K. Yokota, H. Uematsu, and S. Tanoue. Analysis of interlacing process by high-speed video image of filament motion. *Journal of Textile Engineering*, 62(4), 2016.
- [29] P. Duru Baykal and İ. Özkan. The effects of intermingling process parameters and number of filaments on intermingled yarn properties. *The Journal of The Textile Institute*, 104(12):1292–1302, 2013.
- [30] M. Acar, R. K. Turton, and G. R. Wray. 18—an analysis of the air-jet yarn-texturing process part iv: Fluid forces acting on the filaments and the effects of filament cross-sectional area and shape. *The Journal of The Textile Institute*, 77(4):247–254, 1986.
- [31] R. Alagirusamy, V. Ogale, A. Vaidya, and P.M.V. Subbarao. Effect of jet design on commingling of glass/nylon filaments. *Journal of Thermoplastic Composite Materials*, 18(3):255–268, 2005.
- [32] J. W. S. Hearle, L. Hollick, and D. K. Wilson. *Yarn texturing technology*. Elsevier, 2001.
- [33] Y. Iemoto, S. Tanoue, J. Lu, and T. Takano. Effects of size of interlacer on air flow in a yarn duct. *Journal of Textile Engineering*, 55(4):111–118, 2009.
- [34] M. Miao and C. S. Mei-Chun. Air interlaced yarn structure and properties. *Textile Research Journal*, 65(8):433–440, 1995.
- [35] H. Qiu, Y. Iemoto, and S. Tanoue. Effects of cross-sectional shape of yarn duct of interlacer on the properties of interlaced yarn. *Journal of Textile Engineering*, 53(1):1–8, 2007.
- [36] H. Qiu, Y. Iemoto, and S. Tanoue. Evaluation of significance of processing parameters to characteristics of interlaced yarn. *Journal of Textile Engineering*, 55(3):99–102, 2009.
- [37] S. Chono, Y. Iemoto, and W. Han. Model experiment on interlaced yarn part 4 : Characteristics of a new interlacing process without conventional interlacers. *Journal of the Textile Machinery Society of Japan*, 45:19–24, 1999.
- [38] H. Qiu and Y. Jin. Three dimensional flow simulation in yarn duct of interlacers with various cross-sectional shapes. *Journal of engineered fibers and fabrics*, 7:43–49, 09 2012.

- [39] Y. Iemoto, S. Chono, and M. Ge. On-line evaluation of interlaced yarn. *Journal of the Textile Machinery Society of Japan*, 45(3):79–88, 1999.
- [40] M. P. Millman, M. Acar, and M. R. Jackson. Computer vision for textured yarn interlace (nip) measurements at high speeds. *Mechatronics*, 11(8):1025–1038, 2001.
- [41] N. Otsu. A threshold selection method from gray-level histograms. *IEEE Transactions on Systems, Man, and Cybernetics*, 9(1):62–66, Jan 1979.
- [42] Pierre Wickramarachi. Effects of windowing on the spectral content of a signal. *Sound and vibration*, 37(1):10–13, 2003.
- [43] S. Ristic. Flow visualisation techniques in wind tunnels part i–non optical methods. *Scientific Technical Review*, 57(1):39–50, 2007.
- [44] R. Acharya. *Satellite Signal Propagation, Impairments and Mitigation*. Academic Press, 2017.
- [45] T. P. Wright, C. Song, s. Sears, and M. D. Petters. Thermodynamic and kinetic behavior of glycerol aerosol. *Aerosol Science and Technology*, 50(12):1385–1396, 2016.
- [46] J. P. Bonnet and E. Chaput. Large-scale structures visualization in a high reynolds number, turbulent flat-plate wake at supersonic speed. *Experiments in fluids*, 4(6):350–356, 1986.
- [47] K. Avila, D. Moxey, A. de Lozar, M. Avila, and B. Barkley, D.and Hof. The onset of turbulence in pipe flow. *Science*, 333(6039):192–196, 2011.
- [48] A. Zhou, K. Wang, L. Wang, F. Du, and Z. Li. Numerical simulation for propagation characteristics of shock wave and gas flow induced by outburst intensity. *International Journal of Mining Science and Technology*, 25(1):107 – 112, 2015.
- [49] A. Markhotok. A shock wave instability induced on a periodically disturbed interface with plasma. *IEEE Transactions on Plasma Science*, pages 1–10, 2018.
- [50] H. Hosseini, S. Moosavi-Nejad, H. Akiyama, and V. Menezes. Shock wave interaction with interfaces between materials having different acoustic impedances. *Applied Physics Letters*, 104, 03 2014.
- [51] O. Ram and O. Sadot. Analysis of the pressure buildup behind rigid porous media impinged by shock waves in time and frequency domains. *Journal of Fluid Mechanics*, 779:842–858, 2015.



- [52] B. W. Skews, M. D. Atkins, and M. W. Seitz. The impact of a shock wave on porous compressible foams. *Journal of Fluid Mechanics*, 253, 8 1993.
- [53] A. Garcia-Perez, J. Amezquita-Sanchez, D. Morínigo Sotelo, and K. Gyftakis. Vibration analysis as a diagnosis tool for health monitoring of industrial machines. 2016:1–2, 07 2016.
- [54] M. M. Campagna, G. Dinardo, L. Fabbiano, and G. Vacca. Fluid flow measurements by means of vibration monitoring. *Measurement Science and Technology*, 26(11):115306, 2015.
- [55] J. Tuma. Gearbox noise and vibration prediction and control. *International Journal of Acoustics and Vibration*, 14(2):1–11, 2009.
- [56] P. Šuránek, M. Mahdal, J. Tuma, and J. Zavadil. Modal analysis of the cantilever beam. *Proceedings of the 14th International Carpathian Control Conference (ICCC)*, pages 367–372, 2013.
- [57] C. Sujatha. *Vibration and Acoustics*. Tata McGraw-Hill Education, 2010.
- [58] E. Alberti, G. Moschioni, B. Saggin, and M. Tarabini. Mechanical filters for accelerometers: Design and metrological characterization. *Proceedings of the IEEE Instrumentation and Measurement Technology - Sorrento, Italy*, pages 2254–2259, 2006.
- [59] J. Knapp, E. Altmann, J. Niemann, and K. D. Werner. Measurement of shock events by means of strain gauges and accelerometers. *Measurement*, 24(2):87 – 96, 1998.
- [60] S. G. Kelly. *Mechanical vibrations: theory and applications*. Cengage learning, 2012.
- [61] Alok Sinha. *Vibration of mechanical systems*. Cambridge University Press, 2010.
- [62] D. S. Dugdale. Discrete frequency noise from free running circular saws. *Journal of sound and vibration*, 10(2):296–304, 1969.
- [63] G. Boré and S. Peus. Microphones. methods of operation and type examples. *Edition, Georg Neumann, Berlin*, 1999.
- [64] Y. Lee, P. Kim, Y. J. Jung, Y. M. Chang, J. H. Cho, and M. N. Kim. Custom-made ite type hearing protection device using a small acoustic filter. *Journal of Biomedical Engineering Research*, 27(6):376–383, 2006.

- [65] L. E. Kinsler, A. R. Frey, A. B. Coppens, and J. V. Sanders. Fundamentals of acoustics. *Fundamentals of Acoustics, 4th Edition, by Lawrence E. Kinsler, Austin R. Frey, Alan B. Coppens, James V. Sanders, pp. 560. ISBN 0-471-84789-5. Wiley-VCH, December 1999.*, page 560, 1999.
- [66] R. P. Feynman, R. B. Leighton, and M. Sands. *The Feynman lectures on physics, Vol. I: The new millennium edition: mainly mechanics, radiation, and heat*, volume 1. Basic books, 2011.
- [67] T. Cox and P. d'Antonio. *Acoustic absorbers and diffusers: theory, design and application*. Crc Press, 2016.
- [68] J. Zhang, R. J. Perez, and E. J. Lavernia. Documentation of damping capacity of metallic, ceramic and metal-matrix composite materials. *Journal of Materials Science*, 28(9):2395–2404, 1993.
- [69] B. C. Moore. *Hearing*. Academic Press, 1995.
- [70] T. M. Sullivan. Multi-microphone correlation-based processing for robust automatic speech recognition. *Unpublished doctoral dissertation, Carnegie Mellon University, Pittsburgh, USA*, 1996.
- [71] B. E. A. Saleh and M. C. Teich. *Fundamentals of photonics*. John Wiley & sons, 2019.
- [72] J. G. Graeme and J. G. Graeme. *Photodiode amplifiers: op amp solutions*. McGraw-Hill New York, 1996.
- [73] H. Spieler. Introduction to radiation detectors and electronics. *Lecture Notes-Physics*, 198, 1998.

## Publications

M. Bertolla, C. Castellan, D. Roilo Eds., "Proceedings of the event IPSP2016 - Industrial Problem Solving with Physics", University of Trento Press, 2016, ISBN (978-88-8443-713-6).

M. Bertolla, L.Cenci, A. Anesi et al., "Solvent-responsive Molecularly Imprinted Nanogels for targeted protein analysis in MALDI-TOF mass spectrometry". ACS Applied Materials and Interfaces, vol. 9, pp 6908–6915, 2017.

L. Cenci, M. Bertolla, A. Anesi et al., "Micro- versus nano-sized molecularly imprinted polymers in MALDI-TOF mass spectrometry analysis of peptides", Analytical and Bioanalytical Chemistry, vol. 409, pp. 6253-6261, 2017.

M. Bertolla, M. Scotoni, M. Caldara et al., "On-line sensing of the interlacing process". 2017 IEEE Sensors, vol. 9, pp. 1679–1681, 2017.

M. Bertolla, M. Scotoni, "Optical sensing online: an interlacing yarn". Organic Photonic Materials and Devices XXI, vol. 10915, Conference Presentation, 2019.



## Conference presentations

Congresso Nazionale della Società Italiana di Fisica (SIF), 11-15 September 2017, Trento, Italy. Oral presentation on "Looking and sensing an interlaced yarn".

IEEE Sensors 2017, 29 October-1 November 2017. Glasgow, Scotland. Oral presentation on "On-Line Sensing of the Interlacing Process".

6th International Symposium on Optics and its Applications (OPTICS-2018), 17-20 February 2018. Trento, Italy. Oral presentation on "Industry meets academic research: the challenge of sensing an interlacing yarn".

Euronoise 2018, 27-31 May 2018. Heraklion, Crete. Oral presentation on "Acoustic sensing of an interlaced yarn in a noisy industrial environment".

SPIE Photonics West, 2-7 February 2019. San Francisco, California, USA. Oral presentation on "Optical sensing online: an interlacing yarn".



## Acknowledgments

When you climb a mountain and you reach the summit, the scenario around you is not the only source of satisfaction. The sensation of serenity and fullness is the result of the effort in each step of your hiking, with the right companions that with an encouraging gaze, reassuring smile and a strong hand make efforts lighter and the right path brighter.

First, I would like to acknowledge the company, Aquafil, for showing me that mountain and giving me the opportunity to explore it. I wish to thank Mauro Caldara and Giuseppe Crippa, for their continuous support and suggestions. I'd like to recognize the assistance of Gianmarco Giacomelli and Franco Grossi, that helped me in performing the measurements on the industrial plant, with patience and enthusiasm. I am grateful to Emanuele Pasqualini that provided me with helpful advices about the differences between research in a company and in university. Many thanks also to Michele Preghenella and Michele Cecchetto, that introduced me to the whole process of yarn Nylon 6 polymerization and industrial yarn production.

A decisive role in this work was played by my supervisor, prof. Mario Scotoni. In the most difficult crossroads, he calmly suggested me always brilliant and unpredictable solutions, helping me both with new ideas and experiments.

I would like to thank also the mechanics and electronic services of the Department of Physics, with special thanks to Sandro, for his electronic and personal advices. Thank you also to prof. Graziano Guella, my "scientific father", for his tips and suggestions.

The right companions in this hike were the colleagues and friends that supported each day and step. Stefano, the second, unofficial supervisor of this PhD. He disclosed to me the secrets of the compute button in Comsol, supported and advised me when the project was still unclear and difficult to tackle. Each day of this PhD he helped me in understanding the yarn entangling and the disentangling of my mind. Claudio, the stable, longtime study-companion. During those 8 years we faced together many different (dis)adventures, but even replacing a punctured tire he was calm and organized! One of the best

adventures in this PhD has been the organization of IPSP, with a perfect trio: me, Claudio and David. David is a colleague that in short time became a good friend, since too special to let him run away: mango and tissues are our secrets. Kick is the name of a sheep, Chiara knows why. A careful and loving friend, we shared satisfactions and problems in the canteen, mountains and good advises under the sun.

Special thanks to the friends that offered me a smile and a second house in the last 3 years, Andrea, Emanuele, Samuele, Nicolò and Nadir.

Thank you Gloria for your engaging enthusiasm and honest suggestions; pan con palta has been a memorable experience. Thank you Federica, for your sparkling happiness. Thank you Andrea, the most trustable and sincere friend. Thank you Stefy, a walkie-talkie friend from the childhood.

Thank you Matteo, with a laugh, a smile and fresh air in the mountains, the last part of this hike was lighter.

I would like to thank people I met with "La Rete", for teaching me the beauty and simplicity of human relations.

I am extremely grateful to my family. I thank my parents, my brothers Luca and Giuseppe that are my home and my rock, with Francesca and Elena. Samuel and Andrea showed me the simplicity of life through children eyes. Thank you Riccardo, the third brother of my family.

Finally, I thank the mountains, always source of happiness, freshness and surprise, they gave me the strength and suggestions to face each decision with the awareness I was looking for.

*Maddalena*